Development of Ultrafast Laser Inscribed Astrophotonic Components

Fraser Andrew Pike

Submitted for the degree of Doctor of Philosophy

Heriot-Watt University

School of Engineering and Physical Sciences

February 2022

ABSTRACT

The rapid development of astronomical instrumentation has been aided by many innovative new photonic designs, which offer improvements in stability, precision, size and cost, scalability, etc. ─ the field of astrophotonics. A powerful technique enabling many of these astrophotonic devices, ultrafast laser inscription (ULI), creates highly localised and controlled refractive index modification, which guides the path of light in a very efficient manner. This thesis discusses three separate astrophotonic devices, each with a specific application, to demonstrate the versatility of ULI.

Firstly, a reformatting device based on a photonic lantern and 3D ULI waveguide reformatting component, transforms a multimode telescope PSF to a diffraction-limited pseudo-slit. When used to feed a spectrograph, a significant reduction in modal noise ─ a limiting factor in high-resolution multimode fibre-fed spectrographs ─ is demonstrated, with the potential for improved near-infrared radial velocity observations. Secondly, a similar ULI reformatting device for an integral field unit, based on multicore fibre with affixed microlenses, may enable the direct imaging of exoplanets and characterisation of their atmospheres. Thirdly, a two-telescope K-band beam combiner based on ULI directional couplers with an achromatic 3dB splitting ratio is presented. Such a device will upgrade the stellar interferometry capabilities of the CHARA array.

ACKNOWLEDGEMENTS

Research Thesis Submission

Name*:*	Fraser Pike		
School:	EPS		
Version: *(i.e. First, Resubmission, Final)*	Final	Degree Sought:	PhD

Declaration

In accordance with the appropriate regulations I hereby submit my thesis and I declare that:

1. The thesis embodies the results of my own work and has been composed by myself
2. Where appropriate, I have made acknowledgement of the work of others
3. The thesis is the correct version for submission and is the same version as any electronic versions submitted*.
4. My thesis for the award referred to, deposited in the Heriot-Watt University Library, should be made available for loan or photocopying and be available via the Institutional Repository, subject to such conditions as the Librarian may require
5. I understand that as a student of the University I am required to abide by the Regulations of the University and to conform to its discipline.
6. I confirm that the thesis has been verified against plagiarism via an approved plagiarism detection application e.g. Turnitin.

ONLY for submissions including published works

7. Where the thesis contains published outputs under Regulation 6 (9.1.2) or Regulation 43 (9) these are accompanied by a critical review which accurately describes my contribution to the research and, for multi-author outputs, a signed declaration indicating the contribution of each author (complete)
8. Inclusion of published outputs under Regulation 6 (9.1.2) or Regulation 43 (9) shall not constitute plagiarism.

*   *Please note that it is the responsibility of the candidate to ensure that the correct version of the thesis is submitted.*

Signature of Candidate*:*	*Fraser Pike*	Date:	18/02/2022

Submission

Submitted By *(name in capitals):*	FRASER PIKE
Signature of Individual Submitting:	*Fraser Pike*
Date Submitted:	18/02/2022

For Completion in the Student Service Centre (SSC)

Limited Access	Requested	Yes		No		Approved	Yes		No	
*E-thesis Submitted (**mandatory for final theses**)*										
Received in the SSC by *(name in capitals):*						Date:				
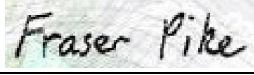
Inclusion of Published Works
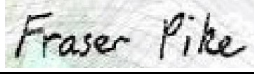
Citation details	F. A. Pike, A. Benoît, D. G. MacLachlan, R. J. Harris, I. Gris-Sánchez, D. Lee, T. A. Birks, R. R. Thomson, Modal noise mitigation for high-precision spectroscopy using a photonic reformatter, Monthly Notices of the Royal Astronomical Society, 497, 3713-3725 (2020)
F. A. Pike	I characterised the source and fibres; I constructed the and aligned it with each of the 3 devices which were tested; I collected and analysed the data to determine the precision of the spectrograph; I created the figures and wrote the paper
A. Benoît	Helped to collect and analyse data, and write the paper
D. G. MacLachlan, R. J. Harris	Made the reformatter
I. Gris-Sánchez	Made the photonic lantern
D. Lee	Assisted with spectrograph design
T. A. Birks	Helped write the paper
R. R. Thomson	Provided guidance on data collection and analysis and helped write the paper
Signature:	*Fraser Pike*
Date:	18/02/2022

Citation details	S. Y. Haffert, R. J. Harris, A. Zanutta, F. A. Pike, A. Bianco, E. M. A. Redaelli, A. Benoît, D. G. MacLachlan, C. A. Ross, I. Gris-Sánchez, M. D. Trappen, Y. Xu, M. Blaicher, P. Maier, G. Riva, B. Sinquin, C. Kulcsár, N. A. Bharmal, É. Gendron, L. Staykov, T. J. Morris, S. Barboza, N. Münch, L. F. Bardou, L. Prengère, H.-F. G. Raynaud, P. Hottinger, T. Anagnos, J. Osborn, C. Koos, R. R. Thomson, T. A. Birks, I. A. G. Snellen, C. U. Keller, Diffraction-limited integral-field spectroscopy for extreme adaptive optics systems with the multicore fiber-fed integral-field unit, Journal of Astronomical Telescopes, Instruments, and Systems, 6, 045007 (2020)
S. Y. Haffert	Organised the project, helped integrate the MCIFU and perform obserations, analysed the on-sky data, wrote the paper
R. J. Harris	Helped organise the project, designed the reformatter geometry, packaged the fibre link, helped integrate the MCIFU and perform obserations, wrote the paper
A. Zanutta, A. Bianco, E. M. A. Redaelli, G. Riva	Made the spectrograph, assisted with the integration of the MCIFU on-sky, helped to write the paper
F. A. Pike	Made and characterised the reformatter, connected the mask and multicore fibre to the reformatter, assisted with the integration of the MCIFU on-sky, helped to write the paper
A. Benoît, D. G. MacLachlan, C. A. Ross	Made the mask and support chip, helped to connect the mask and multicore fibre to the reformatter, and helped to write the paper
I. Gris-Sánchez	Made the multicore fibre
M. D. Trappen, Y. Xu, M. Blaicher, P. Maier, C. Koos	Made the microlens array on the multicore fibre

B. Sinquin, C. Kulcsár, N. A. Bharmal, É. Gendron, L. Staykov, T. J. Morris, S. Barboza, N. Münch, L. F. Bardou, L. Prengère, H.-F. G. Raynaud, P. Hottinger, T. Anagnos, J. Osborn	Prepared and used the adaptive optics system during observations
R. R. Thomson, T. A. Birks, I. A. G. Snellen, C. U. Keller	Advised on project direction and paper writing
Signature:	*Fraser Pike*
Date:	18/02/2022

Citation details	A. Benoît*, F. A. Pike*, T. K. Sharma*, D. G. MacLachlan, A. N. Dinkelaker, A. S. Nayak, K. Madhav, M. M. Roth, L. Labadie, E. Pedretti, T. A. ten Brummelaar, N. Scott, V. Coudé du Foresto, and R. R. Thomson, Ultrafast laser inscription of asymmetric integrated waveguide 3 dB couplers for astronomical K-band interferometry at the CHARA array, Journal of the Optical Society of America B, 38, 2455-2464 (2021) *denotes joint first authorship
A. Benoît	Assisted with characterisation of the beam combiner, wrote the paper
F. A. Pike	Fabricated and characterised the beam combiner and all preceding steps e.g. straight waveguides, helped to analyse data, helped write the paper
T. K. Sharma	Performed the polarization study and interferometry measurements, helped write the paper
D. G. MacLachlan	Helped with the beam combiner fabrication
A. N. Dinkelaker, A. S. Nayak, K. Madhav, M. M. Roth	Organised the interface of the beam combiner and fibre v-groove for the desired application, helped write the paper
L. Labadie, E. Pedretti, R. R. Thomson	Helped with project design and specifications, helped write the paper
T. A. ten Brummelaar, N. Scott, V. Coudé du Foresto	Advised on specifications and goals for theintended purpose of on-sky testing
Signature:	*Fraser Pike*
Date:	18/02/2022

TABLE OF CONTENTS

LIST OF PUBLICATIONS BY THE CANDIDATE

Peer-reviewed journal publications

F. A. Pike, A. Benoît, D. G. MacLachlan, R. J. Harris, I. Gris-Sánchez, D. Lee, T. A. Birks, R. R. Thomson, "Modal noise mitigation for high-precision spectroscopy using a photonic reformatter," *Monthly Notices of the Royal Astronomical Society* 497, 3713 (2020); https://doi.org/10.1093/mnras/staa1950

S. Y. Haffert, R. J. Harris, A. Zanutta, **F. A. Pike**, A. Bianco, E. Maria Alberto Redaelli, A. Benoît, D. G. MacLachlan, C. A. Ross, I. Gris-Sánchez, M. D. Trappen, Y. Xu, M. Blaicher, P. Maier, G. Riva, B. Sinquin, C. Kulcsár, N. A. Bharmal, É. Gendron, L. Staykov, T. J. Morris, S. Barboza, N. Münch, L. F. Bardou, L. Prengère, H. G. Raynaud, P. Hottinger, T. Anagnos, J. Osborn, C. Koos, R. R. Thomson, T. A. Birks, I. A. G. Snellen, C. U. Keller, "Diffraction-limited integral-field spectroscopy for extreme adaptive optics systems with the multicore fiber-fed integral-field unit," *J. Astron. Telesc. Instrum. Syst.* 6 045007 (2020); https://doi.org/10.1117/1.JATIS.6.4.045007

A. Benoît, **F.A. Pike**, T. K. Sharma, D. G. MacLachlan, A. N. Dinkelaker, A. S. Nayak, K. Madhav, M. M. Roth, L. Labadie, E. Pedretti, T. A. ten Brummelaar, N. Scott, V. Coudé du Foresto, and R. R. Thomson, "Ultrafast laser inscription of asymmetric integrated waveguide 3 dB couplers for astronomical K-band interferometry at the CHARA array," *J. Opt. Soc. Am. B* **38**, 2455-2464 (2021); https://doi.org/10.1364/JOSAB.423727

Conference publications

S. Y. Haffert, R. J. Harris, A. Zanutta, **F. A. Pike**, A. Bianco, E. Redaelli, A. Benoît, D. G. MacLachlan, C. A. Ross, I. Gris-Sánchez, M. D. Trappen, Y. Xu, M. Blaicher, P. Maier, G. Riva, B. Sinquin, C. Kulcsár, N. Ali Bharmal, E. Gendron, L. Staykov, T. J. Morris, S. Barboza, N. Muench, L. Bardour, L. Prengère, H. Raynaud, P. Hottinger, T. Anagnos, J. Osborn, C. Koos, R. R. Thomson, T. A. Birks, I. A. G. Snellen, C. U. Keller, L. Close, J. R. Males, "Multi-core fibre-fed integral-field unit (MCIFU):

overview and first-light," *Proc. SPIE* 11448*, Adaptive Optics Systems VII,* 114484M (2020); https://doi.org/10.1117/12.2562719

F. A. Pike, A. Benoit, D. G. MacLachlan, C. A. Ross, R. J. Harris, S. Y. Haffert, I. Gris-Sánchez, T. A. Birks, R. R. Thomson, "Multi-core fiber–fed integral field spectrograph (MCIFU) – III: an ultrafast laser inscribed photonic reformatter and mask," *Proc. SPIE* 11451*, Advances in Optical and Mechanical Technologies for Telescopes and Instrumentation IV,* 1145166 (2020); https://doi.org/10.1117/12.2559197

R. J. Harris, **F. A. Pike**, M. Trappen, S. Y. Haffert, Y. Xu, A. Benoît, C. Ross, D. G. MacLachlan, S. Barboza, N. Münch, I. Gris-Sánchez, M. Blaicher, P. Maier, C. Koos, T. A. Birks, R. R. Thomson, "Multi-core fibre-fed integral field spectrograph (MCIFU) IV: the fiber link," *Proc. SPIE* 11451*, Advances in Optical and Mechanical Technologies for Telescopes and Instrumentation IV*, 1145124 (2020); https://doi.org/10.1117/12.2562689

F. A. Pike, A. Benoit, D. G. MacLachlan, R. J. Harris, I. Gris-Sánchez, D. Lee, T. A. Birks, R. R. Thomson, "Modal noise mitigation in a photonic lantern fed near-IR spectrograph," *Proc. SPIE* 11451*, Advances in Optical and Mechanical Technologies for Telescopes and Instrumentation IV*, 114510E (2020); https://doi.org/10.1117/12.2561644

F. A. Pike, T. K. Sharma, A. Benoît, D. G. MacLachlan, A. N. Dinkelaker, A. S. Nayak, K. Madhav, M. M. Roth, L. Labadie, E. Pedretti, T. A. ten Brummelaar, N. J. Scott, V. Coudé du Foresto, R. R. Thomson, "K-band integrated optics beam combiners for CHARA fabricated by ultrafast laser inscription," *Proc. SPIE* 11446*, Optical and Infrared Interferometry and Imaging VII*, 114460K (2020); https://doi.org/10.1117/12.2561663

Chapter 1 - Introduction

1.1 Types of astronomy

Astronomy is the study of everything beyond our planet. To perform astronomy, we use telescopes to collect signals from objects in order to gain information about them. Until recently, all astronomy was performed by collecting and analysing electromagnetic waves, from Gamma-rays to radio-waves, with each wavelength band providing different information about a particular object. Gamma-rays, for example, are emitted by only the most energetic processes in the universe, and so Gamma-ray astronomy is performed to observe and understand objects such as supernovae and pulsars. At the other end of the electromagnetic spectrum, radio-wave astronomy can be used to observe the distribution of interstellar gas, particularly Hydrogen through its spectral line at a wavelength of 21 cm.

It is important to recognise that astronomy can also be performed using signals that are not electromagnetic in nature. Neutrino astronomy, for example, uses underground facilities such as the Deep Underground Neutrino Experiment (DUNE) facility currently under construction in South Dakota – US, to detect neutrinos generated by astrophysical objects. Applications for neutrino observations include studies of black holes, galactic supernovae and indirect searches for dark matter. Gravitational wave astronomy also does not rely on the detection of electromagnetic signals. Instead, large optical interferometers, such as the Laser Interferometer Gravitational-Wave Observatory (LIGO) in Hanford, Washington – US, are used to detect time-varying distortions in spacetime as gravitational waves propagate through the interferometer. The astronomical applications for this form of astronomy are focused on the observation of astrophysical events that can generate strong gravitational waves, examples of which include black hole mergers and neutron star collisions.

In this thesis, we are primarily concerned with developing new photonic technologies for applications in near-infrared astronomy between ~ 1.1 μm and 2.4 μm. This encompasses the Y– (~0.95 μm to ~1.05 μm), J– (~1.1 μm to ~1.4 μm), H– (~1.5 μm to ~1.8 μm) and K– (~2.0 μm to ~2.4 μm) bands where the Earth's atmosphere exhibits high transparency. An illustration of the relative positions of these bands is given by

Figure 1. Notably, the observational challenge of the increasing thermal background in K-band (and beyond) neccessitates improved instrumentation capabilities.
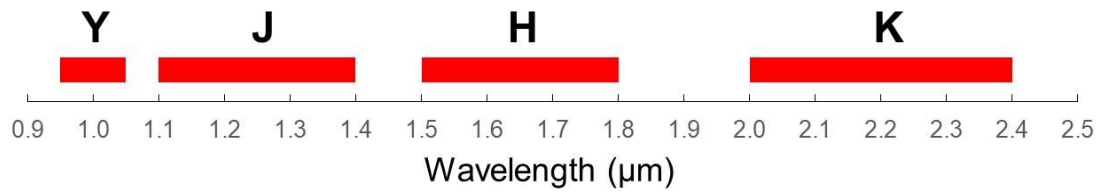
Figure 1: Relative positions and spans of selected near-infrared astronomical bands. The gaps are due to atmospheric absorption.

Observations in these spectral regions have countless applications in astronomy, examples of which include:

High redshift studies - spectroscopic lines such as the H-alpha (Hα) and Lyman-alpha (Ly-α) lines, which reside at 656.3 nm and 121.6 nm respectively in the rest frame, are rapidly redshifted into the near-infrared. Thus, near-infrared K-band astronomy can be used to observe objects at redshifts z > 2 using Hα emission, and J-band at redshifts z > 8 using Ly-α emission, enabling deep observations of the early Universe which are key to understanding some of the "big questions" including: *What is the nature of dark energy and dark matter? How and when do the first stars form? How and when did the universe reionize?* [1]

Studies of cool objects - Wein's displacement law states that the spectral peak of the blackbody emission from an object at temperature (T) occurs at a wavelength (λ_{max}) given by Equation 1:

$$\lambda_{max} = \frac{b}{T}$$

Equation 1

where b is Wein's displacement constant (2898 μm.K).

This means that the near-infrared is a crucially important region for observing cooler objects such as M-dwarf stars which exhibit surface temperatures between 2,000 K and

3,600 K, meaning that their peak blackbody emission is the near-infrared between ~1.5 μm and 800 nm respectively.

Studies of dust obscured objects – the scattering of light by dust is strongly wavelength dependent and is due to a combination of both Rayleigh scattering, where the dimensions of the scattering particles are much smaller than the wavelength of the light, and Mei scattering, where the scattering particles are bigger than the wavelength of the light. The strength of Rayleigh scattering exhibits a λ^{-4} dependency, meaning that near-infrared observations can be used to observe dust obscured objects such as the galactic centre and star forming regions.

In summary, the near-infrared will be an incredibly important area in astronomy for decades to come. In this thesis, I present the results of three investigations aimed at developing new photonic technologies (astrophotonic technologies) for applications in near-infrared astronomy. The remainder of the thesis will therefore focus on only discussing aspects that are relevant to near-infrared astronomy.

1.2   What is an astronomical instrument?

Facility class telescopes are complex beasts, and cutting edge telescopes are some of the most advanced scientific facilities in existence. From an optical perspective, the key components are the telescope itself, which is used to collect and focus light to the telescope focal plane, and the astronomical instruments. On a ground-based telescope, these astronomical instruments might include an adaptive optics (AO) system to "undo", at least partially, the aberrations imparted on the incoming optical wavefront by the atmosphere in quasi-realtime, or an "analysis instrument", such as a spectrograph, to analyse the spectral properties of the light collected. Other analysis instruments include cameras equipped with coronagraphs for directly imaging exoplanet systems, or interferometric beam combiners for coherently combining the light gathered by multiple telescopes which form an interferometer array.

Astronomical instruments come in countless different shapes and sizes. In the case of facility class instruments they are usually highly bespoke to the specific telescope and either a specific science case or collection of science cases. In the following section, I

provide a brief overview of some specific instruments and types of instrument that have been developed for applications in optical and near-infrared astronomy.

1.2.1 High resolution single object spectrographs

The resolution (R) of a spectrograph, where $R = \frac{\lambda}{d\lambda}$, limits the precision with which spectral features within the light from an object can be identified. High resolution spectrographs, which operate at resolutions upwards of $\sim R = 50,000$ are therefore key to many areas of astronomical science, examples of which include, but are not limited to:

Characterising exoplanet atmospheres – At low resolution, spectral lines overlap in the acquired spectra. This means that ground based observations are "contaminated" by the spectral signatures of the Earth's atmosphere. In order to perform spectroscopic analysis of exoplanet atmospheres it is essential to work at high resolution to separate out the planetary, stellar and telluric spectral features using their differential radial velocity shifts.

Radial velocity measurements – Exoplanets can be detected in a variety ways. They can be directly imaged using telescopes equipped with AO systems and a camera behind a coronagraph. They can also be detected from the periodic dip in the apparent stellar brightness they induce as they move in between the telescope and the star. However, both of these techniques suffer from one major drawback – they do not provide information about the mass, and therefore density, of the planet. This information is key in the search for life, as we believe that rocky, high density planets are required to support life.

The only technique that we currently have available for "weighing" extrasolar planets is the radial velocity (RV) technique. The basic physical concept exploited in the RV technique is shown in Figure 2. Here it can be seen that both the star and the exoplanet orbit around their common centre of mass. This means that as the star moves periodically away and towards an observer, the observer will detect a periodic modulation in the stellar spectrum due to the Doppler shift. Since the magnitude of the Doppler shift is dependent on the period and radius of the stellar orbit, and since this is

in part dependent on the mass of the companion, RV measurements provide a route to measure the mass of the companion.
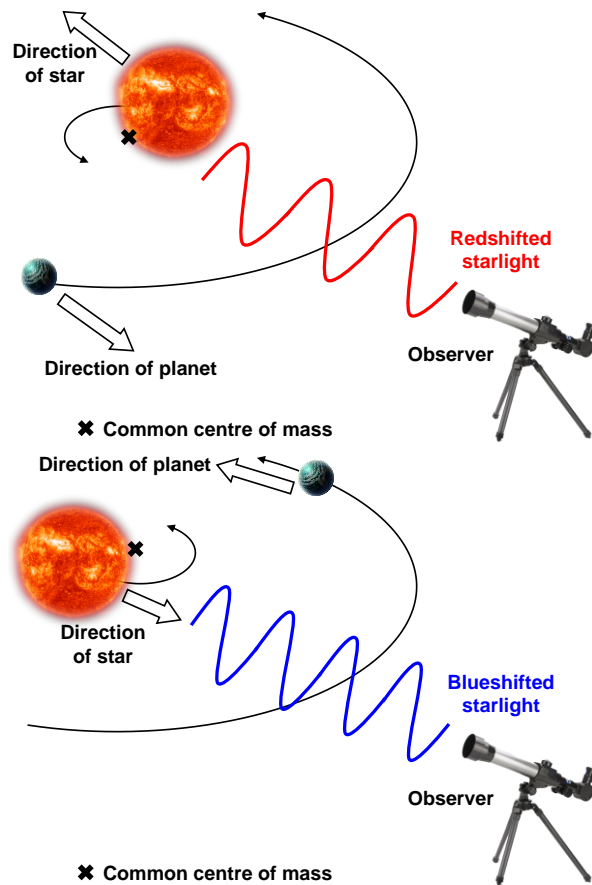
Figure 2: Schematic of Doppler shift due to radial velocity of observed star.

Again, the resolution of the spectrograph directly limits the precision of any RV measurement. For example, the HARPS spectrograph (High Accuracy Radial velocity Planet Searcher) at the ESO La Silla 3.6 m telescope in Chile operates between 378 nm and 691 nm, exhibits a spectral resolution of ~120,000, and is able to generate spectra with a precision of ~ 1 m.s^{-1} [2].

The Sandage-Loeb test – One of the most exciting, but also most challenging, applications for high resolution astronomy in the coming decades is the so-called Sandage-Loeb test for the realtime expansion of the Universe. The basic idea of the test is to measure the drift in the Ly-α forest absorption lines of distant $z \geq 2$ quasars, and by doing so detect the change in the acceleration of the Universe. The change in the redshift is only expected to be a few cm.s^{-1} [3], and so these measurements will require velocity measurements over decades with a precision of a few cm.s^{-1} using high resolution spectrographs.

1.2.2   Multi-object spectroscopy instruments

Single object spectrographs detect and analyse the light from one object at a time. There are, however, astronomical applications that require the spectroscopic analysis of many objects, and sometimes many thousands of objects in order to build up statistically significant data sets. These applications require a multi-object spectroscopy (MOS) instrument, which usually consists of a spectrograph coupled with a "selector" of some kind that allows astronomers to select regions of the telescope focal plane for spectroscopic analysis. At one end of the technology spectrum the selector can be something as simple as a bespoke slit-mask, as is the case for the MOS instrument at Gemini. The slit mask is designed and fabricated such that it only allows light from selected regions of the focal plane to enter the spectrograph for analysis. At the other end of the technology spectrum, the selector can consist of a system of robotically controlled arms with mirrors attached to redirect light from specific parts of the focal plane into a spectrograph, as is the case for KMOS at the VLT [4].

Early MOS systems, such as the 2dF fiber positioner and spectrograph system at the Anglo-Australian Telescope (AAT) [5], were capable of generating spectra for multiple objects simultaneously, but not capable of generating spatially resolved spectra across the objects. New MOS systems are addressing this by enabling the deployment of multiple integral field units (IFUs) across the focal plane. Each of the 24 robotically controlled mirrors in KMOS, for example, projects light onto an image slicer that then splits each sub-field into 14 slices with 14 spatial pixels along each slice. For applications that would benefit from higher multiplex gains, new approaches are being developed that would utilise optical fibre-based IFUs. The SAMI system at the AAT utilised a plug-plate assembly to precisely position 13 "hexabundles" across the image plane [6]. Each of these hexabundles consists of 61 optical fibres closely packed together to collect spatially resolved light from 13 objects. The light from these fibres was then coupled into the AAOmega spectrograph to provide spectrally resolved "imaging" of the object. This photonic approach to MOS IFUs is now being extended to Hector-I, which will consist of 21 hexabundles, and there are future plans for Hector-3df which will utilise around 90 such IFUs.

1.2.3 Beam combiners for interferometry

Due to diffraction, the angular resolution of an image acquired using a single telescope is limited to ~λ/D, where λ is the wavelength of the light used to perform the imaging, and D is the diameter of the telescope aperture. Even if diffraction limited performance were possible with perfect AO, even the ELT with a 39 m primary mirror would exhibit an angular resolution of ~10 mas in the K-band (~2.0 μm to ~2.4 μm – a region of crucial importance for observations of cool objects such as exoplanets and for observations of objects obscured by dust). This angular resolution, and the resulting spatial precisions it enables, are too low for a number of important astrophysical applications, including tests of how the effects of general relativity impact the orbits of stars around supermassive black holes, spatially resolved images of stellar surfaces, and the precision characterisation of exoplanet systems using astrometry.

Stellar interferometry is the technique that allows us to overcome the angular resolution limitations of single aperture telescopes by combining the light collected by multiple widely spaced telescopes, as shown in Figure 3. In radio frequency astronomy, the carrier frequency of the signal is sufficiently low that the radio signals can be fully recorded by each of the multiple telescopes that form the interferometer. These signals can then be combined at some time after detection using computer analysis. However, in the near-infrared domain, the carrier frequency is in the THz domain, and no detector has sufficient bandwidth to resolve the shape of the waveform at these frequencies. Although research is ongoing to use heterodyne techniques, which involve mixing the astronomical signal with a local laser oscillator to record both the amplitude and the phase of the astronomical signal, the only option currently for stellar interferometry in the optical and near-infrared domains is to coherently combine the light gathered by the telescopes in the interferometer using an instrument called a beam combiner.

The task that a beam combiner operating at optical and near-infrared wavelengths must perform is to take the light from each pair of telescopes in the interferometer, and combine it optically such that the mutual coherence between the two telescopes can be interrogated while a variable optical delay line is used to introduce controllable path differences between the telescopes. If this is performed correctly, it can be shown that a two telescope beam combiner will record, as a function of the optical path difference (OPD), an optical signal (I) given by Equation 2:

$$I(\nu_0, \Delta\nu) = 1.0 + T(I_1, I_2)V(\nu_0)\sin(\pi\ OPD\ \Delta\nu)\cos\left(2\pi\nu\ OPD + \phi(\nu_0)\right)$$

<div align="right">*Equation 2*</div>

Where ν_0 is the central frequency of the signal, $\Delta\nu$ is the frequency bandwidth of the optical signal, T is the transfer function $T(I_1, I_2) = \frac{2I_1 I_2}{I_1^2 + I_2^2}$, and V is the fringe packet visibility.

It is knowledge of the fringe visibility, V, that is primarily required from the beam combiner since, according to the Van Citter-Zernike theorem, this visibility is exactly proportional to the amplitude of the image Fourier component with a spatial frequency of $u = \frac{b}{\lambda}$, where b is the interferometer baseline projected onto the sky, and λ is the wavelength of the light.

A complete image of the object can be reconstructed using algorithms together with data that is acquired by filling in the Fourier u- v plane with multiple measurements as the Earth rotates, and by using interferometer arrays with multiple telescopes and therefore multiple baselines. This capability is currently possible at multiple sites around the world, including the VLTI in Chile, NPOI in Arizona, and CHARA in California.

In Chapter 4 of this thesis, we report the development of achromatic 3dB integrated optic K-band beam splitters using a laser fabrication technique known as ultrafast laser inscription. These components will form the operational heart of a future two-telescope integrated optic beam combiner which will eventually replace the JouFLU instrument at CHARA.
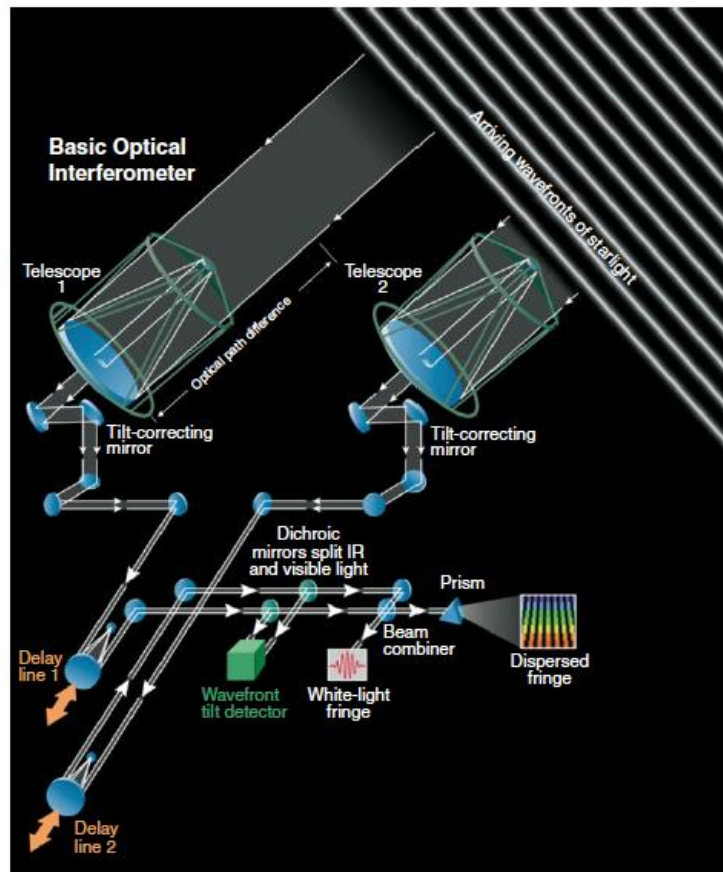
Figure 3: Schematic diagram of the key components of a two-telescope stellar interferometer. Reprinted/adapted by permission from Springer Nature: Optical and Infrared Interferometers by Theo A. ten Brummelaar and Harold A. McAlister © (2013)[7] .

1.3 Astrophotonics

1.3.1 What is astrophotonics and why is it exciting?

According to UNESCO, the field of photonics is "*...the science and technology of generating, controlling, and detecting photons, which are particles of light.*" This is an incredibly broad definition and, in my opinion, slightly misleading, since the reference to the particle nature of light would to suggest that photonic devices must utilise a quantum property of light. This is far from true, and there are, in fact, many truly photonic technologies, such as optical fibres, spatial light modulators and DVDs, which operate purely using classical wave properties of light. In reality, the field of photonics is vast, so vast in fact that it essentially encompasses conventional optics.

This thesis is all about developing photonic technologies and techniques for future applications in astronomy – a field that has become known as *astrophotonics*. So what

makes an emerging technology with potential applications in astronomy *astrophotonic*, rather than just an emerging astronomical technology? Given the discussion in the paragraph above regarding the differences between the fields of photonics and optics, the only conclusion one can draw here is that astrophotonic technologies are simply new optical technologies for astronomy, and that an emerging technology is "*particularly astrophotonic*" if the approach has never been considered for applications in astronomy before.

Despite this rather unsatisfying clarification of the difference between astronomical technologies and astrophotonic technologies, it would be fair to say that there has, over the past few decades, been an increasing willingness to consider the applications of certain photonic technologies in astronomy that would have previously been thought of as irrelevant for astronomy, such devices include fibre Bragg-gratings (FBGs) for filtering unwanted atmospheric lines from the celestial light of interest [8], integrated optics to realise high-stability, high-baseline-number, beam combiners for stellar interferometry [9], and laser frequency combs for precision calibration of spectrographs [10]. In the following, I provide a brief overview of some of the astrophotonic technologies that have been developed to date.

1.3.2   Examples of astrophotonic technologies

1.3.2.1   Integrated beam combiners for stellar interferometry

In Section 1.2.3, I briefly discussed how stellar interferometry, utilising multiple widely spaced telescopes in an interferometer array, can be used to obtain an image of an astronomical object with an angular resolution that is significantly higher than the resolution that can be achieved using any of the individual telescopes. To enable the interferometry, the mutual coherence between the light collected by each pair of telescopes within the array must be determined using an instrument known as a beam combiner.

Beam combining instruments have been constructed for decades using conventional bulk optic approaches with mirrors and beam splitters, and some have had considerable success. A particular example here is AMBER at the VLTI [11], shown in Figure 4, which is capable of coherently and simultaneously combining the light gathered by either three of the four 1.8 m auxiliary telescopes, or the three of the four 8.2 m unit

telescopes. In order to utilise the full capabilities of the VLTI it was highly desirable to combine the light from all four telescopes in the array. Since the number of baselines in an interferometer is $\frac{(n^2-n)}{2}$, combining all four telescopes, rather than three, doubles the number of baselines to 6, rather than 3. This is a significant technical challenge for bulk optic beam combiners, but integrated optics can provide a solution by using lithographically defined integrated optical waveguides to route, reformat and interfere the light from the different telescopes in the array.

Although the concept of using integrated optics for improved beam combiners was first proposed by Kern et al in 1997 [12], it was not until PIONIER successfully combined all four of the 8.2 m unit telescopes in 2011 that the full potential of astrophotonic beam combiners in stellar interferometry was realised [13]. PIONIER operates in the H-band and utilises an integrated optic beam combining circuit, see Figure 5, to provide 24 simultaneous interferometric outputs - 4 for each baseline in an "ABCD" modality to provide unambiguous phase information. The impact of using an integrated optic beam combiner on the complexity of the instrument can be seen in Figure 6. The success of PIONIER subsequently led to the development of the K-band GRAVITY instrument [9] at the VLTI which also utilises a photonic beam combining component. GRAVITY has recently achieved a series of remarkable results, such as the first direct detection of an exoplanet by optical interferometry [14] and direct imaging of the effect of general relativity on the path of a star orbiting the galactic centre [15].

Figure 4: Composite image of the bulk optic AMBER beam combiner instrument. Credit: R. G. Petrov et al., A&A 464, 1-12, 2007, reproduced with permission © ESO [11].

Inputs   Tricouplers   Combining functions   Outputs

3 4
1 2
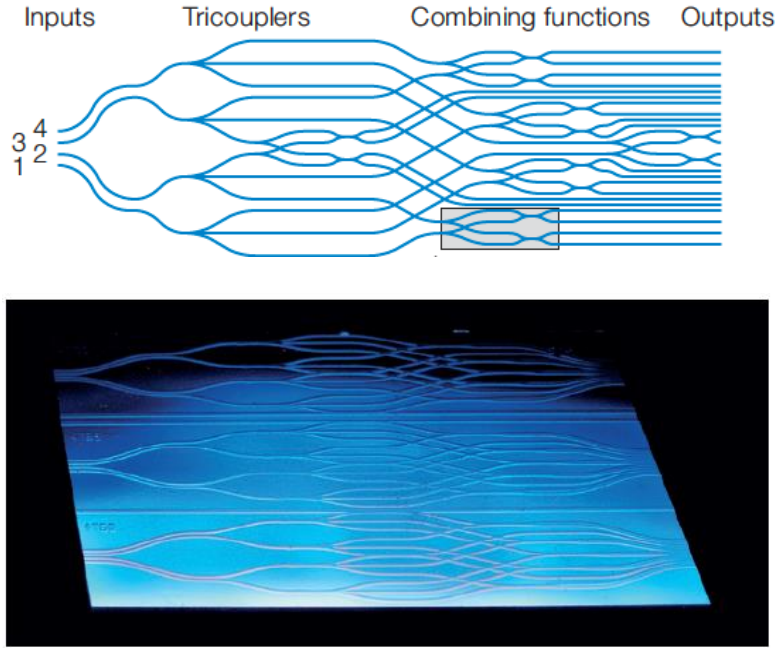
Figure 5: (Top) Waveguide layout for the integrated waveguide beam combiner used in PIONIER, (bottom) photograph of the integrated beam combiner. Adapted/reproduced from Zins et al. 2011, The Messenger, vol 146, credit: ESO/Zins et al [13].
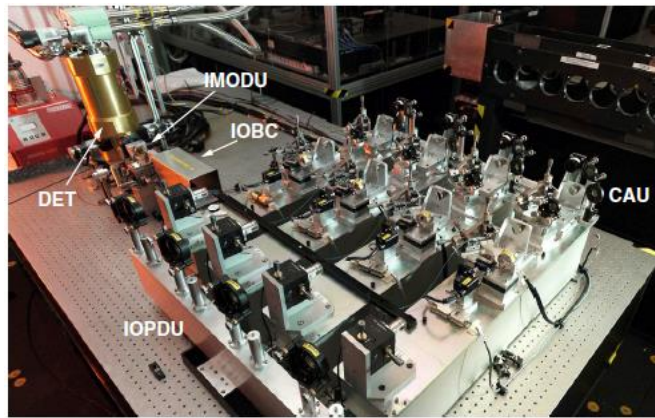
Figure 6: Photograph of the PIONIER beam combiner instrument at the VLTI. The integrated optic component sits in the housing marked "IOBC."Credit: J.-B. Le Bouquin et al., A&A 535, A67, 2011, reproduced with permission © ESO [16].

1.3.2.2   *FBGs for OH-line suppression*

As discussed in Section 1.1, the near-infrared will be a spectral region of key importance for astronomy in the coming decades, for applications ranging from cosmology to exoplanet science. Many of these applications will benefit from the light gathering capacity provided by large ground based telescopes with apertures >10 m. This, however, presents a problem for deep observations, since the Earth's atmosphere

is somewhat bright at night in the near-infrared due to the emission from excited OH radicals that reside at an altitude of ~90 km. When these OH radicals decay, they produce a forest of OH-emission lines throughout the J-, H- and K-bands. The OH lines are multiple orders of magnitude brighter than either the zodiacal scatter or the thermal emission from the telescope, and therefore prevent instruments from reaching their optimal performance capabilities if they are allowed to enter the instrument.

One positive feature of the OH-lines is that they are expected to be extremely narrow spectrally with a FWHM linewidth below ~1 Å [1], meaning that the spectral regions between the lines should remain very dark. This opens up the possibility of using a complex optical filter placed before an instrument to separate (reflect) the unwanted OH-lines from the light contained in the spectral regions between the lines. The specifications of such a filter are extremely demanding, as it should ideally suppress >100's of OH-lines across 100's of nm of bandwidth, each with a reflection band of perhaps 0.5 nm, while simultaneously efficiently (sub-dB losses) passing the light between the reflection bands. This is well beyond anything that can be achieved currently using thin film coating technologies.

One technology that can, in principle, provide the capabilities require for the OH-emission spectral filtering application is the single-mode FBG. These are single mode fibres which have imprinted on them a refractive index modulation which effectively acts as an interference filter. Normally, FBGs are fabricated with a simple sinusoidal modulation in the refractive index to reflect a single spectral notch, but it is also possible to design and fabricate extremely complex FBGs that can simultaneously reflect many 10's of spectral notches. This is exactly the approach that has been pursued by Bland-Hawthorn et al [17], who have successfully develop OH-suppressing FBGs which suppress 103 of the brightest OH doublets in the 1.47-1.7 μm range, with a throughout of ~60% between the lines. These filters were used to filter light collected by the AAT before coupling into the IRIS2 spectrograph. Unfortunately, the interline continuum between the suppressed spectral regions was not observed to be significantly darker than measurements that were obtained without the OH-suppression [17]. This suggests that in this case the background is still dominated by emission from non-suppressed atmospheric emission and work is ongoing to investigate this.

1.3.2.3   *Photonic spectrographs for astronomy*

Atmospheric turbulence, also known as atmospheric "seeing" causes the angular width of the telescope point spread function to increase beyond the diffraction limit. A larger point spread function means that the slit-width of a spectrograph coupled to the telescope must also increase to maintain efficient throughput. This in turn means that the spectrograph size must increase to maintain the required spectral resolution. These relationships mean that since the impact of seeing becomes worse as the telescope aperture increases, larger telescopes also generally require larger spectrographs.

One option to break this scaling is to use AO, and with perfect AO the PSF would be independent of the telescope size. Unfortunately, although AO can deliver extremely high levels of correction over small fields of view, the level of correction possible over the larger fields of view necessary in MOS systems is limited, meaning that MOS spectrographs are becoming extremely large. The spectrograph for KMOS, for example, which is installed on the 8-metre VLT is multiple m^3 in size, housed in a 2 m diameter cryostat, and weighs 2700 kg [4].

With the issues above in mind, researchers have started to investigate whether photonic technologies could provide a solution. The basic idea here would be to use photonic approaches to modularise the MOS system, such that light from each object, or each part of an object, was routed to a mass-producible photonic spectrograph. These spectrographs could utilise new photonic spectrometer concepts such as photonic crystal superprisms [18], the stationary-wave integrated Fourier-transform spectrometry (SWIFTS) concept presented in Figure 7 [19], or more established technologies such as arrayed waveguide gratings (AWGs) [20], an example layout of which is presented in Figure 8.
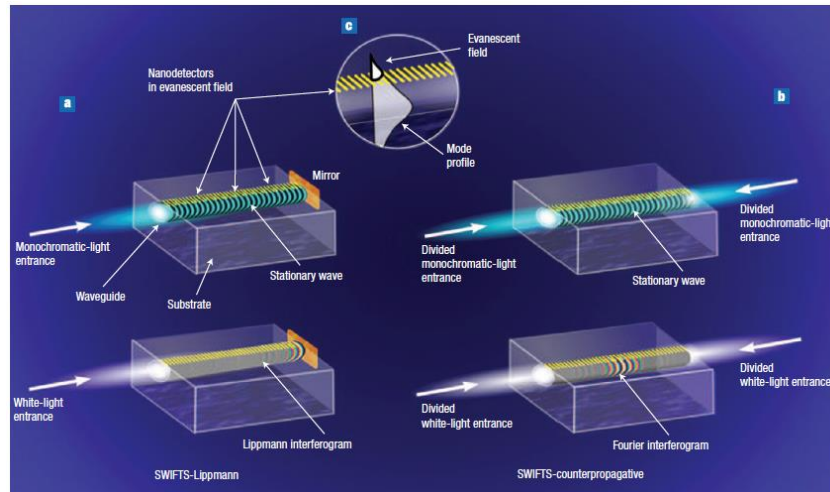
Figure 7: Conceptual diagrams of the SWIFTS photonic spectrometer concept using the Lippmann configuration, where light is coupled into a waveguide with a mirror at one end. This establishes a standing wave white light interferogram, the near field of which can then be sampled using nanodetectors placed on the waveguide surface. In the "counterpropagative" mode the light is divided into two and coupled into either end of the waveguide to establish the interferogram at some point in the middle of the waveguide. In this case, the relative phases of the light will control the positioning of the interferogram. Reprinted by permission from Springer Nature: Nature Photonics, Wavelength-scale stationary-wave integrated Fourier-transform spectrometry, Etienne le Coarer et al, © (2007).
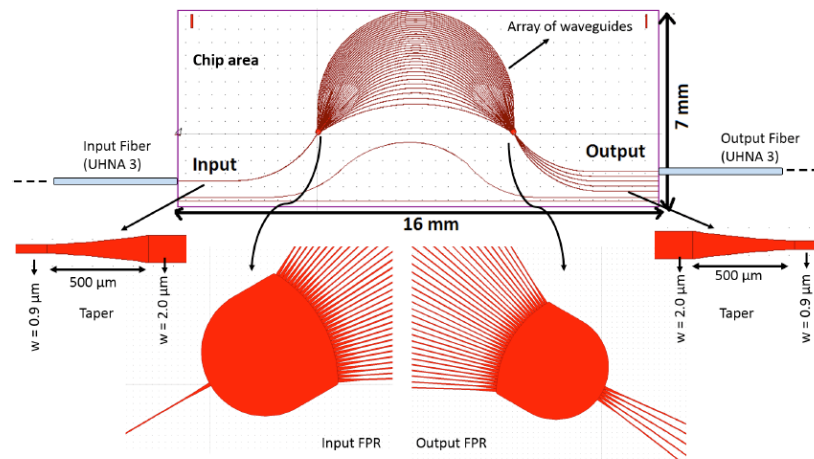
Figure 8: Schematic of the layout of an integrated photonic arrayed waveguide grating (AWG) spectrometer. Light is coupled into the arrayed waveguide via an input free-space propagation region (FPR). The arrayed waveguides each have a set path length difference between adjacent waveguides to generate the wavelength dependent dispersion. Different wavelengths are then focused to different positions at the output of the second FPR. Reprinted with permission from [20] © The Optical Society.

AWGs are the integrated photonic version of a conventional high order Echelle grating based spectrometer, and have so far attracted the most attention for astronomical applications. However, although it is notable that such devices have even been tested on sky [21], there is some doubt about the level of advantage a modular approach to MOS would provide in terms of size, cost and scientific output [22]. Part of this doubt stems from the fact that when an AWG is used to process broadband astronomical signals, the output of an AWG must be cross dispersed onto a two-dimensional detector array to prevent different signals from different wavelengths overlapping on the detector. Science grade detectors are extremely expensive, and developing a modular approach to MOS that then requires a science grade detector for every object is not a solution. It could well be the case that the future of AWG based spectroscopy in astronomy lies in high resolution single object instruments, where the integrated nature of the AWG could allow a significantly smaller instrument, with resultant advantages in terms of cost and stabilisation.

1.3.2.4 *Photonic lanterns*

Although it is not the only determining factor, the efficiency with which the PSF of a telescope can be coupled into a photonic device is fundamentally limited by mode-number-matching – if the number of modes that form the PSF (M_{PSF}) is larger than the number of modes supported by the photonic devices (M_{Device}), the efficiency of the injection can be expected to be limited to $\sim \frac{M_{Device}}{M_{PSF}}$. This is potentially problematic for many astrophotonic devices, such as the AWG-based photonic spectrographs, and the FBG-based OH-line filters, discussed previously, because these devices are single mode photonic devices. By single mode, we mean that they only guide light with one well defined intensity distribution – the fundamental mode. In the case of single mode optical fibres, this mode is a rotationally symmetric mode with a Gaussian-like cross sectional intensity distribution. In the case of single mode integrated optic devices, which are fabricated using planar optical waveguides, the propagating light is free to change shape in the plane of the slab, but can only exhibit a Gaussian-like intensity distribution across the core slab. To put this in some context, we can consider the situation of the 3.58 m diameter Telescopio Nazionale Galileo (TNG) in La Palma, a site which exhibits a median seeing of ~0.6 arcsec, and use Equation 3 and Equation 4 to calculate that we would expect ~75 modes to form the PSF for 950 nm light, reducing to ~12 for 2,500 nm light . If we were to try and couple this PSF to a single mode fibre,

we would expect to lose a minimum of ~99% of the light on average at 950 nm, and a minimum of ~92% of the light on average at 2,500 nm.

$$M_{PSF} \approx \left(\frac{\pi \, \theta_{Focus} D_T}{4\lambda} \right)^2$$

$$\theta_{Focus} \approx \sqrt{(\lambda/D_T)^2 + \theta_{Seeing}(\lambda)^2}$$

One option to address the efficiency limitations discussed above is to use AO. If the AO operates perfectly, which is nearly possible for narrow field of view extreme AO systems such as SCExAO on SUBARU [23], then θ_{Seeing} in Equation 4 becomes 0, and the number of modes that form the PSF = 1, regardless of wavelength. In other words, the telescope operates at the diffraction limit. Exactly this approach is being pursued for coupling light from single unresolved stars efficiently into single mode fibres [23], but this approach is not suitable for the vast majority of applications, and certainly not for MOS instruments. If astrophotonic components such as AWG spectrographs and FBG filters are to be used efficiently on seeing limited telescopes, then another approach is required that allows the multimode PSF to be efficiently coupled into single-mode photonic devices.

The challenge of efficiently coupling the multimode PSF of a telescope into single mode photonic devices may sound an impossible one, and indeed it would be if we wished to efficiently couple multimode light into one single mode. The trick we can play here is to use a guided wave transition, known as a "photonic lantern" to gradually transform the modes of a multimode fibre, to which the PSF can be efficiently coupled, into an array of single modes, as shown schematically in Figure 9.
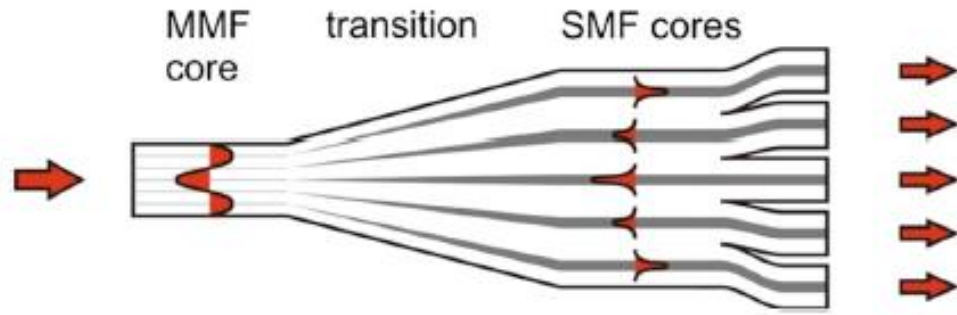
Figure 9: Schematic of how a photonic lantern, in this case a lantern that might be fabricated using a tapered bundle of optical fibres, can be designed to efficiently transform the modes of the multimode fibre (MMF) end into the modes of the single mode fibre (SMF) cores at the other end. Reprinted with permission from [24] © The Optical Society.

Photonic lanterns can be fabricated in a variety of different ways, and for a full description of the history of these devices the reader is referred to this review [25]. The most common techniques used to fabricate photonic lanterns include the "tapered bundle" technique, whereby a bundle of single mode fibres are placed inside a low-index capillary and tapered to create the photonic lantern transition [26], the multicore fibre approach [27], whereby a multicore fibre is placed inside a low-index capillary and tapered to create the photonic lantern transition, and ultrafast laser inscription (ULI) [28] - a laser based fabrication technique which uses ultrashort pulses of laser light to write three-dimensional optical waveguide structures inside a glass substrate.

Each type of lantern has its own advantages. The tapered bundle lanterns have the advantage that the multimode light is coupled to many individual single mode fibres, and this then facilitates the easy coupling of the light to individual OH-line suppressing FBGs [8]. The MCF-lanterns have the advantage that the lanterns can be easily mass-produced, and might enable OH-suppressing gratings to be fabricated across all cores of the MCF in one go (a capability yet to be proven) [27]. The ultrafast laser written lanterns exhibit the advantage that once the multimode PSF has been transformed into single modes, these can then be arbitrarily arranged and manipulated, for example for coupling to a spectrograph operating at the diffraction limit [29].

The fact that photonic lanterns enable the efficient interfacing of multimode light with single mode photonic devices make them a truly enabling technology in the field of astrophotonics. Without them, all but a few astrophotonic concepts would remain exactly that – concepts. Photonic lanterns are the key that opens the door to high impact astrophotonic applications, such as efficient high resolution OH-line suppression in MOS systems (both traditional and astrophotonic versions). Although there remains significant technical issues for such a vision to become reality, the scientific pull appears strong enough to provide the resource to solve these challenges over the next ~decade.

1.3.2.5   *Laser frequency combs (LFCs)*

The precision with which a spectrograph can measure the spectrum of a signal is dependent on many parameters, including its spectral resolution, efficiency, stability and calibration. The last of these is usually performed using sources such as I_2 cells and Th-Ar lamps, but these generate irregular line spacings and intensities (in the case of the lamps) which limit the precision of the calibration possible. One astrophotonic technology that can solve this is the laser frequency comb (LFC).

An LFC can be created in a number of ways, but one of the most common is to use a modelocked laser. In such a laser, the cavity is controlled such that the cavity modes oscillate in a phase coherent manner with one another. This means that knowledge of the frequency of one mode can be used to determine the frequency of another mode. The phase coherent nature of the modelocked laser modes means that it generates pulses of light with a temporal separation equal to the cavity round trip time. The time evolution of the electric field, $E(t)$, can therefore be represented by:

$$E(t) = A(t)e^{i\omega_c t}$$

Where $A(t)$ is the pulse envelope and ω_c ($\omega_c = 2\pi \nu_c$) is the angular frequency of the carrier wave.

The periodic nature of the pulses in turn means that the time evolution of the electric field can also be represented by a period Fourier series:

19

$$E(t) = \sum_{N=N_i}^{N_f} A_N e^{i\omega_N t}$$

Where A_N and ω_N ($\omega_N = 2\pi \nu_N$) are the Fourier amplitude and angular frequency of the Nth mode respectively.

There are no physical properties of the laser cavity that require ν_c to precisely align with a laser mode, and so since the frequency difference between adjacent modes is equal to the pulse repetition frequency of the laser, the positions of the comb modes can be defined as residing at the following frequencies:

$$\nu_N = N.f_r + f_o$$

Where f_r is the pulse repetition frequency and f_o is known as the carrier offset frequency.

In an LFC, a variety of techniques are used to stabilise the carrier offset frequency, such that the whole comb becomes spectrally stable. The key feature here is that f_r and f_o can be locked to atomically traceable standards such as a Cs clock. This in turn means that the spectral positions of all the teeth in the LFC are, in principle, traceable back to the precision of an SI standard.

As shown in Figure 10, the ruler-like nature of laser frequency combs make them the perfect tool for calibrating astronomical spectrographs, where it can be seen that by coupling the light from an LFC into the slit of a spectrograph, the detector is illuminated with thousands of comb modes with precisely known separations and frequencies. This is in stark contrast to the Th-Ar lamp, which illuminates the detector with sparsely positioned lines of variable intensity. Furthermore, given that the comb could be referenced against satellite atomic clocks that form the GPS constellation and exhibit frequency stabilities $< 2 \times 10^{-13}$ [30], it is clear that LFCs open a route to cm.s^{-1} and even sub-cm.s^{-1} calibration of astronomical spectrographs. Indeed, LFCs have already been used to calibrate the HARPS / FOCES [31] down to a precision of ~2.5 cm.s^{-1}.
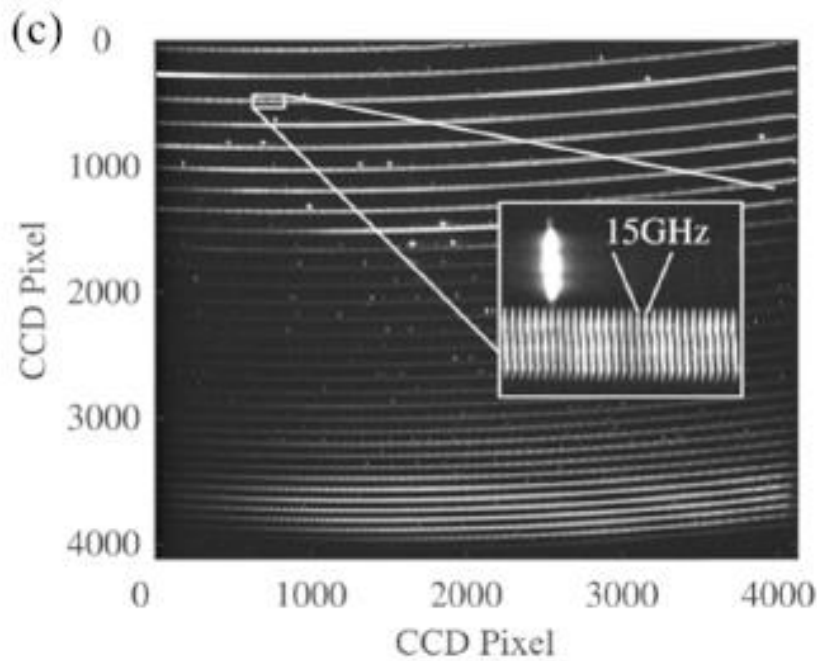
Figure 10: Two dimensional representation of the CCD detector signal obtained from the High Resolution Spectrograph (HRS) at the South African Large Telescope when using either a Th-Ar lamp (bright specs) or a laser frequency comb (teeth). Adapted with permission from [10] © The Optical Society.

1.3.2.6 *Astrophotonic devices not discussed*

In this section I have discussed a selection of some of the most important and high profile astrophotonic technology concepts that are being pursued. It is important to highlight that there are many more that I have not discussed. These include integrated waveguide pupil remappers [32], photonic-lantern-based mode-scramblers [33], laser printed micro-lens arrays [34] and photonic-lantern-based wavefront sensors [35] to name just a few, and some of these will be discussed in the following chapters. For further details on more astrophotonic technologies, the interested reader is referred to the astrophotonics special issues in Optics Express in 2009 and 2017, and the 2021 astrophotonics special issue in Applied Optics / Journal of the Optical Society of America B.

1.4 Ultrafast laser inscription (ULI)

This thesis is focused on the development of three new astrophotonic technologies and techniques for a variety of applications in astronomy. A unifying aspect of these three technologies is that they all utilise an advanced laser fabrication technology, known as ultrafast laser inscription (ULI), in their development. Because of the central role that

ULI plays in the work presented in this thesis, I present here a brief overview of how ULI works and what its capabilities are.

1.4.1   The basic physics of ULI

To perform ULI, ultrashort (usually < a few ps) pulses of laser radiation are focused inside a dielectric material that is transparent to the laser wavelength. If the pulse energy, pulse duration and focusing optics are appropriately chosen, the pulse will propagate through the substrate unattenuated until it reaches the focus. At the focus, the peak intensity of the laser pulse can be sufficiently high that the material becomes absorbing due to a combination of tunnelling ionisation and multiphoton ionisation, Figure 11(a) and (b) respectively. This generates seed electrons which reside at the bottom of the conduction band which are free to absorb laser photons from the remainder of the pulse, Figure 11(c). Once a seed electron has gained sufficient energy it can impact ionise a second electron residing at the top of the valence band, a process known as avalanche ionisation that results in an exponential increase in the density of the free electron plasma [36], Figure 11(d).

As described in Figure 12, the energy contained in the free electron plasma transfers to the cold lattice through carrier-phonon scattering, which takes place on the ps-to-few-ps time scales, rapidly heating the lattice and inducing a range of thermal and structural phenomena such as shock waves and localised melting. These structural phenomena can result in a variety of permanent localised modifications to the properties of the substrate, examples of which include changes to the refractive index and / or chemical etch rate. The technology of ULI aims to use these manifestations of the laser-induced structural modifications to fabricate structures such as optical waveguides, micro-optics and a range of other useful components, as described in the following sections.
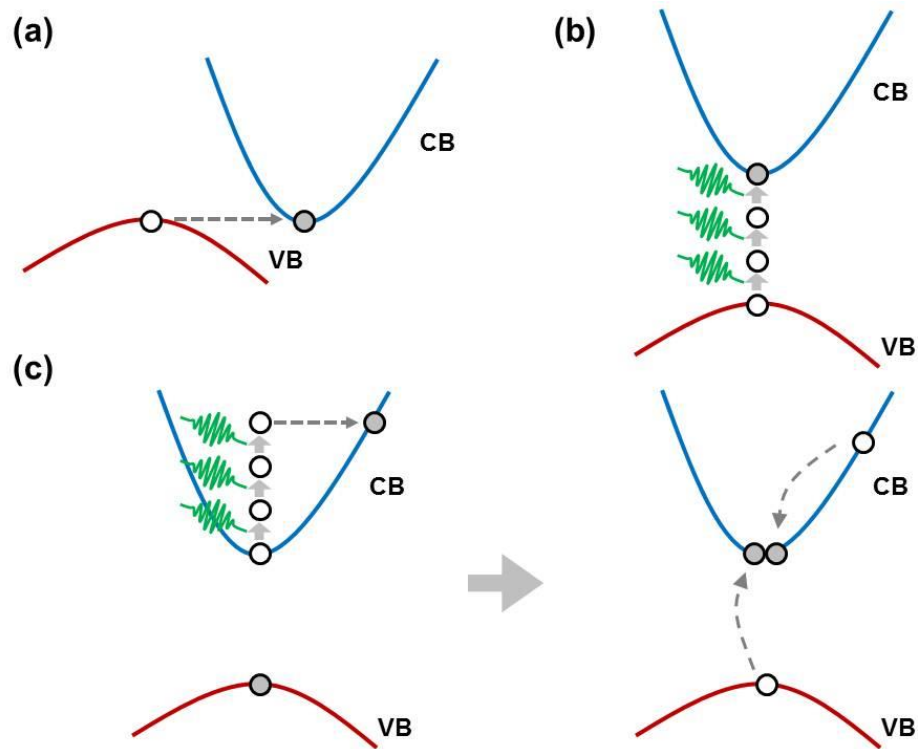
Figure 11: Conceptual representations of the nonlinear photoionisation processes that take place during ULI. (a) Tunnelling ionisation, where the electric field of the laser suppresses the Coulomb potential sufficiently such that a carrier can tunnel through the barrier. (b) Multiphoton ionisation, where multiple photons interact simultaneously to promote an electron from the valence band to the conduction band. (c) Avalanche ionisation, where excited carriers residing at the bottom of the conduction band absorb single photons one after the other until they have sufficient energy to impact ionise a carrier residing at the top of the valence band. Adapted from [36], © 2008 IEEE.
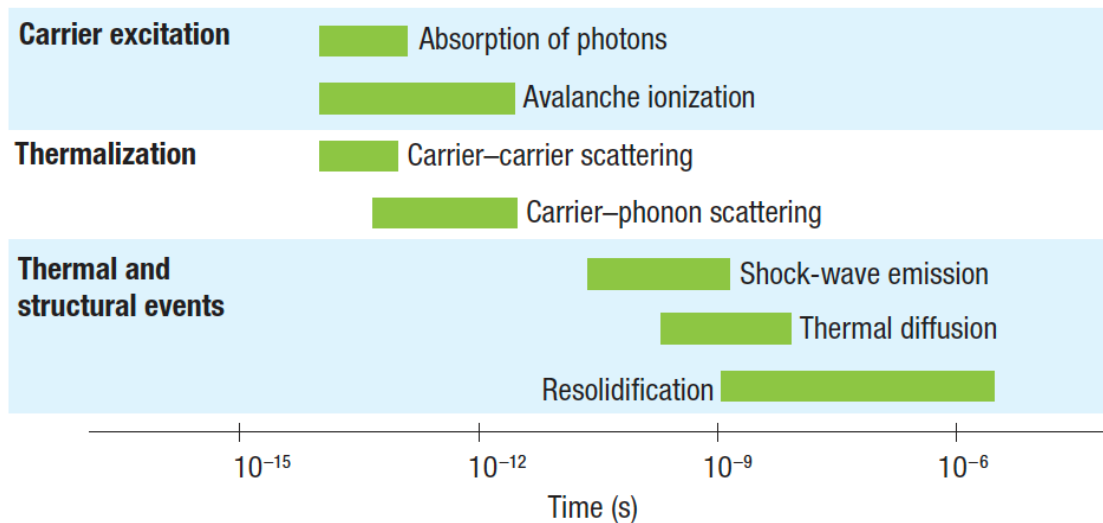
Figure 12: Schematic representation of the different energy transfer processes that take place during ultrafast laser inscription. Reprinted by permission from Springer Nature: Nature Photonics, Femtosecond laser micromachining in transparent materials, Rafael R. Gattass et al, © (2008)[37].

23

1.4.2 Controlling the ULI process

The properties of the modification created during the ULI process are dependent on the ULI parameters, the most important of these are:

- the substrate material.

- the focusing optics.

- the laser wavelength.

- the laser pulse repetition frequency.

- the laser polarisation.

- the laser pulse duration.

- the inscription geometry (is the substrate translated primarily along, or transverse, to the direction of the laser beam).

- the substrate translation speed and scanning trajectory.

This may seem like a vast parameter space, and that it would be impossible to efficiently find the optimal parameters. Fortunately, the parameter space becomes significantly smaller when one considers that:

- the eventual application usually determines the substrate material (there is no point developing a component for applications at visible wavelengths using a silicon substrate for example!).

- the laser wavelength is also determined by the substrate material, as the photon energy must be less than the material bandgap. In reality, the laser wavelength is usually determined by what laser systems the laboratory has available.

- the inscription geometry is usually set to be the "transverse writing geometry" where the substrate is primarily translated in the plane perpendicular to the propagation direction of the laser beam. This is because this geometry allows structures of effectively unrestricted paths to be fabricated, which is not the case when using the "longitudinal writing geometry".

Of the remaining parameters:

- the pulse energy is a crucially important parameter, as this controls the modification "regime". When using fused silica as a substrate material, for example, low pulse energies just above the modification threshold are found to induce a smoothly varying structural modification, higher pulse energies are found to induce a nano-structured modification which can exhibit properties such as birefringence, and even higher pulse energies can induce micro-explosions that leave a void structure [38].

- the pulse repetition frequency controls the inter-pulse time, and therefore the role of thermal accumulation [39]. If the pulse repetition rate is such that the inter-pulse time is much longer than the characteristic time for heat to diffuse out of the focal region (often about 1 μs), then each pulse is incident on material that is essentially cool. This reduces the efficiency with which the laser heats the material in the focal region, which can be detrimental for processes such as ultrafast laser welding, but useful for processes such as the ULI of optical waveguides as it results in more controllable and repeatable material modification.

- the focusing optics determine the spatial distribution of the electric field in and around the focal region. As a result, the focusing optics can be used to control the spatial distribution of the laser induced free electron plasma, and the spatial properties of the laser induced modification. For writing waveguides in silica, for example, we generally use a focusing lens with a numerical aperture of between ~0.6 and 0.3. Given that the laser wavelength is ~1.0 μm, this results in a beam waist diameter $\left(2\omega_0 = \frac{\lambda}{\pi\,NA}\right)$ of between ~1.0 μm and ~2.0 μm respectively, and a confocal parameter $\left(b = \frac{2\pi\omega_0^2 n}{\lambda}\right)$ of between 2.5 μm and 10 μm respectively. This will clearly result in a structural modification that has a high degree of asymmetry, unless steps are taken. These approaches can include the use of static [40] and active optic systems [41] to further control the shape of the laser focus or, as we have used in the work in this thesis for waveguide shaping, the use of substrate scanning strategies to control the final shape of the laser modified region – a technique known as the multiscan technique [42].

- the substrate translation velocity essentially controls the "amount" of modification without altering the other parameters such as the ULI regime. This is not strictly true, of course, because if the substrate translation velocity were set sufficiently high, then the pulses could be sufficiently separated spatially that they would arrive on cool material

regardless of the pulse repetition frequency, but this is an extreme situation and the assumption that the substrate translation velocity essentially controls the amount of modification is a good working one.

- the pulse duration plays an important role, but the reasons for this are not yet clear. At one end, it has been observed that longer pulses can be useful to reduce nonlinear effects that prevent the tight focusing of the pulse inside highly nonlinear materials such as $LiNbO_3$ [43]. At the other end, it has been observed that short pulses are required to write smooth structural modifications into fused silica [36]. In short, the pulse duration is a parameter that should be tuned to find an optimum, but the reason for this optimum may never be fully understood.

- the polarisation also plays an important role, but again the reasons are not well understood. When writing waveguides in some glasses, the use of circular polarisation has been associated with a larger increase in the refractive index change [44], and when using ULI to create structures for selective chemical etching, the polarisation can have a large impact on the selectivity of the etching, a fact that is thought to be due to the alignment of nano-grating structures with respect to the direction of propagation of the etchant [45].

The task of finding the optimum ULI parameters for a given application is an iterative one with the starting parameters informed by previous work. In the case of waveguides, for example, the process usually starts by fabricating structures with a wide range of pulse energies, polarisations, substrate translation velocities and path trajectories, and pulse repetition frequencies. The sample is then polished and analysed to investigate the guiding properties of the structures. Based on this analysis, a second sample is then fabricated with a narrower, but more finely interrogated, parameter space. This sample is then analysed, and so on.

1.5 Applications of ULI

The laser induced material modification can manifest itself in a variety of ways, examples of which include changes to the refractive index and/or chemical etch rate. The former of these can be used to directly write structures including volume gratings [46] and arbitrary phase patterns [47]. It is, however, the ability of ULI to fabricate

optical waveguides that has attracted the most attention over the past two decades, as it enables the fabrication of three-dimensional optical waveguides in passive and active glasses and crystals. The fact that ULI can also be used to locally increase the chemical etch rate of certain dielectrics also opens up a range of powerful applications. In this section, I review just a few of the applications that are being pursued for ULI.

1.5.1   Passive waveguide devices

The fact that ULI can be used to fabricate three-dimensional optical waveguide structures in dielectrics opens the door to a range of powerful capabilities in terms of realising new light reformatting and mode manipulation devices. ULI can be used, for example, to realise components such as three-dimensional optical splitters [48] as shown schematically in Figure 13. This capability can also be extended to the realisation of three-dimensional optical reformatting components for interconnecting applications, and the use of ULI fabricated fan-outs for coupling to-and-from MCFs has now even been commercialised e.g. the fan-outs used in the "Hero" experiment [49] were supplied by Optoscribe Ltd.
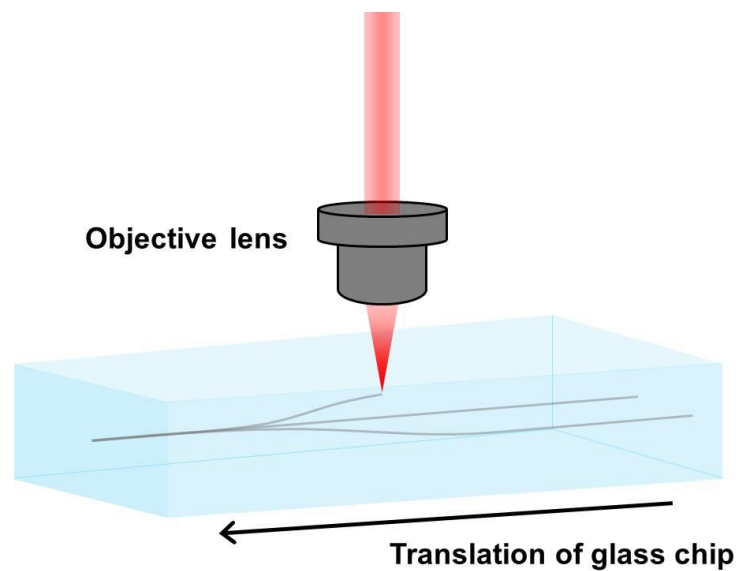
Figure 13: Conceptual cartoon of how ULI can be used to fabricate a three-dimensional integrated waveguide splitter. Adapted with permission from Springer Nature: Applied Physics A: Materials Science & Processing (Femtosecond waveguide writing: a new avenue to three-dimensional integrated optics, S. Nolte et al), © (2003)[48].

Integrated optical waveguide splitters and reformatters are not the only passive capabilities enabled by ULI. The fact that ULI can enable the precise shaping of the waveguide cross section in three-dimensions opens up new opportunities in mode manipulation. A particular example of this capability is the application of ULI to the fabrication of three-dimensional integrated photonic lanterns [26, 50] that can efficiently couple multimode light to single mode waveguides and vice-versa. Such devices can even be integrated with ULI fabricated Bragg-gratings, and such components could find future applications in astronomy for OH-line suppression [51].
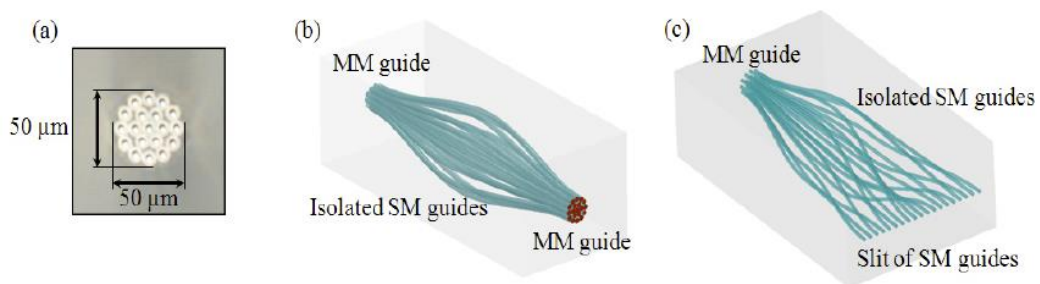
Figure 14: (a) Micrograph of the multimode end of a ULI fabricated photonic lantern. (b) Cartoon showing how 3D ULI fabricated photonic lantern transitions can be used to create a multimode-to-singlemode-to-multimode device. (c) Cartoon showing how 3D ULI fabricated photonic lantern transitions can be used to create a multimode-to-diffraction-limited-pseudo-slit device. Reprinted with permission from [50] © The Optical Society.

1.5.2   Active waveguide devices

The fact that ULI can be used to fabricate optical waveguides in nearly any transparent dielectric material opens up the possibility of realising active devices such as lasers and modulators. Indeed, ULI has been successfully used to fabricate high gain (~16 dB) waveguide amplifiers operating at around 1550 nm in the telecommunications C-band by inscribing optical waveguides in Er-doped bismuthate glass [52]. Taking this concept further, there has been a huge amount of work in the community into developing compact integrated waveguide lasers using ULI, and there have been successful demonstrations across multiple spectral regions, including the visible at around 636 nm using praseodymium-doped fluorozirconate glass [53], the near-infrared at around 1030 nm using Yb:YAG [54], the near-infrared at around 1550 nm using ErYb-doped glass [55], and even the mid-IR at around 1.91 μm using Tm-doped glasses [56] and 2,486 nm using Cr:ZnSe [57].

Waveguide amplifiers and lasers are not the only active devices that can be realised using ULI. By fabricating waveguides in crystalline materials it is also possible to realise frequency conversion devices based on quasi- [58] and birefringent phase matching techniques [59], and it is even possible to fabricate quasi-phase-matched structures by using the femtosecond laser to periodically structure the $\chi^{(2)}$ [60].

1.5.3 Selectively etched devices

The fact that ULI can be used to locally increase the chemical etch rate of a variety of materials opens the door to realising previously impossible structures. This capability has been extensively used to fabricate micro-optic structures such as mirrors based on total internal reflection [61] and lenses [62], and even hollow optical waveguides for future applications in high field physics [63]. One application for the selective etching capability enabled by ULI that has attracted particular attention is the development of microfluidic structures, and devices have been developed for many microfluidic applications, examples of which include the sorting of cells based on the mechanical properties of the cells [64] and studies of fluid mechanics at the micron scale [65].

The fact that ULI can be used to fabricate three-dimensional microfluidic structures is certainly powerful, but it is the fact that ULI can be used to fabricate such structures and integrate them passively with other structures that is particularly powerful. This capability has been used successfully to create a variety of "optofluidic" structures that combine optical and microfluidic capabilities. Particularly impressive examples include the development of integrated optofluidic devices for selective plane illumination microscopy (SPIM) [66], as shown in Figure 15, and the development of optofluidic devices that integrate microfluidics and optical waveguides for interrogating cells through "optical cell stretching" [67], as shown in Figure 16.
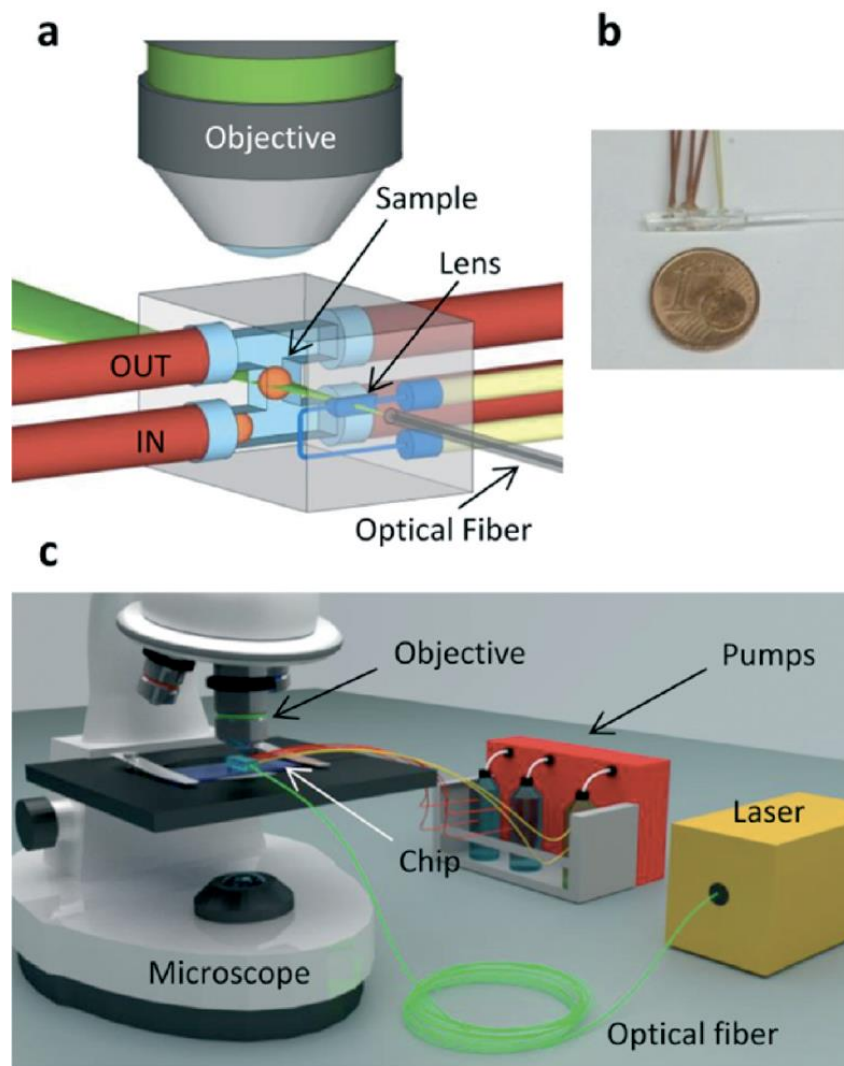
Figure 15: (a) Schematic of the SPIM-on-a-chip device developed by Paiè et al, where ULI is used to create a network of three-dimensional microfluidic structures. One set of structures can be used to create a fluidic cylindrical lens, the focusing power of which can be tuned via the refractive index of the fluid. The other set of structures could be used to control the flow of biological organoids past the light-sheet focus of the cylindrical lens. (b) Photograph of the device next to a 1 Euro coin. (c) Cartoon showing how the device would be used in conjunction with a microscope to perform the SPIM imaging. Reproduced from [66] with permission from the Royal Society of Chemistry.
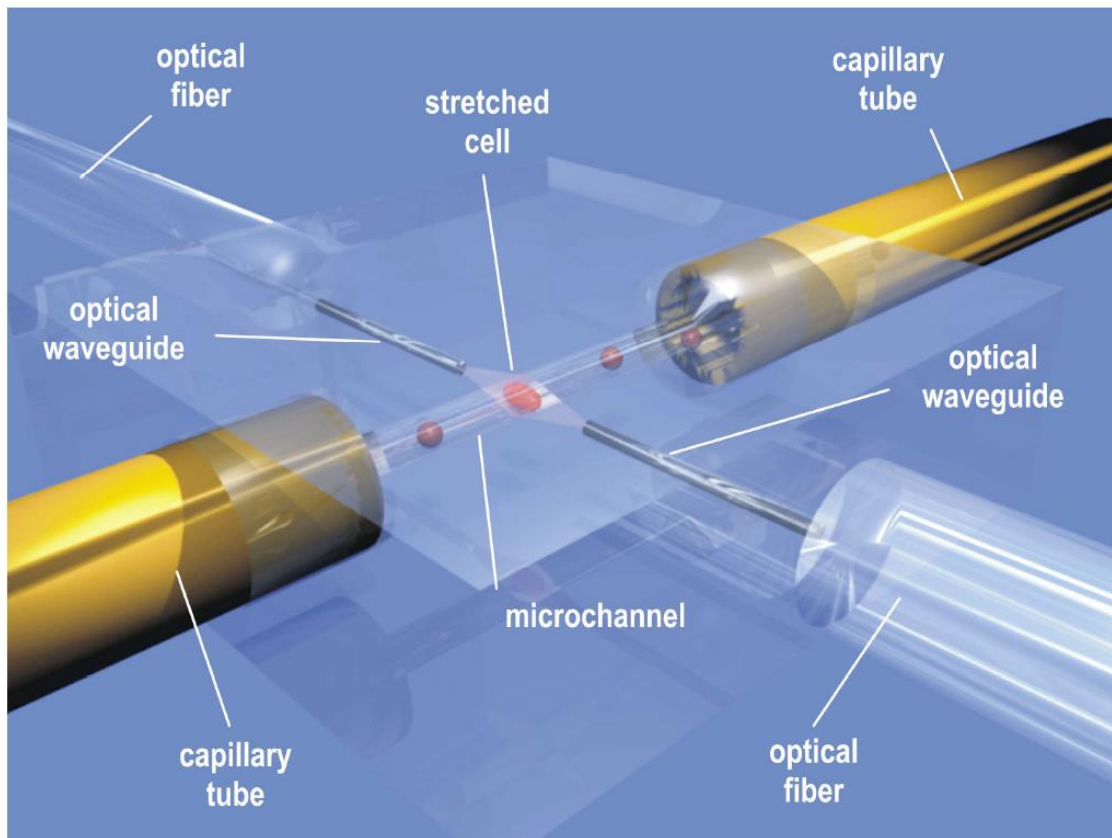
Figure 16: Cartoon of an optofluidic cell stretching devices fabricated via ULI. The device consists of a microfluidic channel which is fabricated using ULI-induced selective etching, together with two ULI-fabricated waveguides that interrogate the microfluidic. As cells pass the optical waveguides, they are first trapped by the counter propagating laser beams, and then stretched once the power of the laser beams is increased sufficiently. Reprinted with permission from [67] © The Optical Society.

1.5.4 Applications of ULI not discussed

The breadth of applications now being pursued for ULI is too vast to discuss all of them in this thesis, and I have chosen to focus on some of the more applied areas, rather than the areas of fundamental interest. It is worth highlighting, however, that ULI is also becoming an enabling technology in many other areas not covered here, including quantum photonics [68] and optical analogues of physical phenomena, including topological physics [69] and condensed matter physics [70]. It can also be used to fabricate structures in optical fibres, including waveguides written into the cladding of the fibre [71] and FBGs [72].

1.6 Conclusion

In this Chapter, I have set the context for the research presented in this thesis. I have provided an introduction to the various types of astronomy that exist, and the role that the astronomical instruments play in astronomy. I have presented the case for astrophotonics, and discussed some of the astrophotonic applications that are currently being pursued by research groups around the world. In the following chapters, I present my work on developing ULI fabricated astrophotonic devices, and so given the importance of ULI to my research I have also provided the reader with a brief introduction to the technology of ULI, covering how it works, how it can be controlled, and some of the various applications for this emerging fabrication technology.

Chapter 2 - Modal noise mitigation for high-precision spectroscopy using a photonic reformatter

2.1 Introduction

The precision with which a spectrograph can measure changes in the spectrum of an optical signal is dependent on many parameters, one of which is its stability. The stability of a spectrograph is in turn determined by factors, including its susceptibility to thermal fluctuations, mechanical vibrations and changes in gravitational loading on the instrument as the telescope slews (if the instrument is attached to the telescope itself), all of which can affect the manner in which light is dispersed and detected.

Applications such as radial velocity measurements require the acquisition of spectral signatures with the highest possible precision. To facilitate this, almost all state-of-the-art radial velocity spectrographs are completely mechanically decoupled from the telescope, and placed in an environmentally stabilised room in the observatory. Light from the telescope is then collected from the telescope focal plane using a multimode optical fibre, which can flex and change shape as the telescope slews to track the object, and transported to a spectrograph for analysis.

Unfortunately, the use of multimode optical fibres for high precision astronomical spectroscopy can result in a phenomenon known as "modal noise", where the distribution of light at the spectrograph end of the multimode fibre is not stable. This optical instability effectively results in a variation in the spectrograph lineshape over time, limiting the precision with which variations in the spectral properties of astronomical signal can be identified.

In the published paper which accompanies this chapter, I demonstrate how a "hybrid" photonic optical reformatting device, which is constructed by combining a multicore fibre photonic lantern with an ultrafast laser inscribed 3D waveguide reformatter, can be used to strongly mitigate modal noise in multimode spectrographs.

2.2 Motivation

2.2.1 *What is modal noise in fibre-fed astronomical spectrographs?*

As discussed briefly in Chapter 1, the efficiency with which starlight from a telescope can be coupled into an optical fibre is limited by the mismatch between the number of spatial modes supported by the optical fibre and the number of modes that form the stellar image. Under either perfect seeing conditions, or diffraction limited operation using an extreme AO system, the unresolved stellar image, which is essentially just the telescope PSF, will be close to an Airy function, or even a Gaussian-like distribution if pupil apodization is used. Such optical profiles can, in principle, be efficiently coupled to single mode fibre [23]. If, however, the seeing conditions are not perfect, or no extreme AO system is available, the telescope PSF will be multimode, with the number of modes forming the PSF (M_{PSF}) being given by Equation 6 and Equation 7 [29]:

$$M_{PSF} \approx \left(\frac{\pi \, \theta_{Focus} D_T}{4\lambda} \right)^2$$

<div align="right">Equation 6</div>

Where D_T is the diameter of the telescope, λ is the wavelength of the light, and θ_{Focus} is the astronomical seeing, given by:

$$\theta_{Focus} \approx \sqrt{(\lambda/D_T)^2 + \theta_{Seeing}(\lambda)^2}$$

<div align="right">Equation 7</div>

Again, as discussed in Chapter 1, to put this into context, the 3.58 m Telescopio Nazionale Galileo (TNG) commonly experiences seeing conditions of 0.6 arcsec seeing. This means that its PSF would consist of $\sim$75 modes at 950 nm and $\sim$12 modes at 2,500 nm. To efficiently collect this light from the telescope focal plane it is therefore necessary to use multimode optical fibres, and the efficiency of the injection can be expected to be limited to $\sim \frac{M_{Device}}{M_{PSF}}$, up to a maximum of 1.

Unfortunately, the use of multimode optical fibres in astronomical spectroscopy can result in issues with "modal noise". Modal noise is a phenomenon that occurs in multimode fibre spectrographs due to the coherent nature of the telescope PSF, which in turn excites a coherent set of spatial modes at the telescope-end of the multimode optical fibre, with well-defined relative phase and power relationships. These modes then travel down the fibre, resulting in pattern of light at the spectrograph end of the fibre. As the telescope slews, and as the seeing conditions change, the shape and position of the stellar image on the input to the fibre can change, changing the relative phases and amplitudes of the fibre modes that it excites. Movements in the fibre further impact the relative phases and amplitudes of the spatial modes at the spectrograph end of the fibre. The combination of all of these processes means that the pattern of light at the spectrograph end is unstable, as shown in Figure 17, resulting in a source of noise in the acquired spectrum called modal noise.
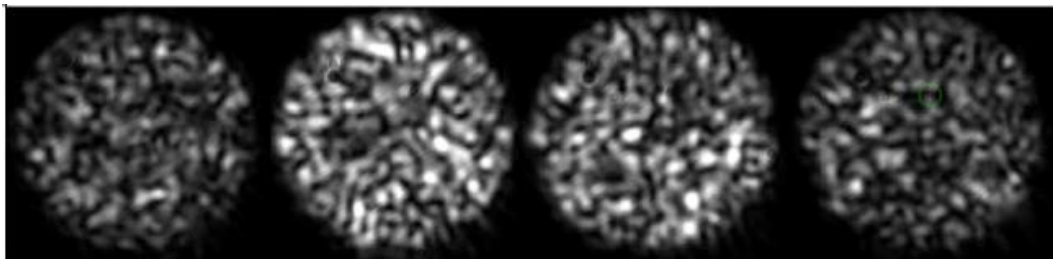
Figure 17: Examples of how the pattern of light at the output of a multimode optical fibre changes as the input coupling is varied. Taken and adapted from [73].

Because the pattern of light at the end of a long length of multimode optical fibre changes rapidly with wavelength, the phenomena of modal noise only becomes an issue in high resolution, high precision spectrographs, such as those intended for applications in RV measurements. In contrast, in lower resolution spectrographs, the modal noise averages out over the spectrograph resolution bandwidth. Another interesting, and somewhat unintuitive, property of modal noise is that once multimode fibres are used, its magnitude actually reduces as the number of modes involved increases due to statistical averaging. For this reason, modal noise is not particularly problematic in fibre-fed RV spectrographs such as HARPS [2], which operates in the visible region of the spectrum, from 380 nm to 690 nm with a resolution (R) of around 115,000, and can provide RV measurements of stars with sub m.s^{-1} precision. In contrast, modal noise is

extremely problematic at near-infrared wavelengths. In GIANO, a high resolution (R ≃ 50,000) infrared (950–2450 nm) spectrometer constructed for the TNG, modal noise was found to severely limit the precision with which spectra could be acquired, and that no amount of fibre agitation could mitigate it completely [74], as shown in Figure 18.
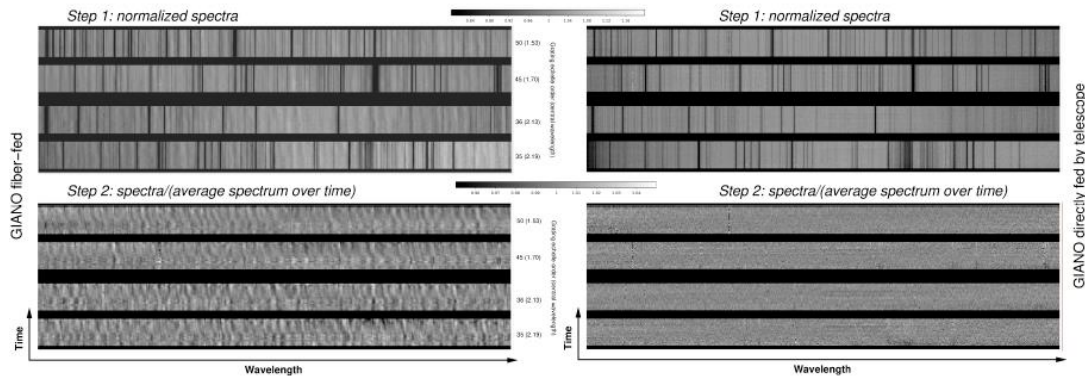

Figure 18: Time-series spectra of stars collected with the GIANO spectrometer. Left- and right-hand panels: data collected with and without fiber feeding, respectively. Modal noise causes the wavy pattern clearly visible in the data taken with fibres. Credit: E. Oliva et al., A&A 632, A21, 2019, reproduced with permission © ESO [74].

2.3 Techniques for mitigating modal noise

2.3.1 *Traditional approaches to mitigating modal noise*

The most obvious approach to mitigate modal noise is to feed the spectrograph with a single mode optical fibre, rather than a multimode fibre. As mentioned previously, this approach will come with an unacceptable reduction in coupling efficiency between the telescope, unless the telescope is operating close to the diffraction limit. It should be noted that a number of groups are pursuing this approach by using extreme adaptive optics systems such as the SCExAO instrument at the Subaru Telescope [75], or iLocator at the Large Binocular Telescope [76]. Unfortunately, extreme AO systems are expensive and have a limited field of view, and as such currently only operate well with bright objects. For these reasons, alternative approaches are required that can mitigate modal noise in conventional multimode fibre fed spectrographs.

The aim of any system intended to mitigate modal noise is to somehow "force" the time-averaged light pattern at the spectrograph end of the multimode fibre to be as stable as possible between measurement exposures, regardless of how the fibre is excited, and how the fibre is moved. Given that variations in the pattern of light at the

output of the fibre arise because alterations to the fibre position and fibre excitation affect the relative amplitudes and phases of the fibre modes at the output of the fibre, it is clear that techniques to mitigate modal noise should seek to equalise, when considered in a time-averaged manner across the measurement, the distribution of light at the output of the multimode fibre across the spatial modes, and randomise, when considered in a time-averaged manner across the measurement, the relative phases of the spatial modes.

Established techniques to mitigate modal noise include the use of "rotating double scramblers" [77] and diffusers and integrating spheres [78], but the simplest and most widely used technique to "thermalise" the light at the output of the fibre is simply to shake the optical fibre. This promotes mode coupling and randomises the relative phases of the spatial modes. Many ingenious techniques have been pursued to shake multimode fibres to mitigate modal noise in high resolution astronomical spectroscopy, including speakers and fans, and the results can be extremely good for high mode count systems. As an example, Figure 19 shows the patterns of light at the output of three multimode fibres when the fibre is either static or agitated. The absence of speckles in the images obtained when the fibre is agitated demonstrates the suppression of modal noise.
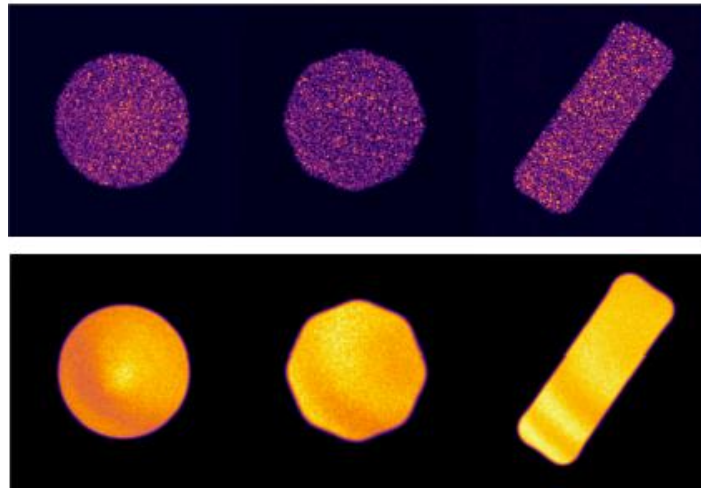
Figure 19: (Top) Speckle patterns at the output of 200 μm circular (left), 200 μm octagonal (middle), and 100 μm × 300 μm rectangular (right) optical fibres that are excited at 652 nm using a single mode optical fibre. All fibres have an NA of 0.22. (Bottom) The same fibres shown above, but the fibres are agitated using a custom "shaker", and the exposure is controlled such that it is significantly longer than the timescale of the agitation. Taken and adapted from [79]. © AAS. Reproduced with permission.

2.3.2 *Astrophotonic techniques for mitigating modal noise*

In the previous section I discussed some of the traditional approaches to mitigating modal noise in traditional multimode fibre fed spectrographs, but astrophotonic technologies are now opening up new possibilities. In 2012, Birks et al [27] demonstrated that a multimode-to-single-mode-to-multimode fibre device realised using a 121-core multicore fibre with photonic lantern transitions at each end could act as an extremely efficient mode scrambler, Figure 20. This concept was later extended to a 511 core fibre, and shown to perform better than an octagonal fibre which is commonly used in astronomy for its mode scrambling properties [33].
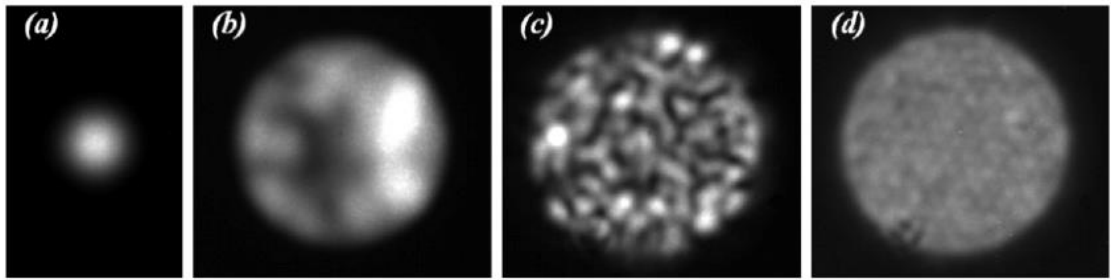
Figure 20: Near field images of the light emitted from (a) a single mode fibre, (b) a multimode fibre, (c) the multimode output of a MM-to-SM-to-MM fibre devices created using a 121 core MCF lantern, and (d) the output of the same device used in (c) but with fibre agitation and a long exposure to average out the speckles. Reprinted with permission from [80] © The Optical Society.

Photonic lanterns also open up another route to mitigate modal noise by efficiently converting the multimode light into a series of single modes, each of which can be dispersed in a modal noise free manner [81, 82]. This approach can be conducted using photonic lanterns constructed using multicore fibres, but the number of modes this can be applied to is limited because the spectra from multiple cores will begin to spatially overlap on the detector. Another approach which can be extended to higher numbers of modes is to feed the light into the spectrograph via a photonic lantern created from a tapered bundle of single mode fibres, as shown schematically in Figure 21. In this case, the light can be reformatted to create a one-dimensional pseudo-slit, which should allow the spectrograph to operate at the diffraction limit, and in a manner that is free of modal noise. This approach has become known as the photonic integrated multimode microspectrograph (PIMMS) approach.
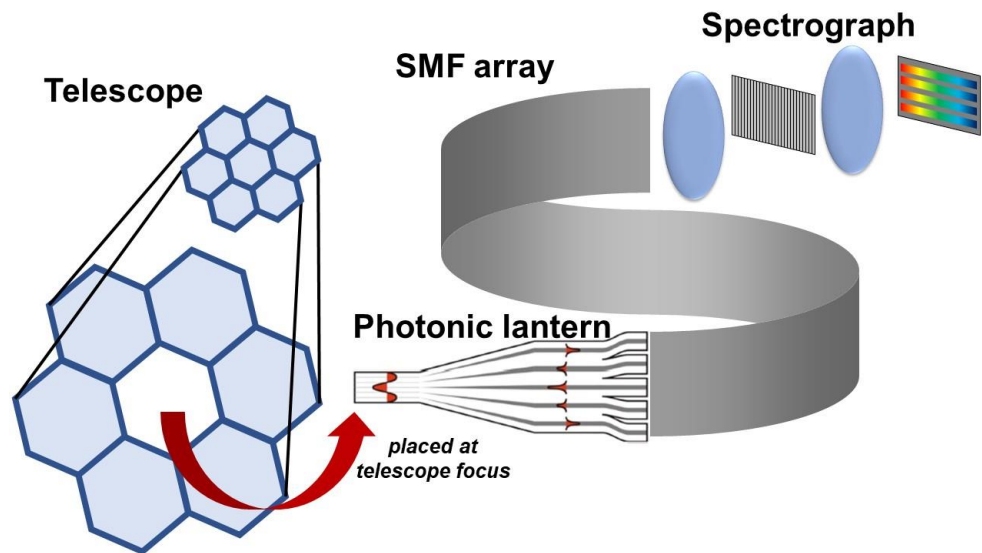
Figure 21: Schematic diagram of a photonic integrated multimode micro-spectrograph (PIMMS) system formed by feeding multimode light into a diffraction limited spectrograph via a photonic lantern. Adapted and reprinted with permission from [81] © The Optical Society.

2.4 Aim of the study

One disadvantage of the PIMMS approach using photonic lanterns created from a tapered bundle of single mode fibres is that the presence of the cladding material in the fibres limits the minimum distance between the fibres that form the pseudo-slit. This means that each spectrum from each fibre is separated by a significant distance in the axis orthogonal to the dispersion axis, limiting the use of the detector real-estate, and resulting in a longer pseudo-slit length than is otherwise necessary. To address this issue, MacLachlan et al [83] developed a new astrophotonic reformatting technology based on a multicore fibre photonic lantern combined an ultrafast laser inscribed 3D waveguide reformatter. The photonic lantern converts the modes at the multimode end of the photonic lantern into a two dimensional array of single modes, while the 3D waveguide reformatting components reformats the single modes exiting the photonic lantern into a one-dimensional diffraction limited pseudo-slit. Crucially, in this technology, there is no space between the single mode waveguides that are brought together to form the output of the component. Figure 22 presents a schematic of the device together with photographs of the actual device developed by MacLachlan et al, and its sub-components. In the paper that accompanies this chapter, I demonstrate that that this hybrid device can indeed efficiently suppress modal noise in near-infrared spectrographs that operate at the diffraction-limit, and discuss how such components could be used for applications including radial velocity measurements of M-dwarfs.
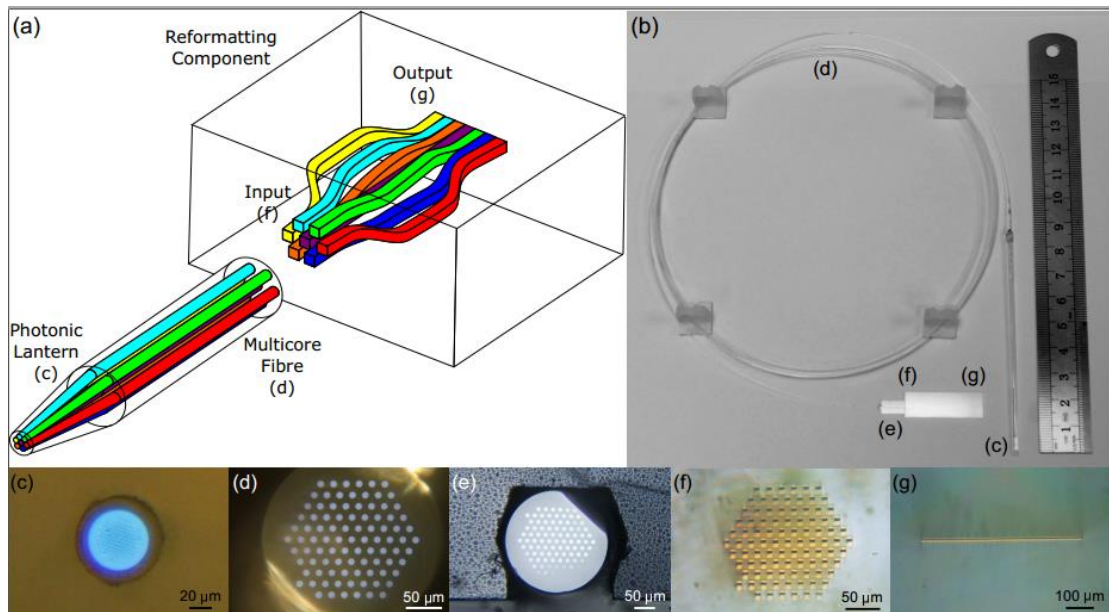
Figure 22: (a) Schematic diagram of the "hybrid photonic reformatter" which utilises a multicore fibre photonic lantern in combination with an ultrafast laser inscribed 3D waveguide reformatting component to transform multimode light into a diffraction limited pseudo-slit. (b) Photograph of the hybrid reformatter device. (c) Photonic lantern with multimode input port. (d) Facet of the multicore fibre. (e) Multicore fibre placed in a custom ULI fabricated V-groove. (f) Input facet of the ultrafast laser inscribed 3D waveguide reformatting component. (g) Pseudo-slit output of the reformatting component.

2.5 My contributions

This section explains what contributions were made by myself and my co-authors towards the work in the following paper. The photonic lantern was made by I. Gris-Sánchez, and the reformatter was designed, manufactured and connected by D. G. MacLachlan and R. J. Harris. I characterised the source and fibres, constructed the spectrograph with the design advice of D. Lee and R. R. Thomson (RRT), and aligned it with each of the 3 devices which were tested. Data was collected from the spectrograph by myself, with assistance from A. Benoît (AB), who also helped determine the most rigorous and useful methods of analysis. I analysed the data to determine the precision of the spectrograph and created the figures. A calibration for correcting the slanted slit was developed by myself and RRT, who also ensured the validity of the "temperature proxy" analysis method. I wrote the paper with assistance from AB, T. A. Birks, and RRT.

Modal noise mitigation for high-precision spectroscopy using a photonic reformatter

F. A. Pike [ID],[1][*] A. Benoît [ID],[1] D. G. MacLachlan,[1] R. J. Harris [ID],[2] I. Gris-Sánchez [ID],[3][†] D. Lee,[4] T. A. Birks[3] and R. R. Thomson[1]

[1]*SUPA, Institute of Photonics and Quantum Sciences, Heriot-Watt University, Edinburgh EH14 4AS, UK*
[2]*Zentrum für Astronomie der Universität Heidelberg, Landessternwarte, Königstuhl 12, D-69117 Heidelberg, Germany*
[3]*Centre for Photonics and Photonic Materials, Department of Physics, University of Bath, Bath BA2 7AY, UK*
[4]*STFC UK Astronomy Technology Centre, Royal Observatory, Blackford Hill, Edinburgh EH9 3HJ, UK*

ABSTRACT

Recently, we demonstrated how an astrophotonic light reformatting device, based on a multicore fibre photonic lantern and a 3D waveguide component, can be used to efficiently reformat the point spread function of a telescope to a diffraction-limited pseudo-slit. Here, we demonstrate how such a device can also efficiently mitigate modal noise – a potential source of instability in high-resolution multimode fibre-fed spectrographs. To investigate the modal noise performance of the photonic reformatter, we have used it to feed light into a bench-top near-infrared spectrograph ($R \approx 7000$, $\lambda \approx 1550$ nm). One approach to quantifying the modal noise involved the use of broad-band excitation light and a statistical analysis of how the overall measured spectrum was affected by variations in the input coupling conditions. This approach indicated that the photonic reformatter could reduce modal noise by a factor of 6 when compared to a multimode fibre with a similar number of guided modes. Another approach to quantifying the modal noise involved the use of multiple spectrally narrow lines, and an analysis of how the measured barycentres of these lines were affected by variations in the input coupling. Using this approach, the photonic reformatter was observed to suppress modal noise to the level necessary to obtain spectra with stability close to that observed when using a single mode fibre feed. These results demonstrate the potential of using photonic reformatters to enable efficient multimode spectrographs that operate at the diffraction-limit and are free of modal noise, with potential applications including radial velocity measurements of M-dwarfs.

Key words: instrumentation: spectrographs – techniques: radial velocities – planets and satellites: detection.

1 INTRODUCTION

Since the first discovery of a planet orbiting a main-sequence star in 1995 (Mayor & Queloz 1995), the search for exoplanets has been a major focus of modern astronomy. Current technology can only directly image very long-period planets using the very largest telescopes therefore detection techniques require us to look at the effect the planet has on its host star. The two most successful techniques are transit photometry (Borucki & Summers 1984), where the variation in the brightness of a star as the planet transits across it is measured, and the radial velocity (RV) method (Reiners et al. 2010), which involves measuring the Doppler shift in the host star's spectrum due to the motion around the system barycentre. When these methods are used in combination, a great deal of information can be gathered about the exoplanet in question, including the density (Charbonneau et al. 2000). Typically, an exoplanet candidate is identified using a survey telescope, which relies on transit photometry. A famous example of such a telescope is the recently retired *Kepler Space Telescope*, which has allowed the identification of more than half of all confirmed exoplanets. Among others, the recently launched *TESS* will observe the entire sky during its mission, and the PLATO mission is due for launch in 2026. They are expected to provide many new targets in the coming years. *Kepler* was designed specifically for the detection of the Earth–Sun system analogues (Koch et al. 2010), and upon analysing the data, the prevalence of terrestrial planets detected was highly encouraging, although a poor detection rate of smaller radius planets was identified (Catanzarite & Shao 2011). Following this discovery, Dressing & Charbonneau (2013) extended the *Kepler* data to smaller planets around smaller stars, and estimated that M-dwarfs hosted habitable near-Earth-sized planets at a rate of $0.15^{+0.13}_{-0.06}$ per star.

M-dwarfs are small cool stars (~ 2500 K) with peak blackbody emission in the near-infrared (NIR) range, and may have an anomalously high chance of hosting exoplanets. According to the study by Mulders, Pascucci & Apai (2015), there is an inverse correlation between stellar temperature and planet occurrence rates: planets around M stars occur twice as frequently as around G stars (such as

---

[*] E-mail: fap30@hw.ac.uk
[†] Currently with ITEAM Research Institute, Universitat Politècnica de València, Camino de Vera s/n, 46022 Valencia, Spain (IG-S).

the Sun). Indeed, an M-dwarf hosts one of the largest Solar systems discovered to date (apart from our own) – TRAPPIST-1 (Gillon et al. 2017). The closest exoplanet to the Earth, Proxima Centauri b, also has an orbit in the habitable zone of an M-dwarf (Anglada-Escudé et al. 2016). A further advantage of performing RV measurements of these cooler, lower mass stars is the increased perturbations from habitable zone planets − the habitable zone being closer and the smaller mass disparity allows much easier detection of small rocky planets that could host life (Claudi et al. 2017).

To date, the most successful RV spectrograph is High Accuracy Radial velocity Planet Searcher (HARPS), which operates over visible wavelengths between 380 and 690 nm, with a resolving power of 115 000, and uses a multimode (MM) fibre to feed light from the telescope focal plane to the instrument, which is placed in the observatory basement where environmental conditions are strictly controlled for maximum stability (Mayor et al. 2003). Such advantages of feeding spectrographs with optical fibres are profound and well-known (Angel et al. 1977; Barden 1994). HARPS also uses a simultaneous ultrastable ThAr reference spectrum fed through an adjacent fibre, to allow an RV precision down to 30 cm s^{-1} (Fischer et al. 2016). Unfortunately, the use of silicon-based charged-coupled-device arrays in HARPS restricts its observations to visible wavelengths, preventing efficient RV measurements of M-dwarf stars whose blackbody emission peaks in the NIR. There is therefore a strong pull to develop high-precision ($\sim$1 m s^{-1}) spectrographs for NIR RV measurements, but this capability still remains to be addressed. To highlight the difference in precision between wavelengths, CARMENES, which saw first light in 2015, exhibits a precision of 1–2 m s^{-1} in the visible, and 5–10 m s^{-1} in the NIR (Quirrenbach et al. 2018). Roy et al. (2016) also state this discrepancy in precision goals, these being $\sim$10 cm s^{-1} in the visible and <1 m s^{-1} in the NIR. One example of a visible spectrograph with a precision goal of 10 cm s^{-1} is ESPRESSO (Pepe et al. 2010), and an example of an NIR spectrograph with a precision goal of 1 m s^{-1} is NIRPS (Blind, Conod & Wildi 2017).

The use of fibres for transporting light from the telescope focal plane to the instrument is highly advantageous for environmental stability reasons, but they are not without drawbacks. For example, modal noise (Hill, Tremblay & Kawasaki 1980; Rawson, Goodman & Norton 1980) is a phenomenon that occurs where the pattern of light at the output of the fibre evolves with time, due to fluctuations in the distribution of optical energy or relative phases of the guided modes. Modal noise will arise when the stellar image at the fibre input changes (either a change in its position as the telescope slews, or from changing atmospheric conditions), or if the fibre bends (due to the telescope slewing, thermal variations, or air currents). This drastically reduces the signal to noise (Baudrand & Walker 2001) and severely limits the accuracy of the spectrograph. A further issue with the modal noise is that it cannot be eliminated by calibration, since the injection of the calibration source will never exactly match that of the star and thus the different coupling exacerbates the modal noise.

Modal noise is obviously minimized using a single mode (SM) fibre to feed the spectrograph, but at the expense of telescope–fibre coupling efficiency, since atmospheric turbulence causes wavefront distortions and produces a stellar image that is not diffraction-limited. Extreme adaptive optics (AO) can be used to increase the coupling efficiency, and is planned for several future instruments (Crepp et al. 2016). However, this is expensive, and only possible where a suitably bright natural guide star is available, limiting the number of targets (Morris, Corrigan & Harris 2016). In any case, the point spread function (PSF) will still not be completely diffraction-limited

(Jovanovic et al. 2016). Once in the MM regime, modal noise actually reduces as the number of spatial modes increases due to statistical averaging. The number of modes (in a step index fibre), N_{modes}, is strongly dependent on the wavelength, λ, of a given fibre. This can be seen in equation (1):

$$N_{\mathrm{modes}} = \left(\frac{\pi \cdot a \cdot NA}{\lambda} \right)^2, \qquad (1)$$

where a and NA are the fibre core radius and numerical aperture (defined by the effective core and cladding refractive indices), respectively.

The simplest approach to mitigate modal noise in MM fibre-fed spectrographs is to agitate the fibre (Baudrand & Walker 2001), which cross-couples the excited modes and averages the energy over all modes, including some that were not initially populated. This is most effectively done by hand due to the random nature of the hand movement (Plavchan et al. 2013), although an auto-mated mechanical oscillator is more practical during observations. Other methods for mode-scrambling include using alternative fibre geometries, e.g. octagonal or rectangular core fibres (Petersburg et al. 2018). Annealed fibre has also shown effective mode-scrambling (Osterman et al. 2014) since scattering centres are produced in the fibre that distribute light uniformly both radially and azimuthally. Laser speckle reducers are also available commercially and have been used to some success by Mahadevan et al. (2014). In all of these cases, however, it is important to stress that efficient mode-scrambling becomes increasingly difficult to achieve as the number of modes decreases, making modal noise a particular challenge in precision MM fibre-fed NIR spectrographs. It is for this reason that modal noise is not a significant problem for spectrographs like HARPS that operate in the visible, but was a limiting factor in GIANO at the Telescopio Nazionale Galileo (Iuzzolino et al. 2014), which suffered from such significant modal noise that the engineers modified the entrance slit to bypass the fibre altogether (Oliva et al. 2015). This free-space approach does not take advantage of the environmental and optomechanical stability advantages offered by an optical fibre feed.

A potential alternative to standard modal-noise mitigation tech-niques relies on the exploitation of photonic lanterns (PLs; Leon-Saval et al. 2005; Birks et al. 2015), guided wave transitions that efficiently couple light from a MM port to an array of SM waveguides. PLs can be created in a variety of ways. For example, a multicore fibre (MCF) with a 2D array of SM cores can be heated and tapered to form an MM port when the taper is cleaved, with the taper forming a gradual transition between the MM port and the SM cores of the MCF. Such MCF–PLs are a well-suited method to eliminating modal noise in RV spectrographs (Gris-Sánchez et al. 2018; Haynes et al. 2018). A second approach involves the tapering of a bundle of SM optical fibres to form an MM port in a similar manner. Regardless of the specific fabrication approach used, a spectrograph fed with MM starlight in the form of multiple SMs should be free of modal noise. To exploit the full potential of this capability, however, it is essential to correctly arrange the SMs generated by the PL at the slit of the spectrograph, such that the individual spectra from each SM do not overlap on the detector. One approach to achieve this in MCF–PL-fed spectrographs is the TIGER method (Leon-Saval, Betters & Bland-Hawthorn 2012; Betters et al. 2020), where the MCF is rotated to the correct angle, although this technique is only applicable to systems operating in the few-mode regime. Another approach proposed by Bland-Hawthorn et al. (2010), known as the Photonic Integrated MultiMode Spectrograph (PIMMS) concept, would make the use of PLs fabricated from multiple SM fibres. In this case, the individual
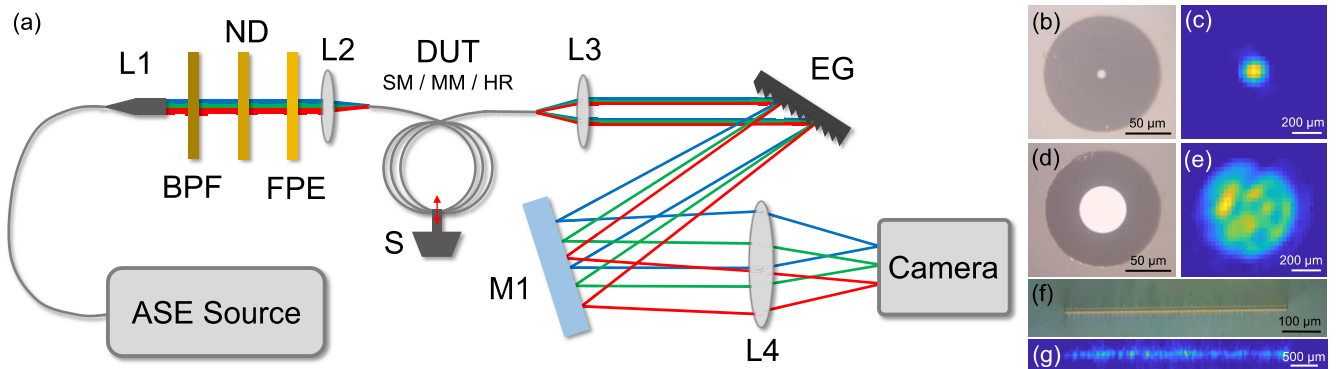
Figure 1. (a) Schematic of spectrograph layout including fibre-coupled ASE source, L1 fibre collimation package, BPF bandpass filter, ND filter, FPE Fabry-Pérot etalon (if required), L2 coupling into the device under test (DUT), mechanical shaking system S, collimation by L3, the dispersion by an Echelle grating (EG), folded by mirror M1 and focused by L4 on to an InGaAs Camera; (b) image of the 8.2 μm core SM fibre; (c) typical output light pattern of the SM fibre; (d) image of the 50 μm core MM fibre; (e) typical output light pattern of the MM fibre; (f) image of the 570 μm long pseudo-slit; (g) typical output light pattern of the single-mode pseudo-slit. Note that the image of the pseudo-slit is not to scale with the fibres, and the output light patterns are imaged through lenses that magnify the image.

SMs at the PL output can be arranged at will along the slit of the spectrograph.

Both the PIMMS and TIGER approaches can, in principle, enable very high-resolution MM spectrographs that exploit an Echelle grating (EG) for dispersion (Schwab et al. 2012; Betters et al. 2014). However, for a real spectrograph system, we ideally wish to use a single MCF–PL for capturing the telescope PSF and transporting it to a spectrograph, whilst also combining this capability with the mode-reformatting flexibility offered by PLs fabricated from individual SM fibres. As we have demonstrated previously (MacLachlan et al. 2017), one solution is the combination of an MCF–PL with a 3D integrated optical waveguide mode-reformatting component fabricated using ultrafast laser inscription (ULI) − an advanced laser manufacturing technique. We have demonstrated that this combination of technologies can be seamlessly integrated together to efficiently reformat the MM PSF of the CANARY AO system operating on the William Herschel Telescope to a SM pseudo-slit, with an on-sky throughput of 53 ± 4 per cent in the *H* band. Although the on-sky throughput results were promising, no results relating to the modal noise performance of the device were reported.

To address this, we characterized the device using a single wavelength to simulate high resolution, both experimentally and theoretically (Spaleniak et al. 2016). Initial findings suggested modal noise, whilst largely suppressed, was still present in the output of the device. This was in agreement with other experiments (Cvetojevic et al. 2017) and showed that to properly estimate the modal noise contribution from a photonic reformatter, a full characterization of the device was required.

In this paper, we use a simple NIR spectrograph to investigate in detail the modal noise performance of the photonic reformatter demonstrated on sky in MacLachlan et al. (2017), and compare its performance to SM and MM fibres. We call this device the 'hybrid' reformatter since it integrates an MCF–PL and a ULI fabricated mode reformatting component. In Section 2, we will outline the experimental design of the spectrograph and the experimental techniques used to investigate the modal noise performance. In Section 3, we describe the data processing methods and the results obtained, which demonstrate that near-SM performance can be obtained using the hybrid reformatter (HR). In Section 4, we link the precision of our device to potential scientific applications.

2 EXPERIMENTAL SPECTROGRAPH DESIGN AND DATA CAPTURE METHODS

We have designed an inexpensive bench-top spectrograph constructed from catalogue components, which enables observation and quantification of modal noise using different optical fibre feeds. For our purposes, light was fed into the spectrograph using three devices; the HR, an SMF28e fibre patch cord with FC/PC connectors at both ends, and a step index MM fibre. The SMF28e fibre exhibits a mode field diameter (MFD) of 10.4 ± 0.5 μm at 1550 nm and an NA of 0.12 based on its 0.36 per cent core-cladding refractive index contrast (Chandrasekharan et al. 2020). The MM fibre has a 50 μm core diameter and an NA of 0.22, again based on its 1.2 per cent core-cladding refractive index contrast (Thorlabs 2019). The MM input of the HR has a core diameter of 43 μm and an NA of 0.22 based on its 1.2 per cent core-cladding refractive index contrast, as specified by the manufacturer of the custom part. The pseudo-slit output exhibits a MFD of 8.5 μm at 1550 nm and a physical size of 6.7 ± 0.7 μm. Using this information, we have used BEAMPROP software to estimate the core-cladding refractive index contrast (0.65 ± 0.15 per cent), and from this we calculate the pseudo-slit exhibits an NA of 0.14 ± 0.02. All devices had a length of approximately 2 m. A schematic of the spectrograph design, images of the end-facets of the three devices, and their respective typical output light patterns are presented in Fig. 1. A schematic of the complete HR is presented in Fig. 2. It is crucial to highlight that the number of guided modes (around 124) supported in this 50 μm MM fibre at 1550 nm is reasonably close to the 92 modes processed by the HR. This MM fibre was chosen to facilitate the closest possible comparison using an off-the-shelf fibre.

For all characterization experiments, the light source used was an SM fibre-coupled broad-band amplified spontaneous emission (ASE) source (Thorlabs FL7002-C4) centred on 1560 nm with a bandwidth (measured at the −10 dB points relative to the peak) of approximately 75 nm, which is close to the centre of an M-dwarf emission spectrum. A bandpass filter (BPF; Thorlabs FB1550-12) with a full width at half-maximum (FWHM) of 12 nm was also used to ensure that the spectrum was within one free spectral range of the EG, eliminating the need for cross-dispersion. Neutral density (ND) filters were placed in the input beam path as necessary to avoid saturating the camera. Lens L1 is a 15.58 mm focal length fibre collimation package (NA 0.16) and lens L2 is a 10 mm focal length and 8 mm diameter achromatic doublet, producing an image
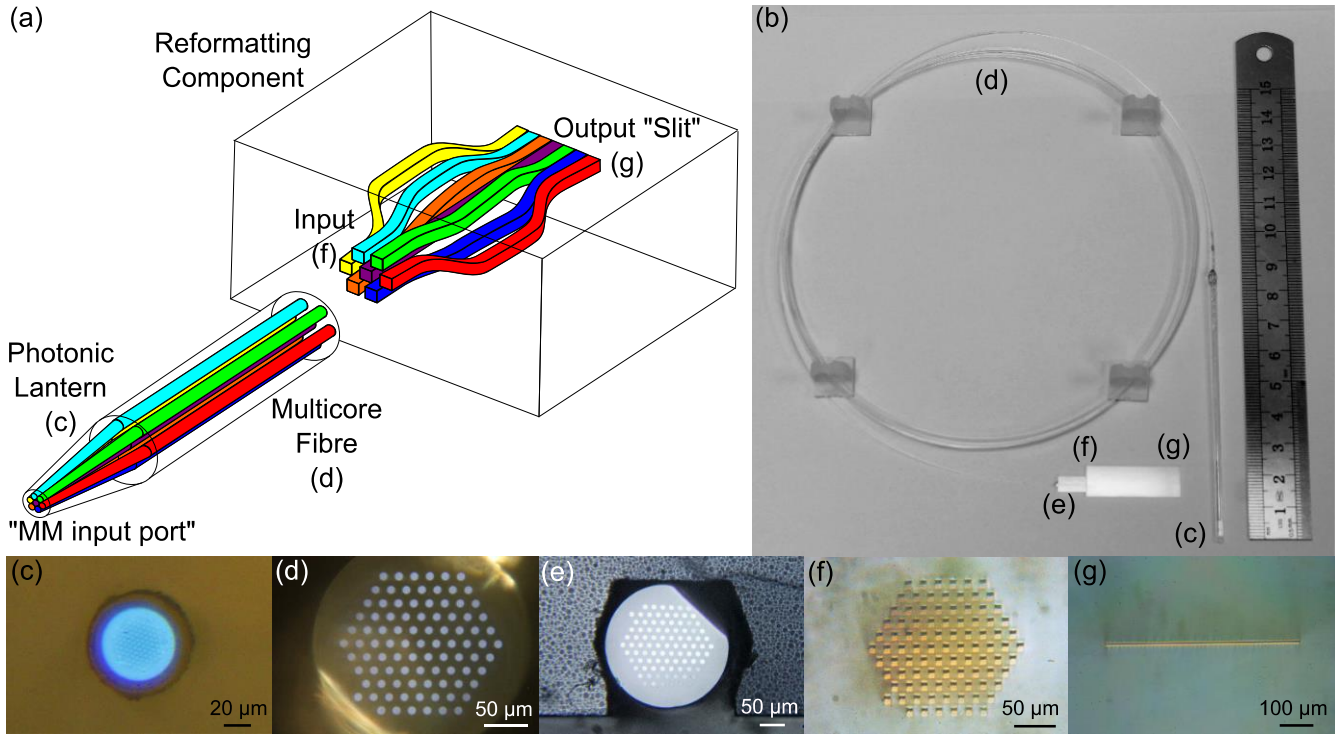
Figure 2. Key: (a) Schematic diagram of the complete device with the different colours showing the paths of the SMs, (b) Photograph of the device with 15 cm ruler for scale, (c) MM input facet of the PL, (d) MCF of 92 cores in a hexagonal array with a core-to-core pitch of 17.6 μm, (e) MCF placed in a V-groove, (f) input facet of the ULI reformatter chip, and (g) SM pseudo-slit output. From MacLachlan et al. (2017).

of the fibre mode that has an MFD of 6.7 ± 0.5 μm. This image is initially aligned with the input to the device under test (DUT) by maximizing the throughput. Lens L3 has 25.4 mm focal length, and lens L4 has 500 mm focal length for a magnification of ≈ 20. This magnification has been selected to allow the image of the pseudo-slit created by the HR to fill the majority of the detector height. The EG was sourced from Thorlabs (GE2550-0363) with 63° blaze angle and 31.6 lines mm^{-1}; this is used due to the high efficiency in higher orders, which greatly increases the dispersion and is essential to achieving a high resolution. M1 is a 2 inch square silver mirror used to fold the beam path and overcome restrictions from bulky optic mounts. This allows the grating to be used close to its design angle (the Littrow configuration). The output raw images are recorded by a Hamamatsu C10633-23 InGaAs camera, based on a detector cell of 256×320 pixels with a pixel size of 30×30 μm. The resolving power R of the spectrograph is $\lambda/\Delta\lambda$, where $\Delta\lambda$ is the FWHM of the line function. The resolving powers we calculate for each DUT are as follows: $R \approx 9500$ for SM fibre, $R \approx 3500$ for MM fibre, and $R \approx 7000$ for the HR.

To mimic the effect of the atmosphere and telescope slewing as stars are tracked across the sky, the coupling into the fibre was adjusted in a semirandom meander across the facet while maintaining a throughput greater than 80 per cent of the maximum at optimal coupling. At each fibre position, 250 frames were captured at 15 ms exposure time with the camera. These frames were then added together to produce a single detector image for that fibre position, simulating a longer and thus more relevant exposure time. The input coupling is modified successively to obtain 60 of these images, which were then processed according to Appendix A. In the following section, we discuss how the data were analysed using two different experimental protocols to quantify the modal noise when characterizing each DUT. We also investigate the effect of shaking

the DUT on the modal noise performance. To do so, a mechanical scrambling system was constructed by fixing the centres of two independently controlled loudspeakers to loops of the DUT, which is represented by S in Fig. 1(a).

3 DATA PROCESSING TECHNIQUES AND RESULTS

3.1 Characterizing modal noise from a broad-band measured spectrum

In our characterization system, modal noise manifests itself through changes in the measured spectrum as the input coupling is varied. The strength of the modal noise can therefore be determined by quantifying how the spectrum varies across the full data set. To do so, we compare the spectrum obtained from each of the 60 images to the mean spectrum across all images. A higher degree of modal noise will result in larger differences, which can then be quantified statistically. More specifically, 60 spectra were obtained by summing each processed image along the spatial axis (as described in Appendix A). Figs 3(a)–(d) illustrate examples of raw data (unprocessed images) acquired using a single input coupling position for each of the three DUTs, including examples where the MCF of the HR is either static or shaken during the exposure, and when shaken we define this as HRS. Only the data obtained using the MM fibre with shaking (MMS) is shown because the visual difference in the images taken using with and without shaking was low by eye. Figs 3(e)–(h) present spectra obtained from the raw data sets after processing, with the black line representing the average spectrum obtained across the 60 different input coupling positions, and the red line representing the spectrum out of the 60 that was most different from the average. The peak of the spectrum appears at slightly different positions on
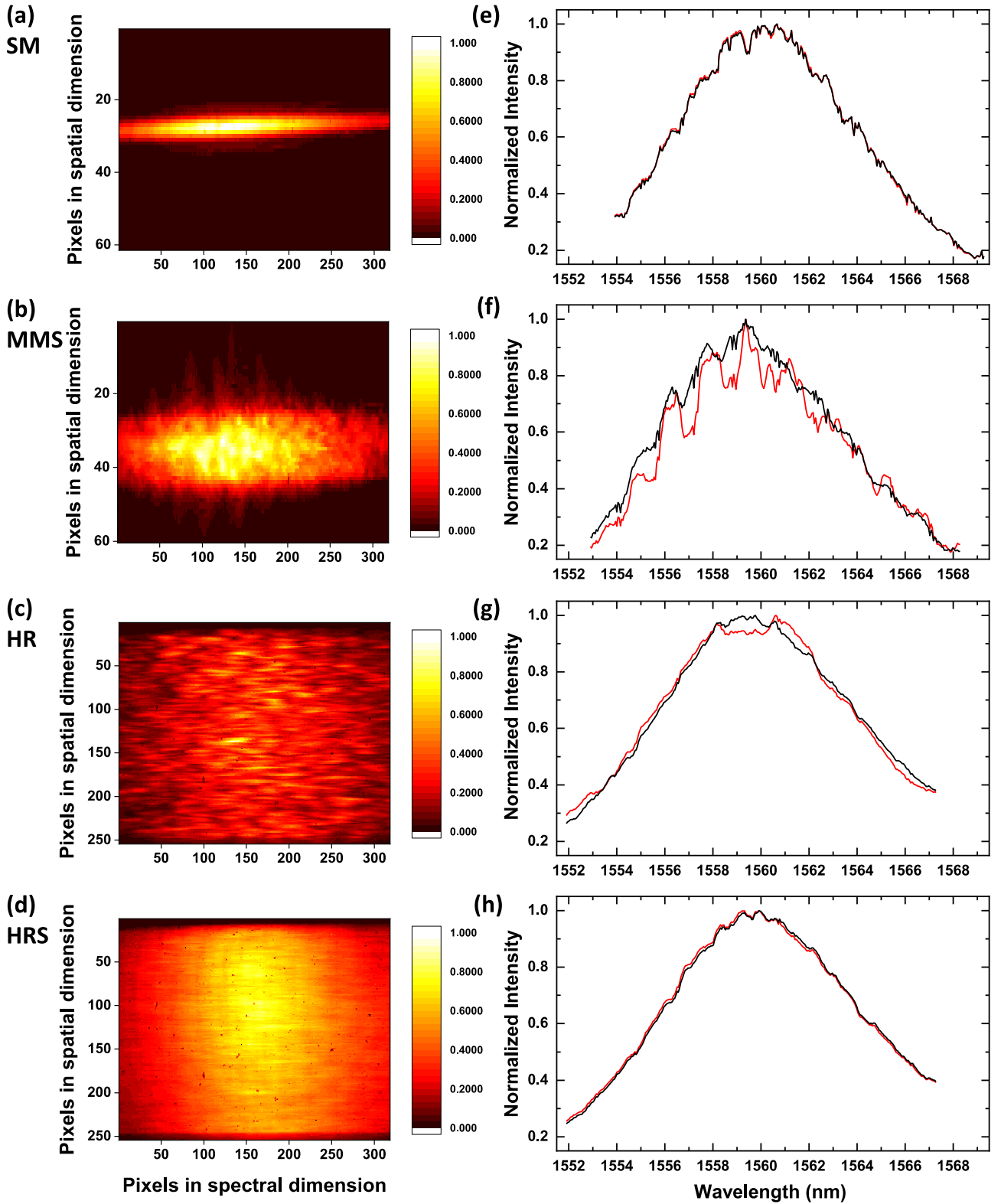
Figure 3. Examples of normalized coloured raw images for: (a) SM, (b) MMS, (c) HR and (d) HRS; Mean spectrum (the black line) and the most different spectrum (the red line) for (e) SM, (f) MMS, (g) HR, and (h) HRS. Each raw image corresponds to the most different spectrum. Some empty space on the detector with the SM and MM fibres has been omitted. Note that the normalization step shown here is shown for the benefit of the reader only, and does not form part of the data analysis in the manner depicted.

Spectra – 2 of 1×308 vectors   60 × absolute difference spectra   60 × normalized difference spectra
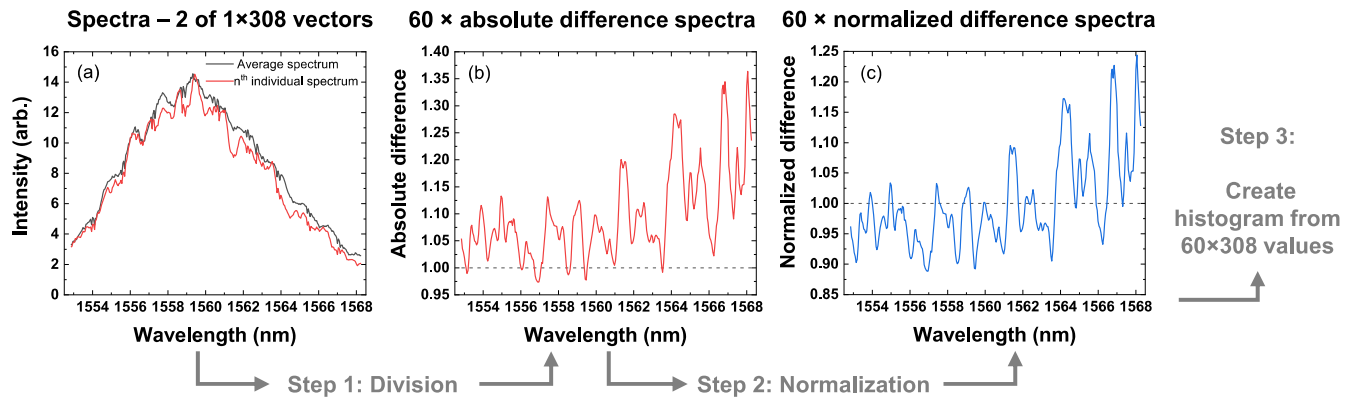
Figure 4. The three steps to obtain the histogram in Fig. 5 are illustrated using MMS data: (a) shows how the *n*th individual spectrum compares to the mean, (b) shows the absolute difference spectrum obtained by dividing these, and (c) shows the normalized difference spectrum. A histogram is then formed from the full data set of 60 × 308 elements.

the camera from one DUT to another due to small differences in the physical positioning of the DUT relative to the spectrograph. There is no reason to expect these differences will affect the analysis.

We provide five visualizations (available via MNRAS online - see links in 'supporting information' section) to show the effect that changing the input coupling has on the measured output, with each frame in the movie representing a different input coupling position. The difference between the data and spectra obtained using the SM fibre (Figs 3a and e) and the MMS image (Figs 3b and f) is immediately apparent. Here, we see the characteristically smooth spectrum obtained using the SM fibre, and the highly variable spectrum obtained using the MM fibre, the shape of which varies with input coupling. The difference between the spectra obtained using the HR and HRS devices is also observable, and we highlight the impact of the scrambling process in visualizations HRmov.mp4 and HRSmov.mp4. The HRS image appears very similar to the SM image spectrally, but with a large difference in the height of the area filled on the detector due to the length of the pseudo-slit. The modal noise phenomena we observe when using the HR to feed our spectrograph has some similarities to the modal noise phenomena initially observed in the RHEA instrument (Rains et al. 2016), which utilized an integral field unit with nine SM fibres. We note that the authors were also able to mitigate the modal noise in their system through fibre agitation.

The data processing steps followed to quantify the modal noise using the acquired data are depicted in Fig. 4 to aid the reader. First, by elementwise dividing the average spectrum by the nth (of 60) measured spectrum (Fig. 4a), we obtain a 308 value vector that represents the absolute deviations between the nth spectrum and average spectrum (Fig. 4b). This vector is then normalized such that the mean value is 1, which accounts for any variation in the absolute power of the nth spectrum (Fig. 4c). The deviation from unity in this vector is related to the modal noise. Once this process is applied to the full data set, a histogram of the 18 480 values, sorted into 40 bins, can be plotted to represent the spectral differences across all the 60 spectra due to modal noise. As seen in Fig. 5, the histograms (data points) that are generated by this data processing are well approximated by a Gaussian distribution, the best fit of which is also presented. We have normalized the histograms so that the Gaussian fit has a peak value of 1 to allow a straightforward comparison. The strength of the modal noise can be represented by the standard deviation (SD) of the fitted Gaussian, σ, and these can be found in Table 1, along with the goodness of fit.

Any light that is not guided within the ULI-fabricated reformatter, for example, due to coupling losses between the MCF cores and the reformatter waveguides, will significantly affect the performance of the spectrograph. To block the vast majority of this unguided light, we carefully placed opaque adhesive tape above and below the pseudo-slit at the output surface of the HR. We were also extremely careful to ensure that none of the light from the pseudo-slit itself was blocked. We have recently demonstrated how ultrafast laser microfabrication techniques can be used to create extremely precise versions of this mask (Pike et al. 2020), and such approaches will be exploited in the future to make optimal reformatting components with negligible spurious light signals.

By considering these results, it is apparent that the modal noise present in the spectra measured using the HRS is greatly reduced compared to when using either the HR or MMS devices, and is approaching the performance using the SM fibre. It should be highlighted that the width of the histogram obtained using the SM fibre represents the experimental limits of our characterization system. We see that the data obtained using the HR exhibits a factor of 2.6 reduction in modal noise compared to the data obtained with the MM device, and a factor of 2.0 reduction in modal noise compared to the data obtained using the MMS device. Shaking the MCF of the HR reduces the modal noise by a further factor of 2.9. The data obtained using MMS exhibit only a factor of 1.3 reduction in modal noise compared to the data obtained using the MM fibre. It is interesting to note that since the 9 μm diameter, 0.11 NA cores of the MCF are separated by only 17.6 μm, there will be significant intercore coupling of light along its ∼2 m length. We believe that this will help to 'thermalize' the distribution of light across the modes when the HR device is shaken, and hence result in an improved modal noise performance. The total amount of modal noise mitigation is a factor of 5.7 between the HRS and the MMS – using the same scrambling system, with a small difference in number of guided modes. These results clearly demonstrate the superior scrambling ability of the HR device in comparison to the MM fibre, and demonstrates our first method to quantify how a photonic reformatter such as the HR can efficiently mitigate modal noise.

3.2 Characterizing modal noise from the barycentre precision of spectral peaks

The results outlined in Section 3.1 provide a straightforward route to quantify modal noise and modal noise mitigation, but do not
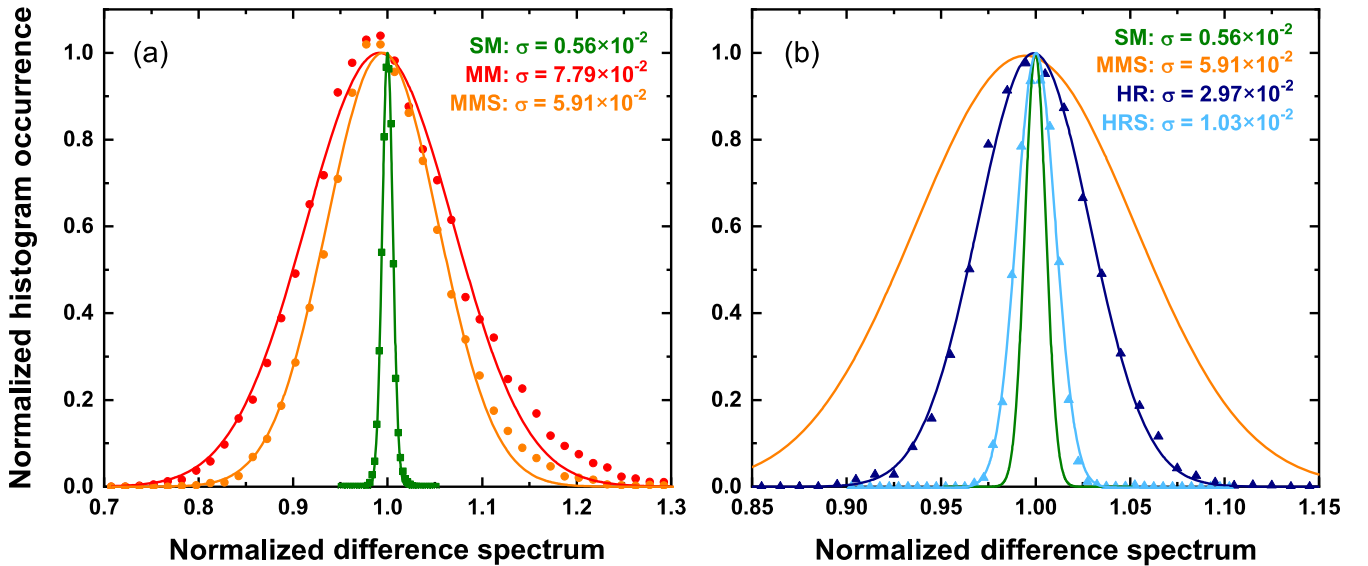
Figure 5. The data represents the histogram of the difference between spectra at different coupling positions, with a wider distribution indicating larger differences in intensity for each wavelength unit. The solid lines are a Gaussian fit to the data. (a) Normalized occurrence of difference spectrum value with changing coupling in MM (the red circles), MMS (the orange circles), and SM (the green squares) fibres; (b) Normalized occurrence of difference spectrum value with changing coupling in the HR (the dark blue triangles) and in the HRS (the light blue triangles) superimposed on to SM (the green curve) and MMS (the orange curve).

Table 1. Parameters of the fits to difference spectrum data in Fig. 5. We present σ with a factor 10^{-2} removed for ease of comparison.

| Device	SD σ ($\times 10^{-2}$)	R^2 goodness of fit
SM	0.56	0.998
MM	7.8	0.989
MMS	5.9	0.995
HR	3.0	0.997
HRS	1.03	0.996

provide an immediate quantification of how modal noise affects the precision of a spectrograph. To address this, we have investigated a second method to quantify modal noise. This method uses the same characterization system shown in Fig. 1, but with a Fabry–Pérot etalon placed in the input beam path between L1 and L2, converting the smoothly varying broad-band light source into a series of discrete spectral peaks spaced by a regular frequency interval – the etalon free spectral range. As outlined previously, modal noise generates variations in the acquired spectra as the input coupling is varied. Here, we use the measured spectral stability of the etalon peaks under different input coupling conditions as a proxy for the strength of modal noise using different DUTs. The etalon we chose was sourced from Light Machinery and was made from solid fused silica with a thickness of 0.821 mm and surface reflectivities of ∼0.885 and ∼0.873, respectively. These parameters produce an etalon with a finesse of 23, generating spectral peaks with a width of approximately 40 pm spaced by ≈1 nm around 1550 nm. This etalon was chosen since the spectral peaks are sufficiently spaced such that they can still be resolved by the spectrograph when fed using light via the MM fibre. It is important to note that when using a light source with these narrow-line properties we are, in effect, observing the modal noise that would be observed using a broad-band source and a spectrograph with a resolving power (R) of ≈40 000 (1550 nm/40 pm), even though we are actually using a spectrograph

with an $R \approx 9500$ for the SM fibre feed, $R \approx 7000$ for the HR feed, and $R \approx 3500$ for the MM fibre feed.

In Figs 6(a)–(d), we present the raw images of data acquired using three DUTs (again with both unshaken and shaken conditions for the MCF of the PL). In Figs 6(e)–(h), we present how the acquired spectrum varies with input coupling, again with the solid black line indicating the average spectrum for 60 measurements, and a sample of 5 of these spectra at different coupling positions represented by the coloured dashed lines. Again, since there is a lack of visual difference between the MM fibre with and without shaking, only the MMS measurements are presented in Fig. 6. We again used the process outlined in Appendix A to correct for deviations in the straightness of the pseudo-slit and the angle between the pseudo-slit and the pixel axes of the camera.

For each of the spectral peaks generated by the etalon, a Gaussian fit was made to determine the central wavelength (barycentre). The fit was typically over 10 pixels that gave a high confidence in the precision. The variation in the acquired spectra is due to modal noise while varying the input coupling, which in turn results in variations in the measured barycentres of each peak. Thus, the SD of the 60 measured barycentres for each peak is our second measure of modal noise. These data are plotted in Figs 7(a and b), where the x-axis position of each data point represents the average measured barycentre for an etalon peak, and the y-axis position of each data point is the SD of the 60 measured barycentres for that spectral peak.

It is also useful to plot these barycentres as a ratio of the width of the peaks themselves, as this can link the precision to the resolution, plotted in Fig. 7(c). We calculate the peak width from the FWHM of the Gaussian fit. The large uncertainty for the MM/MMS measurements is due to the non-Gaussian shape of the peaks providing an imprecise fit. In Table 2, we present the mean values (and associated uncertainty from the SD of those 16 values) of the barycentre stability over each of the 16 peaks, calculated from the SD of 60 barycentres as seen in Fig. 7. It is apparent that the
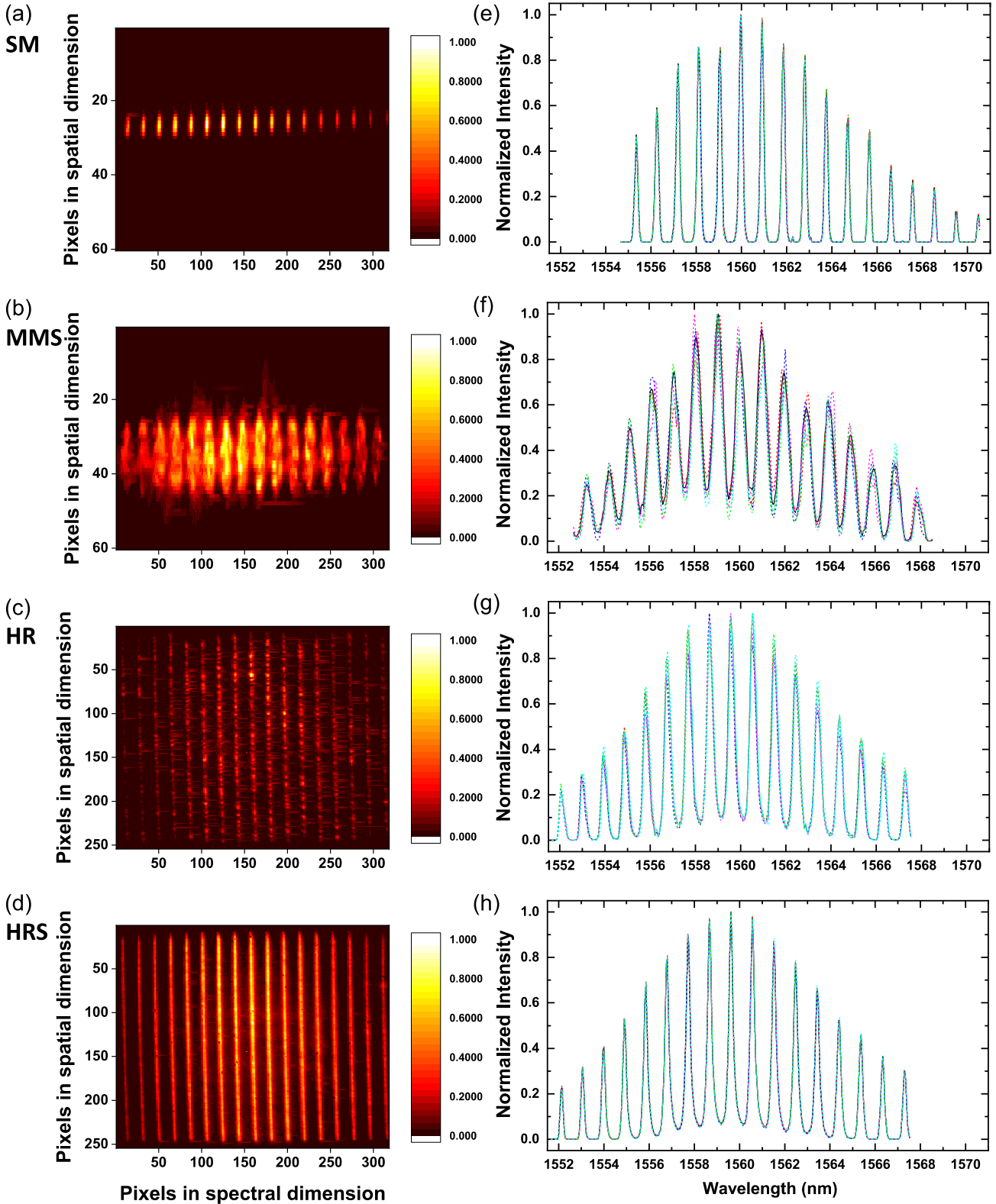
Figure 6. Examples of normalized coloured raw images with the etalon for (a) SM, (b) MMS, (c) HR, and (d) HRS; Examples of five randomly chosen spectra (the dashed line) and the mean spectrum (the solid line) for (e) SM, (f) MMS, (g) HR, and (h) HRS. Again, we present raw images of the most different spectra, and some empty space on the detector with the SM and MM fibres has been omitted.

49

(a)

(b)

(c)
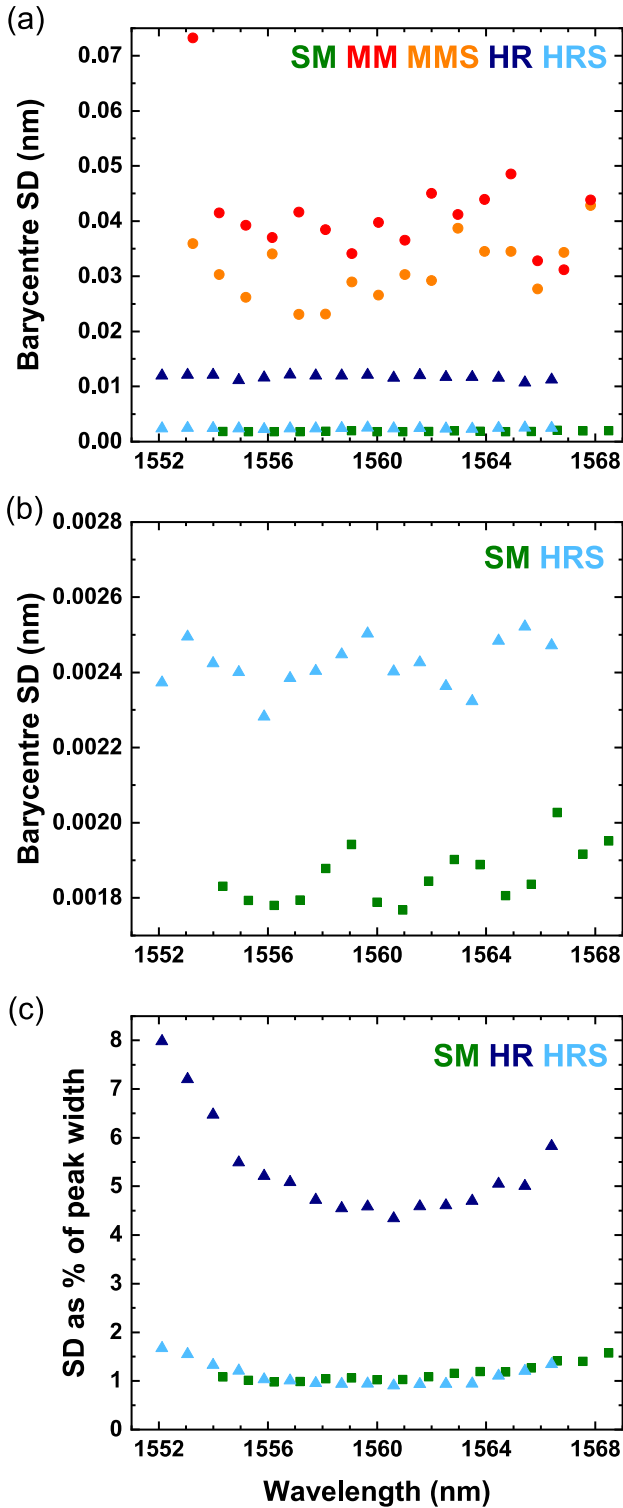
Figure 7. (a) Standard deviation of 60 calculated barycentres for each spectral peak at the given average wavelength, where the green squares correspond to SM, the red circles to MM, the orange circles to MMS, the dark blue triangles to HR, the light blue triangles to HRS; (b) Close-up of SM and HRS in (a); (c) Standard deviation of 60 calculated barycentres, plotted as a percentage of the respective peak's width, for each spectral peak at the given average wavelength. The spectra of each DUT were sampled at different positions that cause the slight offset on the graph.

Table 2. Average values of the barycentre precision presented in Fig. 7. We present the SD with a factor 10^{-3} removed for ease of comparison.

Device	Mean SD ($\times 10^{-3}$ nm)	Mean SD as per cent of peak width
SM	1.86 ± 0.07	1.2 ± 0.2
MM	42 ± 10	8 ± 2
MMS	31 ± 6	6 ± 2
HR	11.7 ± 0.4	5.3 ± 1.0
HRS	2.42 ± 0.07	1.1 ± 0.2

photonic approach using HRS offers a significant improvement over the MM fibre and a performance close to that measured using the SM fibre, and also that the mode scrambling system is highly effective – reducing the modal noise by a factor of 5 compared to when using the HR without shaking. The variation of the barycentre across the pseudo-slit with the HRS is 1.1 per cent of the peak width. The effect of shaking the MM fibre is again observed to be minimal compared to when shaking the HR. The mean SD as a percentage of the peak width for the SM fibre is equal to the HRS, showing their equivalent performance in this spectrograph.

3.3 Correcting for variations in the laboratory temperature

Our experiments were performed in a basic lab without the 0.01 K temperature control and vacuum chambers used in a state-of-the-art spectrograph. Temperature effects can therefore introduce instabilities in the spectrum that are not due to modal noise. For example, the true spectral positions of the etalon peaks may drift by 10 pm K^{-1} (Williams & Dean 2020). With the aim of accounting for the impact of laboratory thermal fluctuation on our barycentre method of quantifying modal noise, we have also conducted the following additional analysis.

It is logical to assume that laboratory temperature drifts will have a very similar effect on the spectral peaks across the measurement, since the wavelength span of the measurement is very small. Therefore, by examining the manner in which the measured spectrum shifts for each of the 60 measurements compared to the mean spectrum measured across all 60, it should be possible to substantially account and correct for laboratory temperature variations.

For a given spectrum, we use the average deviation of 15 etalon peaks from their mean positions (across the 60 measurements) as a proxy to represent how much the spectrograph has drifted from its mean position due to thermal effects – we call this shift the 'temperature proxy'. The temperature proxy was observed to gradually vary over the 60 measurements with a full range of ~8 pm. This would, for example, correspond to an etalon temperature range of slightly less than one degree. We then spectrally shift each of the 60 spectra by the temperature proxy, such that the mean position of 15 peaks is the same across all 60 measurements. This approach will compensate for variations in the laboratory temperature, leaving only the instability in the peak positions due to modal noise.

A Fourier transform of the difference spectrum between the mean spectrum in Fig. 3(h) and any one of the 60 contributing spectra indicates that the modal noise in the HRS occurs with a period that is ~25 per cent shorter than the period of the etalon peaks. Every third etalon peak therefore samples the modal noise with the same phase, meaning that the effect of the modal noise on the mean barycentre shift is negligible when considering every group of three adjacent etalon peaks. We therefore calculated the temperature proxy using the 15 etalon peaks lying closest to the

(a)

(b)
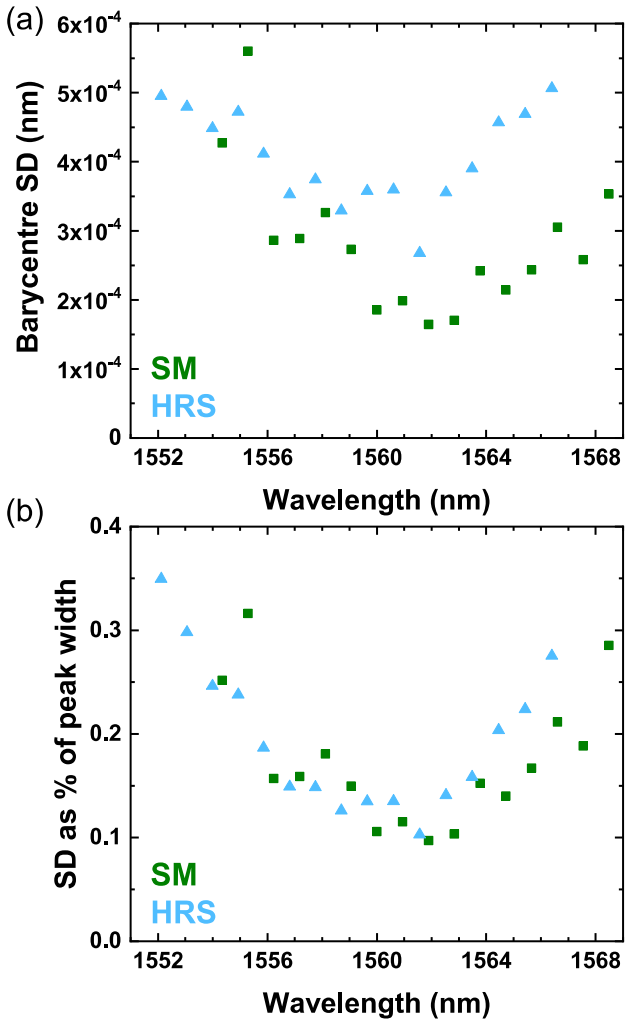
Figure 8. (a) Standard deviation of 60 calculated barycentres when laboratory temperature correction is applied to the data, for each spectral peak at the given average wavelength, where the green squares correspond to SM and the light blue triangles to HRS; (b) Standard deviation of 60 calculated barycentres when laboratory temperature correction is applied to the data, plotted as a percentage of the respective peak's width, for each spectral peak at the given average wavelength. The spectra of each DUT were sampled at different positions that cause the slight offset on the graph.

centre of the wavelength span (an integer of 3), rather than the 16 available, to minimize the potential to subtract contributions to the mean barycentre shift that are due to modal noise. To provide further confidence, we also confirmed that temperature proxy did not vary significantly when using either 14, 15, or 16 peaks to evaluate its magnitude.

The SD of the position of each of the etalon peaks relative to their respective mean positions can then be recalculated, and plotted to generate 'laboratory temperature corrected' versions of Figs 7(b) and (c), presented as Figs 8(a) and (b). In Table 3, we present the mean values of the data shown in Fig. 8. When compared to the data presented in Table 2, it is clear that accounting for the effect of laboratory temperature increases the stability of the etalon spectral peaks by a factor of ∼6 for both the SM and HRS DUTs. It is also interesting to note the shape of the curves shown in Fig. 8, where the etalon peaks are observed to be most stable in the middle of the spectral range. This, we believe, is due to the spectral peaks

Table 3. Average values of the barycentre precision presented in Fig. 8. We present σ with a factor 10^{-3} removed for ease of comparison.

Device	Mean SD ($\times 10^{-3}$ nm)	Mean SD as per cent of peak width
SM	0.28 ± 1.0	0.17 ± 0.06
HRS	0.41 ± 0.7	0.19 ± 0.07

being physically wider on the detector array in the centre of the spectral range, becoming progressively narrower to either side (the difference between the widest and narrowest peaks are factors of 1.5 and 1.9 for SM and HRS, respectively). This may be due to field curvature resulting from lens L4 that prohibits all wavelengths from simultaneously being in focus on the flat detector, and ZEMAX simulations support this belief. There is no reason to suggest that it will not be possible, with a more carefully engineered spectrograph, to achieve the stability observed with the etalon peaks in the centre of the spectral range.

Fig. 8(b) indicates that the barycentres of the etalon peaks at around 1562 nm are stable to a thousandth of the width of the peak for both the SM and HRS DUTs. Based on a barycentre precision of 8 ± 2 per cent of the peak width for the MM fibre DUT, the HRS was observed to result in a factor of 100 improvement in the barycentre stability. Anagnos et al. (2018) have used beam propagation simulations to model the propagation of light through a photonic reformatting component similar to the HR device investigated here, and concluded that they should increase the barycentre precision by a factor of 1000 compared to a 50 μm core MM fibre. It is important to note, however, that since the data we have obtained here using the SM DUT only represents the modal noise measurement limit of our characterization system and methods, Fig. 8(b) merely demonstrates that HRS exhibits a level of modal noise that is not detectable using our experimental system and the methods we have described. With an improved experimental system and optimized experimental protocol, it is logical to expect that the graphs presented in Fig. 8 will both reduce in magnitude further and eventually separate, with the data for the SM DUT dropping further.

4 COMMENTS ON ACHIEVABLE RADIAL VELOCITY PRECISION

Our study has indicated that if we were to build a temperature stabilized spectrograph fed by HRS, we would be able to achieve a barycentre stability of 0.41×10^{-3} nm. This would infer that a single spectroscopic line could be measured to an accuracy of ∼80 m s^{-1}, assuming all other sources of noise are negligible. We therefore conclude that if our spectrograph (or similar) was placed in an environmentally controlled container, it would already operate with a precision close to that required for scientific applications, e.g. for detecting hot Jupiters such as WASP-19b (Hebb et al. 2010), which orbits a star of 12th magnitude and requires a high-throughput spectrograph such as one enabled by this device. If the HRS was used to feed light into a higher resolution spectrograph (such as ≈120 000 offered by the current state-of-the-art) using a camera with smaller pixel size (15 × 15 μm is the current state of the art) we might expect the 0.1 per cent stability of HRS barycentre relative to the physical peak width to result in a single line RV precision around 1 m s^{-1}, again assuming all other sources of noise (e.g. increased role of detector noise due to the length of the slit) are negligible. This is easily low enough to detect a terrestrial exoplanet in the habitable zone around an

M-dwarf. We also note the fact that real RV measurements are almost always made by cross-correlating full spectra consisting of many spectral lines, and so it is reasonable to conclude that the achievable precision when limited by modal noise could be significantly higher.

5 CONCLUSIONS

We have developed a bench top NIR spectrograph to characterize the modal noise performance of a photonic reformatter called the HR that reformats a telescope PSF to a diffraction-limited pseudo-slit. We used the spectrograph to compare the modal noise performance of the HR to that exhibited by two reference devices: a single-mode fibre and a MM fibre that supported a similar number of guided modes. We also investigated the effect of mechanical shaking on the modal noise.

We used two methods to quantify the strength of the modal noise. In the first, we used a spectrally smooth broad-band source and a statistical analysis to quantify how the entire acquired spectrum changed as a result of different input coupling conditions to simulate the effect of telescope slewing and tracking during an exposure. Using this method, we observed that the modal noise performance of the HR when shaken was a factor of ≈6 better than that observed using the MM fibre when shaken, but a factor of ≈2 worse than when using the SM.

In the second, we used a broad-band source consisting of multiple spectrally narrow peaks to quantify how the barycentres of the peaks shift as a result of different input coupling conditions. In this case, we observed that the modal noise performance of the HR when shaken was identical to that of the SM, but we again highlight that this merely indicates that the HR when shaken exhibits a level of modal noise that is not detectable using our experimental system and the barycentre method we have described.

Finally, looking forward to science applications, we have considered the relevance of our modal noise characterization tests in the context of NIR RV measurements, concluding that HR devices could offer a powerful route to combine high throughput efficiencies enabled by multimode operation with high precision spectroscopy through strong modal noise mitigation.

ACKNOWLEDGEMENTS

DATA AVAILABILITY

The raw data is available on Heriot-Watt University's Pure data repository (Pike & MacLachlan 2020).

REFERENCES

Anagnos Th. et al., 2018, MNRAS, 478, 4881
Angel J. R. P., Adams M. T., Boroson T. A., Moore R. L., 1977, ApJ, 218, 776
Anglada-Escudé G. et al., 2016, Nature, 536, 437
Barden S. C., 1994, in Pyper D. M, Angione R. J., eds, Proc. ASP Conf. Ser. Vol. 55, Optical Astronomy from the Earth and Moon. Astron. Soc. Pac., San Francisco, p. 130
Baudrand J., Walker G. A. H., 2001, PASP, 113, 851
Betters C. H., Leon-Saval S. G., Bland-Hawthorn J., Richards S. N., Birks T. A., Gris-Sánchez I., 2014, in Ramsay S. K., McLean I. S., Takami H., eds, Proc. SPIE Conf. Ser. Vol. 9147, Ground-Based and Airborne Instrumentation for Astronomy V. SPIE, Bellingham, p. 91471I
Betters C. H., Bland-Hawthorn J., Sukkarieh S., Gris-Sánchez I., Leon-Saval S. G., 2020, IEEE Photonics Technol. Lett., 32, 7
Birks T. A., Gris-Sánchez I., Yerolatsitis S., Leon-Saval S. G., Thomson R. R., 2015, Adv. Opt. Photonics, 7, 107
Bland-Hawthorn J. et al., 2010, in McLean I. S., Ramsay S. K., Takami H., eds, Proc. SPIE Conf. Ser. Vol. 7735, Ground-Based and Airborne Instrumentation for Astronomy III. SPIE, Bellingham, p. 77350N
Blind N., Conod U., Wildi F., 2017, Presentation at 'Adaptive Optics for Extremely Large Telescopes 5 (AO4ELT5)', Tenerife, Canary Islands, Spain, June 25–30, 2017. Available at: http://research.iac.es/congreso/AO4ELT5/media/proceedings/proceeding-094.pdf (accessed January 15, 2020)
Borucki W. J, Summers A. L., 1984, Icarus, 58, 1
Catanzarite J., Shao M., 2011, ApJ, 738, 151
Chandrasekharan H. K., Ehrlich K., Tanner M. G., Haynes D. M., Mukherjee S., Birks T. A., Thomson R. R., 2020, APL Photonics, 5, 061303
Charbonneau D., Brown T. M., Latham D. W., Mayor M., 2000, ApJ, 529, 45
Claudi R. et al., 2017, Eur. Phys. J. Plus, 132, 364
Crepp J. R. et al., 2016, in Evans C. J., Simard L., Katami H., eds, Proc. SPIE Conf. Ser. Vol. 9908, Ground-based and Airborne Instrumentation for Astronomy VI. SPIE, Bellingham, p. 990819
Cvetojevic N. et al., 2017, Optics Exp., 25, 21
Dressing C. D., Charbonneau D., 2013, ApJ, 767, 95
Fischer D. A. et al., 2016, PASP, 128, 066001
Gillon M. et al., 2017, Nature, 542, 23
Gris-Sánchez I., Haynes D. M., Ehrlich K., Haynes R., Birks T. A., 2018, MNRAS, 475, 3
Haynes D. M., Gris-Sánchez I., Birks T. A., Haynes R., 2018, in Navarro R., Geyl R., eds, Proc. SPIE Conf. Ser. Vol. 10706, Advances in Optical and Mechanical Technologies for Telescopes and Instrumentation III. SPIE, Bellingham, p. 1070665
Hebb L. et al., 2010, ApJ, 708, 224
Hill K. O., Tremblay Y., Kawasaki B. S., 1980, Opt. Lett., 5, 6
Iuzzolino M., Tozzi A., Sanna N., Zangrilli L., Oliva E., 2014, in Ramsay S. K., McLean I. S., Takami H., eds, Proc. SPIE Conf. Ser. Vol. 9147, Ground-based and Airborne Instrumentation for Astronomy V. SPIE, Bellingham, p. 914766
Jovanovic N. et al., 2016, in Evans C. J., Simard L., Katami H., eds, Proc. SPIE Conf. Ser. Vol. 9908, Ground-based and Airborne Instrumentation for Astronomy VI. SPIE, Bellingham, p. 99080R
Koch D. G. et al., 2010, ApJ, 713, 79
Leon-Saval S. G., Birks T. A., Bland-Hawthorn J., Englund M., 2005, Opt. Lett., 30, 2545
Leon-Saval S. G., Betters C. H., Bland-Hawthorn J., 2012, in Navarro R., Cunningham C. R., Prieto E., eds, Proc. SPIE Conf. Ser. Vol. 8450, Modern Technologies in Space- and Ground-based Telescopes and Instrumentation II. SPIE, Bellingham, p. 84501K
MacLachlan D. G. et al., 2017, MNRAS, 464, 4950
Mahadevan S., Halverson S., Ramsey L., Venditti N., 2014, ApJ, 786, 1
Mayor M., Queloz D., 1995, Nature, 378, 355
Mayor M. et al., 2003, The Messenger, 114, 20
Morris T. J., Corrigan M., Harris R. J., 2016, in presentation at 'CLEO: Applications and Technology 2016', California, United States, June 5-10, 2016. Available at: https://doi.org/10.1364/CLEO_AT.2016.JF2N.2 (accessed January 7, 2020)
Mulders G. D., Pascucci I., Apai D., 2015, ApJ, 798, 112

Oliva E. et al., 2015, A&A, 581, A47

Osterman S. N., Ycas G. G., Donaldson C. L., Diddams S. A., Mahadevan S., Ramsey L. W., Plavchan P. P., 2014, in Ramsay S. K., McLean I. S., Takami H., eds, Proc. SPIE Conf. Ser. Vol. 9147, Ground-based and Airborne Instrumentation for Astronomy V. SPIE, Bellingham, p. 91475C

Pepe F. A. et al., 2010, in McLean I. S., Ramsay S. K., Takami H., eds, Proc. SPIE Conf. Ser. Vol. 7735, Ground-Based and Airborne Instrumentation for Astronomy III. SPIE, Bellingham, p. 77350F

Petersburg R. R., McCracken T. M., Eggerman D., Jurgenson C. A., Sawyer D., Szymkowiak A. E., Fischer D. A., 2018, ApJ, 853, 2

Pike F. A., MacLachlan D. G., 2020, in Modal noise mitigation for high-precision spectroscopy using a photonic reformatter - support data. Heriot-Watt University

Pike F. A. et al., 2020, Proc. SPIE Conf. Ser. Vol. 11451, Advances in Optical and Mechanical Technologies for Telescopes and Instrumentation IV. SPIE, Bellingham, p. 11451

Plavchan P. P. et al., 2013, in Shaklan S., ed., Proc. SPIE Conf. Ser. Vol. 8864, Techniques and Instrumentation for Detection of Exoplanets VI. SPIE, Bellingham, p. 88640G

Quirrenbach A. et al., 2018, in Evans C. J., Simard L., Takami H., eds, Proc. SPIE Conf. Ser. Vol. 10702, Ground-based and Airborne Instrumentation for Astronomy VII. SPIE, Bellingham, p. 107020W

Rains A. D. et al., 2016, in Evans C. J., Simard L., Katami H., eds, Proc. SPIE Conf. Ser. Vol. 9908, Ground-based and Airborne Instrumentation for Astronomy VI. SPIE, Bellingham, p. 990876

Rawson E. G., Goodman J. W., Norton R. E., 1980, J. Opt. Soc. Am., 70, 8

Reiners A., Bean J. L., Huber K. F., Dreizler S., Seifahrt A., Czesla S., 2010, ApJ, 710, 432

Roy A., Chakraborty A., Mahadevan S., Chaturvedi P., Prasad N. J. S. S. V., Shah V., Pathan F. M., Anandarao B. G., 2016, in Evans C. J., Simard L., Katami H., eds, Proc. SPIE Conf. Ser. Vol. 9908, Ground-based and Airborne Instrumentation for Astronomy VI. SPIE, Bellingham, p. 99086R

Schwab C., Leon-Saval S. G., Betters C. H., Bland-Hawthorn J., Mahadevan S., 2012, in Haghighipour N., ed., Proc. IAU Symp. 293, Formation, Detection, and Characterization of Extrasolar Habitable Planets. Kluwer, Dordrecht. p. 403

Spaleniak I. et al., 2016, in Navarro R., Burge J. H., eds, Proc SPIE Conf. Ser. Vol. 9912, Advances in Optical and Mechanical Technologies for Telescopes and Instrumentation II. SPIE, Bellingham, p. 991228

Thorlabs specification sheet for part FG050LGA, 2019, web page. Available at: https://www.thorlabs.com/drawings/439e7b5e20ecea9d-8DF19B3E-9FF3-64AB-87AC4C45BF085F0B/M42L02-AutoCADPDF.pdf (accessed June 2, 2020)

Williams E., Dean J., 2020, LightMachinery Inc., web page. Available at: https://lightmachinery.com/optical-design-center/more-optical-design-tools/etalon-tuning/ (accessed January 10, 2020)

SUPPORTING INFORMATION

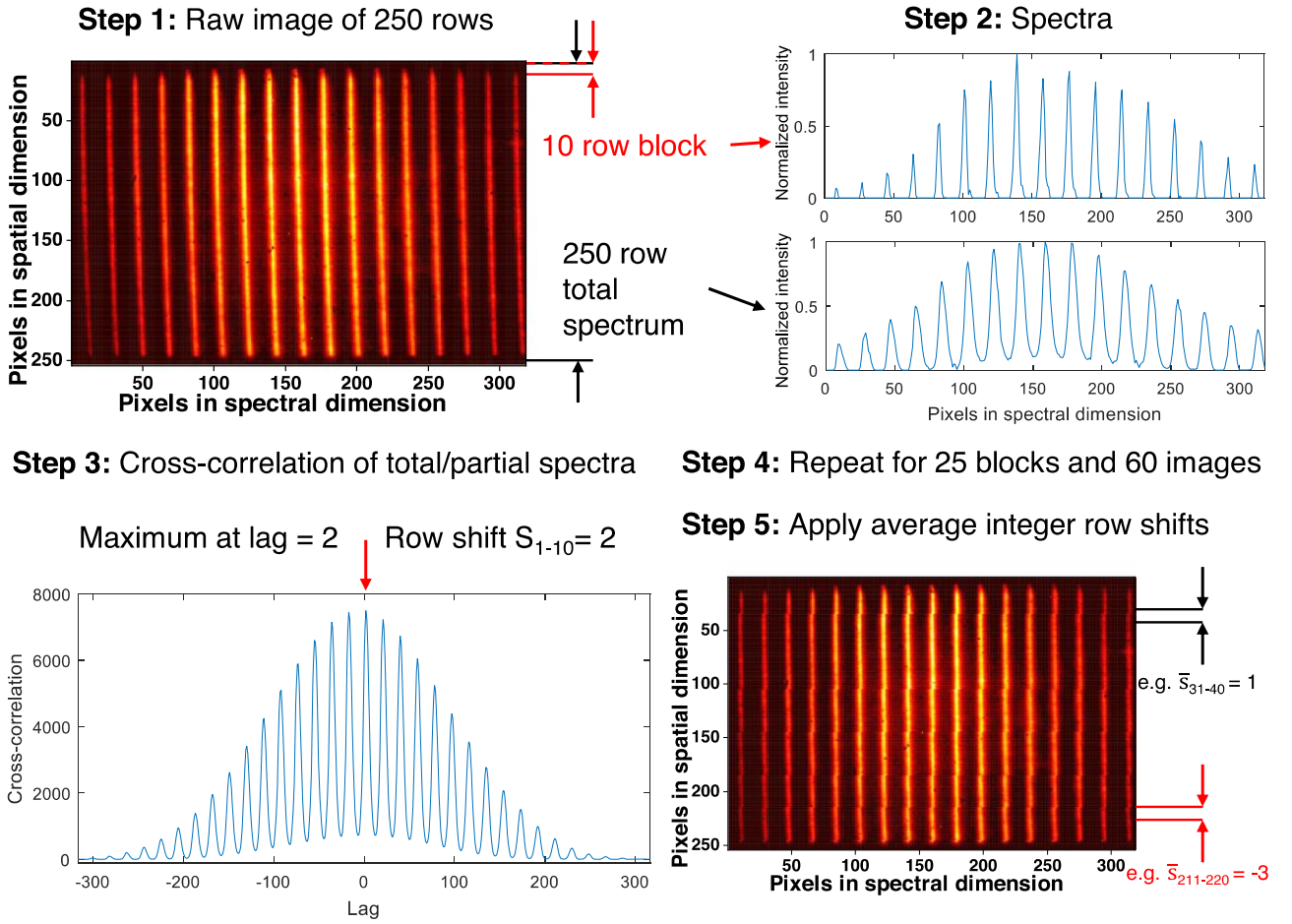Supplementary data are available at *MNRAS* online.

HRmov.mp4
HRSmov.mp4
MMmov.mp4
MMSmov.mp4
SMmov.mp4

Please note: Oxford University Press is not responsible for the content or functionality of any supporting materials supplied by the authors.

Any queries (other than missing material) should be directed to the corresponding author for the article.

APPENDIX A: PROCESS TO CREATE SPECTRA FROM RAW DATA

After gathering the 60 images, some initial data processing was performed. The five hot pixels identified on the camera were all set to zero, and the outermost rows and columns of the camera images were removed from the data as they did not register any light, which results in a matrix of 254×318 elements. Additionally, there is a small but non-trivial angle between the peaks formed by the etalon when the pseudo-slit is imaged on the detector, and the spatial axes of the camera; this is most easily noticeable in Fig. 6(d). The process to 'straighten' the image is explained here with the aid of a schematic in Fig. A1. A calibration file was determined from the data gathered using the HRS, since this is more reliable than the non-shaken conditions. Starting with one image of 250 rows (we eliminate the top four empty rows to achieve a multiple of 10; Step 1), we obtain a partial spectrum for each block of 10 rows in an image (summed along the axis orthogonal to the dispersion), which we can compare to the 250-row spectrum (Step 2). We perform a cross-correlation of the two spectra, and the lag corresponding to the peak of the cross-correlation is where they show most similarity (Step 3). We did this using summed sections of 10 rows because a cross-correlation using individual rows was prone to error. Applied to the full data set, this lag, corresponding to the mth block of rows in the nth image, was set as element (m,n) in a 25×60 matrix (Step 4). This calibration matrix was then averaged down the 60 columns and rounded to an integer to determine how much each block of rows should be shifted (Step 5). The range of the shift required was ~ 7 pixels over the full length of the pseudo-slit. The calibration file was applied consistently to all 60 images in both the shaken and unshaken data sets. The resolution increased by 50 per cent — becoming more comparable to the resolution of the spectrograph when fed with SM fibre. The 'straightened' images were then summed down the spatial axis to create 60 spectra as before. This process was not used to correct the data from the SM fibre as the small angle and minimal number of rows spatially occupied by the image made the process needless. In addition to this reason being applicable to the MM fibre (albeit to a lesser extent), the modal noise present meant this method of cross-correlation was unreliable and actually decreased the resolution. In this case, it would also not be reasonable to use the same calibration file as for the pseudo-slit because the spectrograph needed some small physical adjustments to accommodate the differently shaped outputs. The calibration file was retrospectively applied to the broad-band images of the pseudo-slit without the etalon to ensure the statistical analysis we perform in section 3.1 used the spectrograph at the same resolution. The wrapping of rows when shifted caused some errors on the edges of the images, so the outer five columns on each side were truncated to ensure no unnecessary errors in the spectra were introduced by the data processing. For each DUT, to determine the relationship between pixel number and wavelength a tuneable laser (Anritsu MG9638A) was scanned across the detector in 1 nm increments. A straight line fit then gave the conversion factor (since the small wavelength range does not introduce non-linear dispersion).

53

Step 1: Raw image of 250 rows

Step 2: Spectra

Step 3: Cross-correlation of total/partial spectra

Step 4: Repeat for 25 blocks and 60 images

Step 5: Apply average integer row shifts

Figure A1. The five steps to straighten the image of the pseudo-slit on the detector are presented. Step 1 is to select a raw image of 250 rows. Step 2 is to generate the total spectrum and a partial spectrum from a 10 row block. Step 3 is to perform a cross-correlation between these spectra. The lag corresponding to the maximum value is the row shift for that block and particular image. Step 4 is to repeat this for 25 blocks and 60 images to generate a matrix. The average row shift for each block is calculated and rounded to the nearest integer. Step 5 is to apply the row shifts for each block consistently for all images.

This paper has been typeset from a TeX/LaTeX file prepared by the author.

54

Chapter 3 - Diffraction-limited integral-field spectroscopy for extreme adaptive optics systems with the Multi-Core fiber-fed Integral-Field Unit

3.1 Introduction

Exoplanets can be detected and analysed using a variety of techniques, examples of which include transit photometry and radial velocity measurements. A third technique that has increased in popularity in recent years is direct imaging, but the technical challenges involved are significant due to the fact that the exoplanet is usually between 4 and 10 orders of magnitude fainter than the star they orbit, and also the fact that they typically orbit within 1 arcsec of the star. As a result, direct imaging has only recently become feasible due to advances in AO which reduces the impact of atmospheric seeing, coronagraphs that block the starlight while efficiently passing light from regions surrounding the star, and image processing techniques to separate the exoplanet light from the remaining starlight.

Direct imaging on its own is powerful, but to fully characterise exoplanets and other objects such as protoplanetary discs, it is necessary to use spectroscopy. For this reason, there is currently significant interest in developing high contrast integral field spectroscopy systems, and work is underway to assess which is the most promising approach. Some approaches include the use of image slicers (e.g. VLT-SINFONI/ERIS), others are using lenslet arrays (e.g. Gemini-GPI, VLT-SPHERE). An alternative approach is to use a fibre-coupled microlens array, and since the IFU is to be placed behind an extreme AO system it becomes feasible to efficiently use single mode fibres which further increase the contrast of the system through their mode filtering properties, and also facilitate high resolution spectroscopy without inducing modal noise.

The first single-mode IFU to be developed for exoplanet science applications was the single-mode IFU for the RHEA spectrograph at SUBARU - a high resolution, single mode fibre fed spectrograph designed to operate between 590 nm and 810 nm, with a spectral resolution of ~60,000 [84]. The single mode IFU, shown in Figure 23, was constructed by placing nine single mode fibres into glass ferules, which were then actively aligned and glued to a glass prism. This prism could then be slid against another prim which had the microlens array attached to it, thus controlling the distance between the microlens array and the fibre facets.
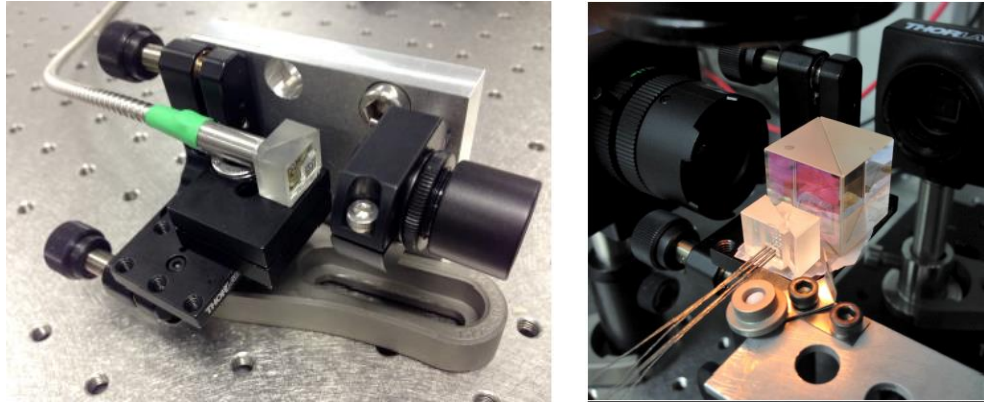
Figure 23: (Left) Photograph of the first single mode IFU to be developed for exoplanet science applications. The armoured cable contains nine single mode fibres which are attached to an alignment mount. (Right) Photograph of the single-mode IFU during alignment and construction. Taken and adapted from [84].

The proof-of-concept work that has been conducted on the single-mode IFU for RHEA is exciting, but the specific technical approaches have significant limitations. As shown in Figure 24, the precision with which the fibres can be aligned and glued is rather limited, even for the relatively low number of fibres used in this initial prototype. Clearly, if the single-mode IFU concept is to be extended to IFUs containing much larger numbers of fibres (e.g. a few 100 is not an unreasonable target [75]), a new approach is required.
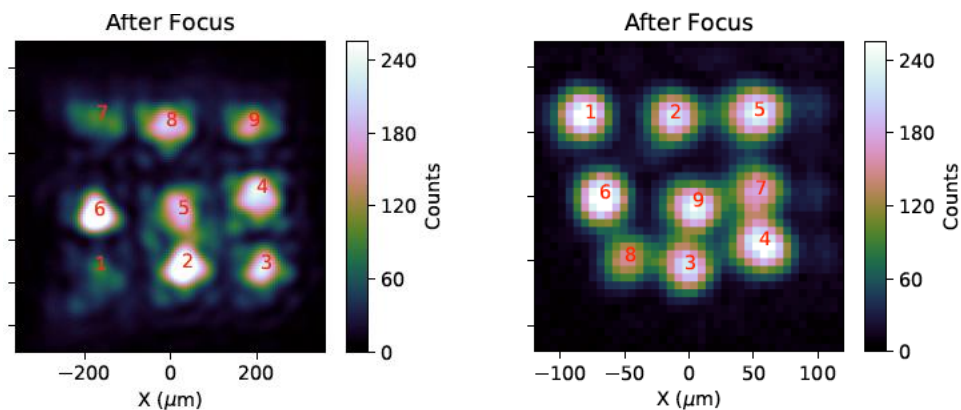

Figure 24: Images of two different 3×3 single mode fibre arrays obtained through the single mode IFU developed for RHEA itself using back illumination. Taken and adapted from [84].

One potential approach to manufacture high performance single mode IFUs with hundreds of fibres is to use ultrafast laser writing in combination with selective chemical etching [85]. This technique facilitates the precise sculpting of various dielectric materials, but particularly fused silica. As such, it would allow the development of a single monolithic component that contains both the microlens array on one side of the component, but crucially also an array of holes on the other side of the component that can act as passive alignment features for optical fibres. This approach has already been used at Heriot-Watt to manufacture prototype fibre focusing packages for the Multi-Object Optical and Near-infrared Spectrograph (MOONS) [86], and a schematic of one of these collimation packages is shown in Figure 25, while Figure 26 presents images of a fibre coupled microlens prototype and its operation for collimation applications. It is not unreasonable to expect that this approach could be extended to multi-fibre IFU components, and there has already been some work to move towards multi-fibre systems at Heriot-Watt, as shown in Figure 27.
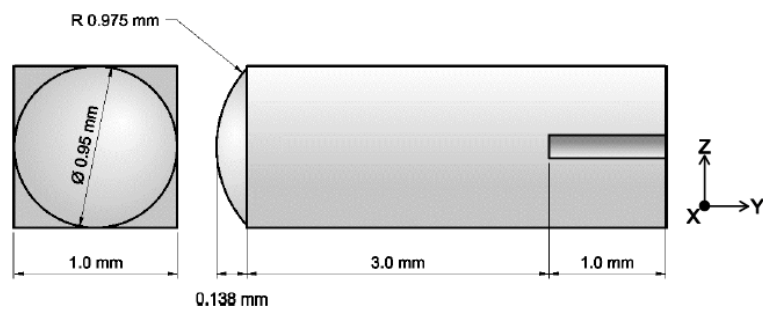

Figure 25: Schematic of one of the MOONS fibre-focusing packages that was targeted for fabrication at Heriot-Watt using ultrafast laser inscription in combination with selective chemical etching. Taken and adapted from [87].
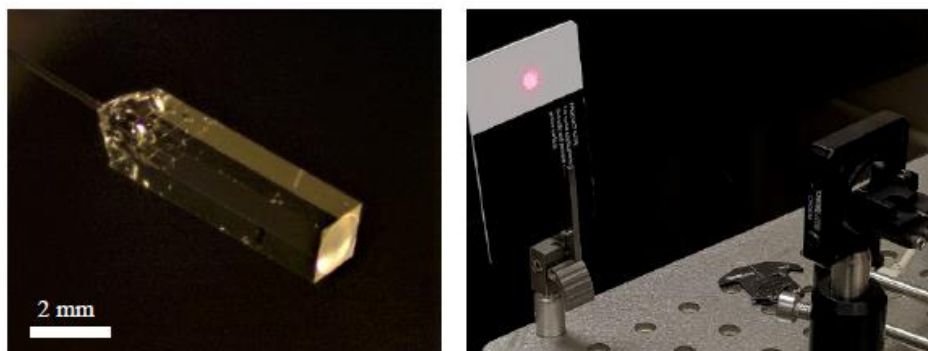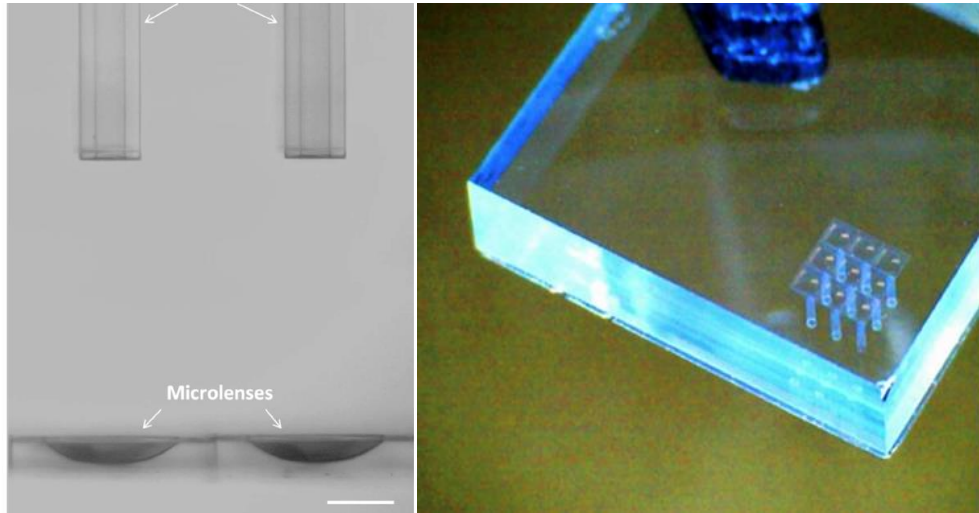

Figure 26: (Left) Photograph of a single fibre coupled lens with a single mode fibre glued into the passive alignment slot on the opposite side of the component from the lens. (Right) Demonstration of low scattering, high precision collimation of the light emitted from the multimode fibre.

Figure 27: (Left) Optical micrograph of two microlenses with passive alignment slots for optical fibres. (Right) Optical micrograph of a 3 × 3 array of microlenses with passive alignment features for optical fibres. Taken and adapted from [88].

An alternative and equally promising approach to manufacturing high spaxel count single mode IFUs is to use a single multicore fibre that contains hundreds of single mode cores. In this case, the relative positioning of the MCF cores can be controlled to an extremely high level due to the nature of the stack-and-draw fibre fabrication process. Using this MCF-based approach, the challenges then become twofold:

- a solution is required to precisely couple the MCF to a microlens array to enable its efficient use at the focal plane of the telescope.

- a solution is required to enable the reformatting of the light emitted from the MCF at the spectrograph, such that the individual spectra from each core of the MCF do not overlap on the detector.

One solution to the first challenge is to use three-dimensional laser nanolithography. In this technique, which can be performed using either in-house research systems, or off-the-shelf commercial systems such as the Nanoscribe system (www.nanoscribe.com), a focused femtosecond laser beam is used locally polymerise a monomer material. After laser writing, the unexposed monomer can be removed using a "development" stage

involving washing the component in a suitable solvent that does not dissolve the polymerised material. The 3D nanolithography approach has many advantages:

- the lenses can be precisely aligned to the cores of the MCF.

- the profile of the lenses can be controlled down to the few nm level.

- the technique is extremely flexible due to its direct-write nature, and the properties of the microlens array can be readily adapted to optimise the system during the IFU development.

As shown in Figure 28, significant progress has been made in the manufacture of freeform microlenses onto multicore fibres, confirming the suitability of this technique for the development of single mode IFUs using MCFs.
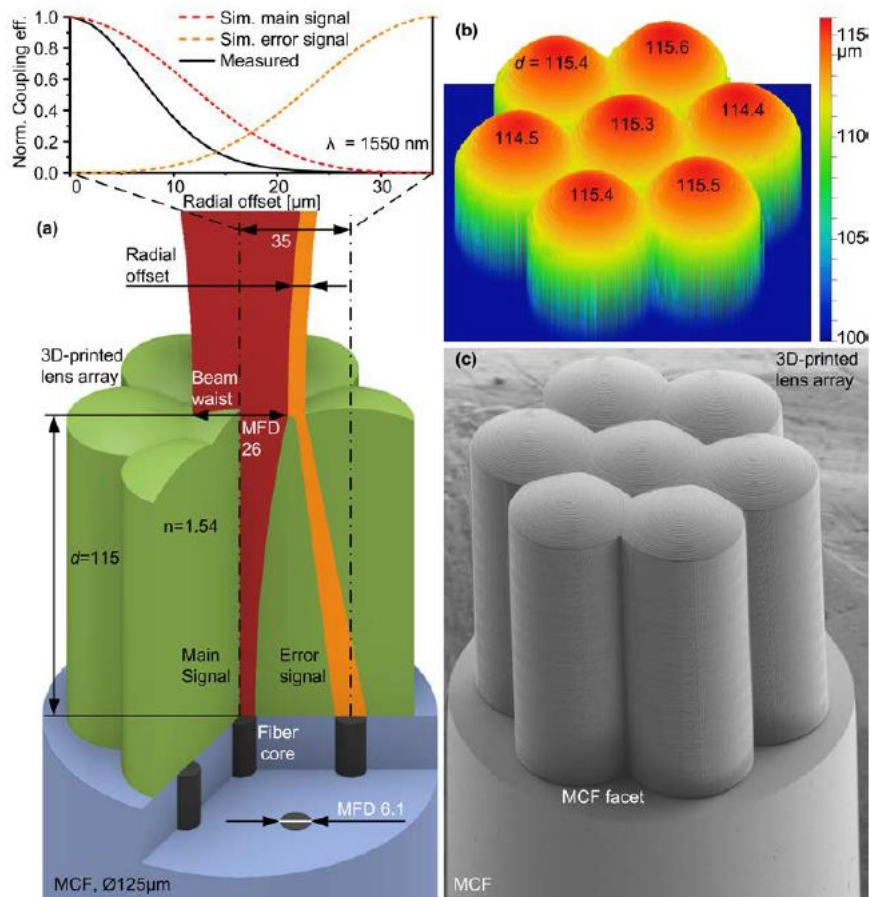
Figure 28: A freeform microlens array fabricated on the facet of a 7-core MCF. (a) Simulations of the microlens array and its operation in coupling light to different cores as a function of the beam offset. (b) Surface topography image of the microlens array. (c) Scanning electron microscope image of the microlens array. Reprinted with permission from [34] © The Optical Society.

Three-dimensional laser nanolithography also has the potential of providing an optical reformatting solution for the light emerging from the MCF cores at the spectrograph end of the MCF. In addition to being able to fabricate components such as microlenses, three-dimensional laser nanolithography can also be used to fabricate free-standing optical waveguides - a capability has become known as photonic wire bonding [89], Figure 29. One drawback of this technique is that since the photonic wirebonds are surrounded by air, the core-cladding index contrast is extremely high (~1.5). This in turn means that the waveguides have to be extremely small in cross section to maintain single mode guidance. For example, for single mode operation at 1,550 nm the waveguide radius must be less than ~550 nm, and for single mode operation at 1,000 nm the waveguide radius must be less than ~350 nm. This obviously makes the waveguides extremely fragile.
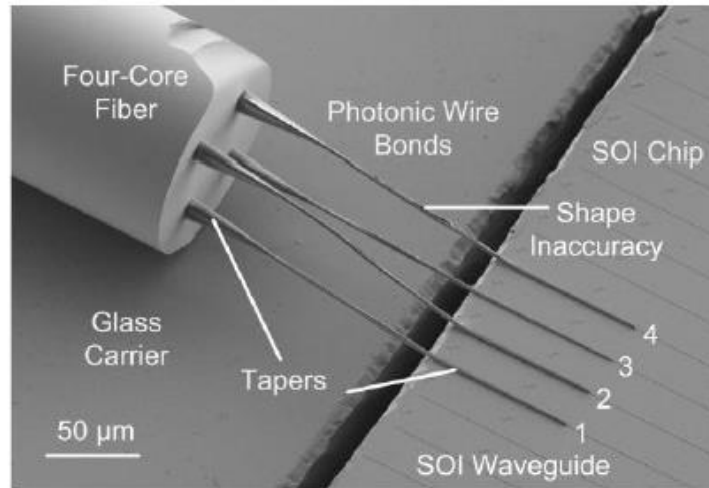
Figure 29: Scanning electron microscope image of photonic wire bonds created to reformat the light emerging from a 2 × 2 core MCF into a 1 × 4 linear array of optical waveguides. Taken and adapted from [89], © 2015 IEEE.

3.2 Aim of the study

The work described in the published paper which accompanies this chapter is concerned with developing a prototype MCF-based single mode IFU, a bespoke spectrograph based on stacked volume gratings, and testing the system on-sky with the CANARY AO system and the William Herschel Telescope in La Palma.

The MCF was designed to contain 73 cores that were single mode at wavelengths longer than 970 nm, and the spectrograph was designed to operate across the 1.0 μm to 1.6 μm band. The fibre link was manufactured by printing a 73 lens array onto one end of the MCF using a Nanoscribe system to provide the MCF-to-microlens array solution required for the telescope end of the MCF-based single mode IFU. To reformat the light emerging from the MCF at the spectrograph end of the MCF we used the refractive index modification capability of ULI to fabricate a three-dimensional optical waveguide component that reformats the modes of the MCF into an arrangement that allows the light to be dispersed without multiple spectra spatially overlapping on the detector. A custom chrome-on-silica mask was also fabricated using ULI in combination with selective chemical etching to block stray light at the output of the reformatting component. Although we were not in a position to conduct exoplanet studies using the MCIFU, we were able to conduct some basic proof-of-concept on-sky work at the WHT using CANARY, successfully demonstrating the acquisition of the spectrum of Vega. The spectral width of the measured telluric lines imprinted on the acquired spectra

confirm that the spectrograph is operating in a manner that is in agreement with the performance expected based on laboratory characterisation work. Based on these results, the collaboration has now been granted time to test the MCIFU system on MagAO-X, an extreme AO system at the Magellan Clay 6.5 m telescope at Las Campanas Observatory in Chile.

3.3   My contributions

This section explains what contributions were made by myself and my co-authors towards the work in the following paper. The overall project was co-lead by S. Y. Haffert (SYH) and R. J. Harris (RJH).

I used the refractive index modification capability of ULI to develop a custom waveguide component for reformatting the light emerging at the spectrograph end of the MCF in a manner that prevents spectra for different MCF cores spatially overlapping on the detector. The reformatter geometry was calculated by RJH. The MCF was manufactured by I. Gris-Sánchez. I also attached the chrome-on-silica mask made by C. A. Ross (CAR), used to block stray light from emerging from the reformatter into the spectrograph. I attached the MCF to the fibre support chip made by CAR which provided a larger surface for gluing to the reformatter. This required careful alignment while ensuring the angle between the two parts remained within a small tolerance. I characterised the throughput of the reformatter with and without the mask, before the addition of the microlens array. The authors affiliated to KIT made the microlens array.

The spectrograph was constructed by the authors affiliated to INAF, and SYH, RJH and I assisted them with the alignment of and integration into the telescope. We also worked together for the acquisition of the data on-sky. The paper was contributed to primarily by SYH and RJH, with my input concerning section 3, with assistance from A. Benoît.

Diffraction-limited integral-field spectroscopy for extreme adaptive optics systems with the multicore fiber-fed integral-field unit

Sebastiaan Y. Haffert[a,b,*,†,‡] Robert J. Harris,[c,d,†] Alessio Zanutta,[e] Fraser A. Pike,[f] Andrea Bianco,[e] Eduardo Redaelli,[e] Aurélien Benoît,[f] David G. MacLachlan,[f] Calum A. Ross,[f] Itandehui Gris-Sánchez,[g,h] Mareike D. Trappen,[i,j] Yilin Xu,[i,j] Matthias Blaicher,[i,j] Pascal Maier,[i,j] Giulio Riva,[e] Baptiste Sinquin,[k] Caroline Kulcsár,[k] Nazim Ali Bharmal,[l] Eric Gendron,[m] Lazar Staykov,[l] Tim J. Morris,[l] Santiago Barboza,[d] Norbert Muench,[d] Lisa Bardou,[l] Léonard Prengère,[k] Henri-François Raynaud,[k] Phillip Hottinger,[c] Theodoros Anagnos,[c,n] James Osborn,[l] Christian Koos,[i,j] Robert R. Thomson,[f] Tim A. Birks,[g] Ignas A. G. Snellen,[a] and Christoph U. Keller[a]

[a]Leiden University, Leiden Observatory, RA Leiden, The Netherlands
[b]Unversity of Arizona, Steward Observatory, Tucson, Arizona, United States
[c]Zentrum für Astronomie der Universität Heidelberg, Landessternwarte Königstuhl, Königstuhl, Heidelberg, Germany
[d]Max-Planck-Institute for Astronomy, Königstuhl, Heidelberg, Germany
[e]INAF—Osservatorio Astronomico di Brera, Merate (LC), Italy
[f]Heriot-Watt University, SUPA, Institute of Photonics and Quantum Sciences, Edinburgh, United Kingdom
[g]University of Bath, Department of Physics, Claverton Down, Bath, United Kingdom
[h]Universitat Politècnica de València, ITEAM Research Institute, Valencia, Spain
[i]Institute of Microstructure Technology, Karlsruhe Institute of Technology, Eggenstein-Leopoldshafen, Germany
[j]Institute of Photonics and Quantum Electronics (IPQ), Karlsruhe Institute of Technology (KIT), Karlsruhe, Germany
[k]Université Paris-Saclay, Institut d'Optique Graduate School, CNRS, Laboratoire Charles Fabry, Palaiseau, France
[l]Durham University, Department of Physics, Durham, United Kingdom
[m]Université PSL, CNRS, Sorbonne Université, Université de Paris, LESIA, Observatoire de Paris, Meudon, France
[n]Macquarie University, MQ Photonics Research Centre, Department of Physics and Astronomy, Australia

Abstract. Direct imaging instruments have the spatial resolution to resolve exoplanets from their host star. This enables direct characterization of the exoplanets atmosphere, but most direct imaging instruments do not have spectrographs with high enough resolving power for detailed atmospheric characterization. We investigate the use of a single-mode diffraction-limited integral-field unit that is compact and easy to integrate into current and future direct imaging instruments for exoplanet characterization. This achieved by making use of recent progress in photonic manufacturing to create a single-mode fiber-fed image reformatter. The fiber link is created with three-dimensional printed lenses on top of a single-mode multicore fiber that feeds an ultrafast laser inscribed photonic chip that reformats the fiber into a pseudoslit. We then couple it to a first-order spectrograph with a triple stacked volume phase holographic grating for a high efficiency over a large bandwidth. The prototype system has had a successful first-light observing run at the 4.2-m William Herschel Telescope. The measured on-sky resolving power is between

J. Astron. Telesc. Instrum. Syst.   045007-1   Oct–Dec 2020 • Vol. 6(4)

63

2500 and 3000, depending on the wavelength. With our observations, we show that single-mode integral-field spectroscopy is a viable option for current and future exoplanet imaging instruments. © *2020 Society of Photo-Optical Instrumentation Engineers (SPIE)* [DOI: 10.1117/1 .JATIS.6.4.045007]

1 Introduction

Exoplanet characterization often makes use of spatially unresolved spectroscopy of transiting planets. During the transit, light from the host star passes through the planet's atmosphere and leaves imprints in the starlight, which can then be analyzed to characterize the planet. This has lead to remarkable characterization of a wide variety of exoplanets.[1–3] The same technique has been applied to measure the direct emission from the planet, either thermal emission or optical reflected starlight, itself instead of the indirect signatures in the starlight.[4–6] These are very challenging observations, but they are within the current limits of technology for hot Jupiters. The main limiting factor for the detection of fainter exoplanets in unresolved spectroscopy is the overwhelming amount of starlight contaminating the planet signal, which has to be removed in postprocessing by complex time-series filtering algorithms.

Direct imaging instruments, such as SPHERE,[7] GPI,[8] or SCExAO,[9] are built to spatially resolve planets on large enough orbit from their host stars and often employ extreme adaptive optics (ExAO) systems and advanced coronagraphs. By employing ExAO, the influence of the star is greatly reduced by spatially resolving the planet, allowing for easier characterization of the planet. The coronagraph is then used in conjunction with an ExAO system to suppress the starlight, to enhance the contrast between the star and planet even further. After employing all these optical techniques, there is still residual starlight that leaks through the system due to imperfect adaptive optics (AO) correction and residual phase aberrations that create speckles which can appear as planets. Image processing techniques are necessary to remove these residual speckles to recover the planet signal.

While several giant planets have been directly imaged and spectroscopically characterized,[10–13] the number of directly imaged planets has been limited so far. The current generation of high-contrast imagers is sensitive to the small population of young self-luminous exoplanets on wide orbits.[14,15] More planets could be directly imaged if the sensitivity close to the star is improved. Most of the current direct imaging instruments are limited at angular separations smaller than $10\lambda/D$ (0.4 in. at the VLT in H-band)[16] by quasistatic-speckles, which are slowly evolving speckles. Postprocessing algorithms that depend on spatial diversity, such as angular differential imaging (ADI),[17] are not able to remove the quasistatic speckles (QSS) due to the limited spatial diversity at small angles.

The combination of high-contrast imaging with high-resolution spectroscopy can resolve the issues that both techniques face. The effective resolving power on which the QSS change is mainly dominated by the scaling of the PSF with wavelength. This occurs on a resolving power of $R_{QSS} = \Delta\theta/(\lambda/D)$, where $\Delta\theta$ is the angular separation, λ is the central wavelength of observation, and D is the telescope diameter.[18] Observing speckles at 1 arcsec with an 8-m telescope requires a resolving power $R_{QSS} \approx 40$. High-resolution spectroscopy can remove the QSS efficiently if the spectral features of interest are narrower than the width corresponding to the effective resolution of the QSS. This usually holds for atomic and molecular spectral lines, which have an intrinsic resolving power between 100,000 and 200,000. Because these features are so narrow, most spectrographs dilute them to the spectrographs intrinsic resolving power. This sets the requirement that the spectrographs resolving power needs to be much larger than the effective resolving power of the speckles ($R \gg R_{QSS}$), which happens roughly around $R \approx 1000$ and anything above this resolving power is what we consider high-resolution spectroscopy in

this work. The combination of high-contrast imaging and high-resolution spectroscopy has been proposed several times already,[19–23] and only recently projects started to add this capability to high-contrast imaging instruments.[24–26]

While the high-contrast imaging instruments are lacking high-spectral resolution capabilities, there are several AO-fed medium- to high-resolution spectrographs (MUSE, SINFONI, OSIRIS, CRIRES). These instruments have been successfully used in the past years to characterize exoplanet atmospheres. The infrared observations of β Pictoris b[27,28] and HR8799[29–32] were used to detect the presence of several molecules, including water. Due to the high resolving power, CRIRES[27] were able to detect a rotational broadening of β Pictoris b. In the visible part of the spectrum, MUSE was used to characterize the Hα emission of the protoplanet PDS70 b,[12,13,33] and due to the high sensitivity, a second planet was found in the system.[34] The success of these observations shows that it will be worthwhile to add higher resolution integral-field spectroscopy to the current and next generation of high-contrast imagers.

In this work, we take advantage of several astrophotonics technologies developed in recent years[35–37] to create a large core count single-mode (SM) photonic reformatter. With additive manufacturing,[38] a microlens array (MLA) is three-dimensional (3D) printed on top of the fiber face[37] to efficiently feed the individual cores. An integrated photonic chip is used to rearrange the two-dimensional geometry of the multicore fiber (MCF) output into a pseudoslit that can be dispersed.[39] Because the fiber is single-moded, the spectrograph back end can be kept small. The proposed fiber link can be easily used to add higher resolution spectroscopic capabilities to current-generation ExAO systems as an upgrade.[40]

The spectrograph in this work uses an MCF with 73 cores and has a bandwidth ranging from 1 to 1.6 μm which was set by the properties of the available fiber (lower wavelength limit) and the available detector (upper wavelength limit). This spectral range contains interesting spectral features from molecules, such as methane, carbon monoxide, and water and accretion-driven emission lines from hydrogen and helium. The dispersing element of the multicore fiberfed integral field unit (MCIFU) is a custom triple stacked volume phase holographic grating (VPHG) that disperses the light into three orders with higher efficiency compared with conventional transmission gratings.[41] A schematic of the spectrograph is shown in Fig. 1. The prototype MCIFU was designed and built during the first half of 2019 and had its first light at the 4.2-m William Herschel Telescope (WHT) on La Palma behind the CANARY AO system[42] in July 2019.

In Sec. 2, we give a short overview of different image reformatting methods and discuss their advantages and disadvantages for high-contrast imaging. In Sec. 3, we describe the design, manufacturing, and characterization of the fiber link, which includes the 3D nanoprinted
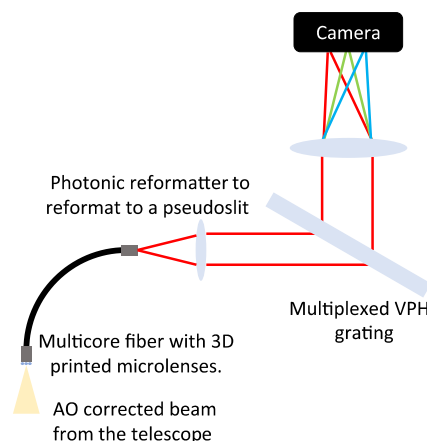
Fig. 1 An overview of the MCIFU. The telescope beam is imaged onto an MLA that is written on top of an MCF. The output of the MCF is rearranged into a pseudoslit by the photonic reformatter to make it dispersable. And finally, a triple multiplexed grating is used to disperse a broad wavelength range into three orders at a resolving power higher than $R = 5000$. The spectrograph itself is used in a first-order manner, where a lens is used to collimate the light onto a grating and a second lens is used to image the spectrograph focal plane.

MLA, the integrated photonic chip, and the fiber protection packaging. Section 4 describes the design and manufacturing of the custom VPHG, followed by the optomechanical design and characterization of the spectrograph with the VPHG in Sec. 5. Section 6 shows the first light results that were achieved with CANARY at the WHT. In Sec. 7, we discuss how to improve the current instrument for future use, after which the paper is summarized and concluded in Sec. 8.

2 Comparison of Image Reformatter Concepts for High-Contrast Imaging

An image reformatter is an optical component that rearranges an input focal plane into something that can be dispersed by a spectograph without losing spatial information. There are several options to achieve this: image slicers, microlenses, or fiber-fed spectrographs.

2.1 *Image Slicers*

An image slicer uses several reflective elements to reformat the field into a series of minislits. The image slicer creates the most efficient packing onto the detector, allowing for the most information to be recorded out of all techniques. But image slicers suffer from spatial–spectral crosstalk because adjacent spatial pixels along each slit are not separated on the detector. Another down-side is that the shape of the line spread function (LSF) changes depending on the the minislit illumination, which can occur, for example, due a slight tip or tilt of the input beam.[43] If high resolution spectroscopy (HRS) is needed to gain a large amount of contrast in postprocessing to characterize the planets, it is necessary to have a stable LSF because the HRS technique effectively searches for LSF variations across the field. If the contrast ratio that has to be bridged with respect to the local stellar halo is not very large (10^1 to 10^3), image slicers may be a good choice as previous observations have shown.[34,44]

2.2 *Microlens Arrays*

MLA-based integral field units (IFUs) use an MLA in the focal plane to sample the field. The MLA-based IFU is the current choice for spectroscopy on ExAO systems[7,45,46] and is even the standard observing mode for GPI.[8] An MLA IFU is easy to implement and is efficient when few spectral samples are required for large fields.[18] Another added benefit is that there are several ways to reduce the cross-talk between spatial-pixels by adding pinhole masks behind the MLA or aperture masks inside the spectrograph.[18] The reduced cross-talk allows the MLA-based IFUs to reach very deep contrast ratios of 10^4 to 10^6.[7,47] The drawback of the MLA IFUs is that it is not possible to measure many spectral resolving elements per spatial pixel (spaxel). Due to diffraction of the microlenses, the spot size is λF_{mla}, where λ is the wavelength and F_{mla} is the focal ratio of the microlens. Each spot requires an area of $\lambda^2 F_{\mathrm{mla}}^2$, while the total available area for each spaxel is the area of a single microlens, D_{mla}^2. That means that the maximum number of independent spectral elements is

$$N_\lambda = \frac{D_{\mathrm{mla}}^2}{\lambda^2 F_{\mathrm{mla}}^2}.$$ (1)

The relative bandwidth of the spectrograph is equal to the number of spaxels divided by the resolving power, $R = \lambda/\delta\lambda$, of the spectrograph,

$$\frac{\Delta\lambda}{\lambda} = \frac{N_\lambda}{\eta R} = \frac{D_{\mathrm{mla}}^2}{\eta R \lambda^2 F_{\mathrm{mla}}^2},$$ (2)

where $\Delta\lambda$ is the spectrograph bandwidth and η is the detector filling efficiency. The usual range of η is between $1/2$ and $2/3$ to ensure either a separation of 1 or 2 resolving elements between the spectra, respectively. The equation as shown in this section holds for MLA-based IFUs with many spaxels where the spectra of the spaxels will overlap if the size of each spectrum becomes

to large. This is the case for most MLA IFUs in high-contrast imaging, which generally have several hundred lenses across the diameter of the field of view. If a smaller array is used, such as a 3×3 MLA, then the array can be rotated to create spectra without overlap and the derived equation does not hold.

The typical microlens diameter is on the order of 300 μm and for the near-infrared (NIR) a central wavelength of 1.4 μm is reasonable. If the microlenses have a focal ratio of 5, the total bandwidth that can be observed at a resolving power of 10,000 with a single exposure is 16%. The bandwidth reduces to 8% if the detector separation is included. For high-resolution spectroscopy ($R = 100,000$), the bandwidth becomes a factor 10 even smaller. The single-shot bandwidth is a crucial parameter for the HRS technique because the signal-to-noise ratio (SNR) of the template matching is proportional to the bandwidth and the integration time, SNR $\propto \sqrt{\Delta\lambda\Delta t}$.[19,22] If the single-shot bandwidth is not high enough, conventional imaging techniques, such as ADI, may be more efficient for exoplanet imaging.[48] The MLA approach would be very suitable to target a small bandwidth around emission lines, such as Hα, at high-resolution to search for protoplanets.

2.3 Fiber-Based IFUs

A field can be reformatted by feeding each spaxel into a fiber. A fiber bundle has the most flexibility of all reformatting techniques, and the input and output can be rearranged completely independent from each other. The fiber-based IFU was therefore also the first IFU concept to be used on-sky.[49] Most fiber-based IFUs until now have used multimode fiber (MMF). These fibers can capture all light due to their large core but have a low fill fraction due to their large cladding diameters. This problem has been reduced by feeding the fibers with a MLA to increase the field.[50] The past few years have shown that the mode filtering capabilities of single-mode fibers (SMFs) can be used to create coronagraphs with smaller inner-working angles or higher throughput.[51–54]

In addition, SMFs can reject random speckles from the ExAO system to increase contrast,[51] which has been used before in the interferometry community to make it easier to interfere different beams.[55,56] Because SMFs only propagate an SM, the LSF is also very stable, which will make it easier to calibrate the spectra. SM spectroscopy is currently pursued in the radial velocity field,[57] because the LSF from multimode fibers is not stable enough.[58] And as a final benefit because SMFs only allow the propagation of an SM, any incoherent source that consists of many modes will be attenuated.[59] This property is very desirable especially in the infrared where the thermal background from the sky is high and limits the SNR of most observations. Therefore, an SMF bundle provides a significant amount of benefits over other manners of image slicing, making it a very attractive option for high-resolution broadband integral-field spectroscopy. It is difficult to quantify the gain of an SMF IFU over other methods without complete end-to-end simulations, which include complete modeling of the instrument, calibration, and observing modes. A downside of SMFs is that the mode filtering capability is restricted to focal plane samplings of $1\lambda/D$ per spaxel or larger. If the spatial sample density is increased, the mode filtering becomes less effective, which removes the main benefit of the SMF. From this, it follows that an optimally designed SM IFU will most likely not Nyquist sample the focal plane, which will remove the ability to use postprocessing techniques, such as ADI. But with the addition of high-resolution spectroscopy, it is possible to apply postprocessing techniques, such as molecule mapping[28] or high-resolution spectral differential imaging,[34] to discover and characterize exoplanets.

2.4 MCIFU Reformatter

To reach a high field filling fraction, the SMFs have to be fed with microlenses.[52,60] SMFs have very strict requirements on the alignment of the fibers for efficient injection,[61] even more if they need to be combined with coronagraphy.[62] Currently, the only SMFs-fed IFU is RHEA,[63] which uses a bundle of SMFs that are fed by a bulk MLA. Accurate alignment of the SMF bundle behind the MLA is very difficult with typical depths of focus of 10 to 20 μm and lateral alignment tolerances $\leq$1 μm.[24] And even in case that the individual fibers would be aligned for high injection efficiency, getting the output of the fibers aligned in the same plane of focus for the

67

spectrograph is still difficult.[24] Both issues can be solved using MCFs, which contain several independent SM cores inside a single fiber. This ensures that the fibers are in the same input and output planes. But because of the small size of the MCFs, it is difficult to feed them with a bulk MLA and reach the required alignment accuracy. We will use *in-situ* 3D printing of the MLA directly on top of the fiber face, which will allow for much more freedom. However, due to fixed core spacing, it is difficult to disperse the output over a broad bandwidth if there are many cores.[64] The pitch constraint is similar to the constraint of microlens-based IFUs.[18,43]

3 Single-Mode Multicore Fiber Link

The fiber link allows the point spread function (PSF) from the AO system to be coupled to the spectrograph. A description of all the different elements of the MCIFU is shown in Fig. 2. Figures 2(a) and 2(b) show a schematic and photograph of the full MCIFU, with the five main components: (c) the MLA, (d) the MCF, (e) the MCF glued inside a custom V-groove, (f-g) the reformatter, and (h) an ultrafast laser fabricated mask to block unguided light in the reformatter. Finally, Figs. 2(f) and 2(g) show a schematic representation of the reformatter with the color scheme to distinguish each row of waveguides.

The fiber link was assembled by first manufacturing and connectorizing the MCF and chip, then aligning and gluing to the reformatter and mask which were manufactured using ultrafast laser inscription (ULI). This was then packaged using off-the-shelf and 3D printed components and finally the microlenses were printed on the MCF which was secured in an FC-PC connector. The following sections are arranged in the order of manufacture.

3.1 Fiber

Due to cost and time constraints, we used an already available MCF that had been manufactured for a different project. Therefore, the specifications and the geometry of the fiber were fixed. The MCF is comprised of 73 step-index Ge-doped cores manufactured using the common stack-and-draw fiber fabrication technique [Fig. 2(d)]. The MCF has a outer cladding diameter of 560 μm.
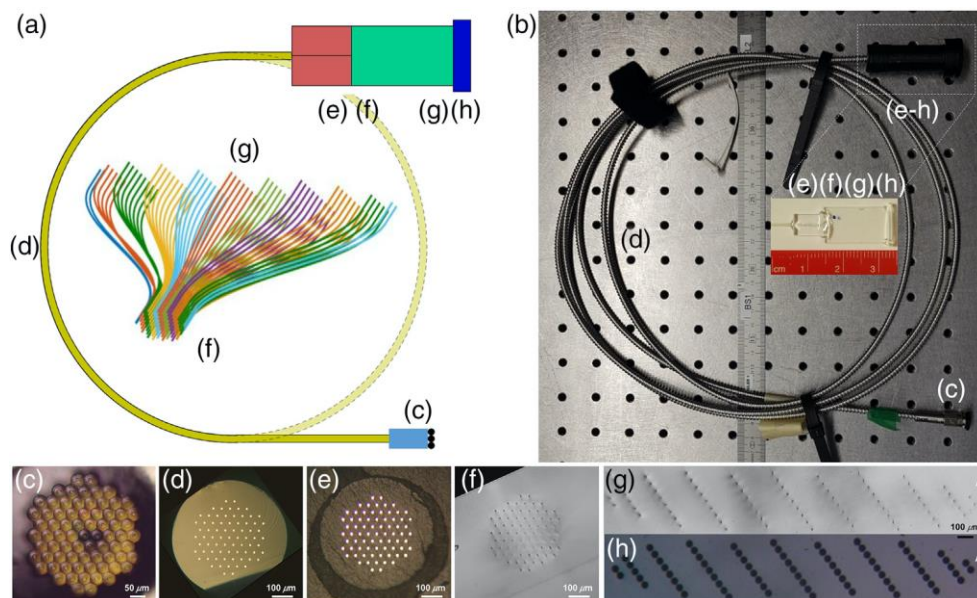
Fig. 2 The MCIFU fiber link, with important sections shown. (a) A schematic representation of the fiber link, (b) photograph of the complete packaged fiber link comprising all the elements from the MLA, (c) the 3D printed microlenses, (d) the bare fiber, (e) the bare fiber in a v-groove, (f) the input of the chip reformatter. (g) The output of the reformatter. (h) The output mask. The white arrow in (g) and (h) indicates the dispersion direction. Inset in (b): Scale picture of the full reformatter.

68

Each individual core has a numerical aperture (NA) of 0.14 and a diameter of ~5.3 μm, which results in a mode field diameter (MFD) of ~8.2 μm at a wavelength of 1.4 μm. The SM cutoff of each core is ~970 nm. The cores are spaced by 41 μm, this means they are separated by approximately five times the MFD, ensuring negligible cross coupling between the cores.

3.2 Reformatter and Mask

At the spectrograph end, the MCF is directly butt-coupled to an ULI-fabricated 3D waveguide reformatter, which spatially reformats the MCF cores into a suitable arrangement, such that the dispersed spectra from each waveguide do not overlap with each other on the detector. To minimize undesirable effects due to scattered/unguided light not contained within the reformatter cores, a mask was fabricated using femtosecond laser inscribed chemical etching (FLICE). This mask consisted of a fused silica fixture with holes precisely positioned to align with the output waveguides. Measurements taken after coating the silica with a layer of chromium show that the chromium mask is blocking the stray light by a factor of 10 to 100 (see Fig. 3).

To separate the spectra from each MCF core and avoid any overlap after dispersion, the quasi-hexagonal MCF shape must be reformatted [Fig. 2(g)]. Existing reformatters have generally chosen a linear pseudoslit output pattern.[36,39,65] However, for the MCIFU, we chose a staggered slit. This has the advantage of increasing the spacing between adjacent cores, reducing cross coupling, while also reducing the translation of the waveguides within the glass. The reformatted pattern was created to give a spacing of 30 μm between the individual spectral traces of each core on the spectrograph. To do so, ULI was used to inscribe a reformatter in a $20 \times 10 \times 1$ mm borosilicate glass substrate (Eagle XG).[66] The inscription laser source is a MenloSystems BlueCut fiber laser emitting at 1030-nm a 500-kHz train of 350-fs pulses which are focused within the substrate with a 0.55-NA aspheric lens. Each waveguide was inscribed using a substrate translation speed of 8 mm/s and 19 scans of the laser focus with an interscan separation of 0.2 μm. This resulted in highly symmetric SM waveguides with an NA of $\approx$0.11 and MFD of $\approx$7.3 μm at the $1/e^2$ beam size of a Gaussian beam at 1310 nm. ULI has a limit in the refractive index contrast that can be achieved, which resulted in a lower NA of the ULI waveguides as compared with the NA of the MCF. This will lead to coupling losses at the interface of the reformatter and the MCF that represents a significant part of the global insertion losses of the reformatter. A custom MCF with an NA that matches the ULI specification would allow for a higher throughput. The pulse energy providing the highest throughput waveguides at the initial depth of 470 μm was 128 nJ and adjusted to 105 nJ for depths lower than 130 μm to compensate for spherical aberrations on the beam.

The waveguides were characterized by two different laser sources: a 1310-nm laser and a supercontinuum with an 1100-nm bandpass filter [with a full-width at half-maximum (FWHM) of 10 nm]. The two different sources were coupled into an SMF-28 optical fiber and characterization performed by butt-coupling the SMF-28 output to a single core of the MCF. The MCF was then butt-coupled to each individual waveguide of the reformatter with the aid of an index
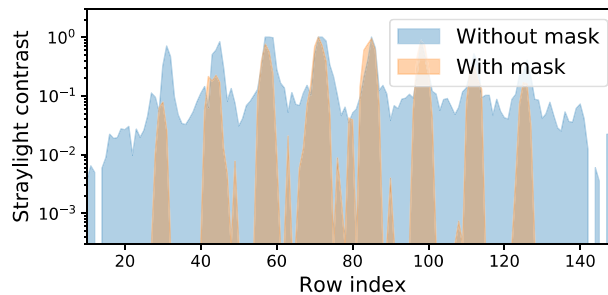
Fig. 3 A slice along one of the rows of the reformatter showing the scattered light with and without the chromium mask. Here, the input MLA is overfilled, specifically to simulate background light in astronomical observations. The blue shaded area shows where the scattered light is still detectable between the waveguides, the red shaded area shows the stray light with the mask. The row index is the pixel index along the extracted slice.

matching fluid. By this way, we ensure to work with the exact MFD to characterize the waveguides. SM behavior of the waveguides in the J-band between 1.1 and 1.3 μm was observed. The throughput was characterized with the ultrastable laser at 1310 nm. With this optimized set of parameters, the throughput of the straight waveguides can reach 67%, corresponding to a global insertion losses of 1.7 dB. To create the reformatter, an investigation was performed to optimize bend radius and minimize transmission losses. The bending losses are negligible for a bend radius in the propagation direction of >15 mm, deviating by a distance of 1 mm (corresponding to the extreme edge waveguides), and we have chosen a bend radius of 18 mm.

The final reformatter was permanently glued to the MCF using a UV curing adhesive. To provide a larger gluing surface to bond the fiber to the reformatter, a fiber support chip was fabricated with a custom hollow-cylindrical V-groove to house the MCF. This was created by the process of FLICE, in an ($8 \times 6 \times 2$ mm) fused silica substrate.[67] The V-groove shape was defined by the process of ULI with 200-nJ pulses from the Bluecut fiber laser at a repetition rate of 250 kHz and a subsequent wet chemical etch in 8 mol.L^{-1} potassium hydroxide solution at 85 deg to remove the excess material.

Finally, a mask was developed to block stray and scattered light at the reformatter output while allowing the light from the individual waveguides to propagate as desired. The scattered light in the ULI glass substrate can present a significant challenge for astronomical instruments trying to overcome the high contrast between the observed star and the planet.[68] The mask [Fig. 2(h)] was created by the process of FLICE in a similar manner to the fiber support chip from a $2 \times 12 \times 2$ mm-fused silica substrate. The high precision stages enabled a rectangular slot to be created to snugly fit the reformatter within this mask, with 30 μm diameter through holes precisely passively aligned to the waveguide positions [Fig. 2(g)]. A 120-nm layer of chromium metal was deposited on the outer surface of the mask by electron-beam physical vapor deposition. This process creates an opaque component that removes the scattered light present in the glass between the waveguides. Figure 3 shows the removal of scattered light between the ULI waveguides without and with the opaque mask in blue and red, respectively. The scattered light was measured by taking a slice along one of the rows of the reformatter.

In Fig. 4, we present the end-to-end throughputs from the MCF to the mask, at 1310 nm, before the MLA was added. In Fig. 4, one can clearly see that the fiber link has lost a significant part of the throughput on the top/bottom edges of the reformatter. These losses come from a slight variation of the input waveguide positions of the reformatter [Fig. 2(f)] in comparison of the MCF, inducing mode-field diameter mismatching. The high sensitivity of the coupling losses between the MCF and the reformatter is highlighted for our final device by a slight misalignment that can change the throughput from 67% to lower than 5%.

The whole output device was then encased with a combination of off-the-shelf components and 3D printed parts, and the MLA was secured within an FC-PC connector to create a robust component for use at the telescope [Fig. 2(b)].
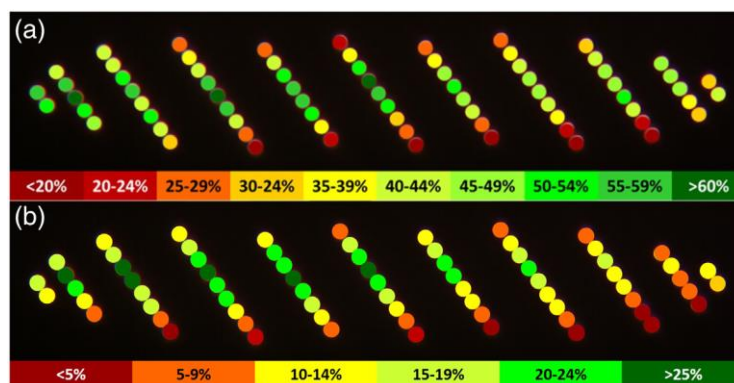
Fig. 4 Illustration of the measured monochromatic (1310 nm) throughput results for the fiber link. (a) The throughput for the 73 individual cores through the fiber, the reformattter and the chromium mask. (b) as for (a) but for the full fiber link, including the microlenses. The color bars represent the throughput ranges for each figure.

3.3 Microlens Array

The surface shape of the MLA was optimized for coupling efficiency using the physical optics propagation module in Zemax. To simulate the Airy pattern of a telescope, we used an unobstructed aperture with a diameter of 1 m. The beam was focused by a paraxial lens with a focal length that created a focal ratio of 22, allowing a $1.5\lambda/D$ sampling per microlens of the focal plane at 1.3 μm. The microlens surface was then modeled as a single lens with a hexagonal aperture made from IP-DIP.[69] We tried several freeform shapes to increase the coupling efficiency but found that there was very little improvement, less than a percent point, compared with purely spherical surfaces. Therefore, we chose a spherical surface for the final design. We found that a radius of curvature of 74.5 μm with a 205-μm height provided the highest wavelength averaged coupling efficiency of 67.5% to a single core of our MCF. Figure 5 shows the on-axis coupling efficiency as a function of the wavelength. The proposed microlens design has a theoretical wavelength-dependent throughput between 50% and 81%. The limiting factor in the throughput is the fraction of the Airy pattern that a single microlens captures. Due to scaling of the Airy pattern with wavelength, longer wavelengths will capture a smaller fraction of the PSF. The orange line in Fig. 5 shows the fraction of the transmitted flux for a microlens as a function of wavelength. It is clear that the coupling to the SMF cores is between 80% and 95% efficient across the spectrum, which shows that there will be little to gain from more complicated designs for on-axis objects.

The MLA was *in-situ* printed on the flat facet of the FC-PC connector in which the cleaved MCF was manually glued and then polished. The lenses were printed in a single block and in a single two-photon lithography step out of the commercial negative-tone photoresist IP-Dip.[70] The structures were defined by an in-house built lithography machine, equipped with a 780-nm femtosecond laser. An in-house developed machine software was used for high-precision alignment and writing with high shape fidelity. Illumination of the fiber back end with a red LED together with machine vision was used to detect all 73 cores of the MCF and align the individual lenslets to the cores. Therefore, the full 3D-model is generated only after core detection to be able to compensate any slight location and pitch variation of the individual cores of the MCF. The individual models of the lenslets are then merged and at places of overlap, due to the slight spatial variation in the MCF cores, the highest surface is chosen. Slight tilts of the fiber facet due to mounting are detected as well and the structures corrected accordingly. The writing distances between subsequent lines and layers, i.e., both hatching and slicing distance, were set to 100 nm. No antireflection (AR) coating was added to the microlenses. This adds some losses due to Fresnel reflection, which is roughly 5%.

3.4 Performance of the Fiber Link

With the whole system assembled and packaged, the individual cores were tested for throughput. This was again performed at 1310 nm to be consistent with earlier tests. The light sources were fed through an SMF and then to a collimating lens (Thorlabs AC254-200-C). The collimated
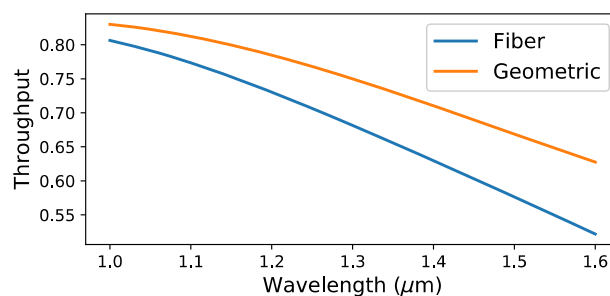
Fig. 5 The amount of on-axis light that couples into a single core of the MCF as function of wavelength within the spectrograph bandwidth. The fiber throughput is the amount that couples into a single core, while the microlens throughput is the amount of light that enters the microlens. With the MLA we can couple between 80% and 95% of the light that falls on a single microlens.

beam was stopped down by an aperture stop to simulate the same focal ratio of 22 beam that the foreoptics of the experiment with CANARY will supply to the microlenses. Finally, a lens (Thorlabs AC254-100-C) was used to focus the light onto the microlenses. To simulate the on-sky conditions, the input light was first optimized for position, focus, tip, and tilt using a central lens. This was optimized and checked at several points across the lens array and then used as the reference. Only from this point, the horizontal (x) and vertical (y) positions were changed, maintaining a global reference for all the microlenses. This means any deviation from perfect will reduce the throughput of the individual lenses. However, it better matches the expectations on sky conditions. This simple setup creates a diffraction-limited beam and shows the wavefront error-free throughput.

The recorded throughputs are shown in Fig. 4. This shows that the central cores performed best, with significant reduction at the edges. Causes and solutions are discussed in Sec. 7.

## 4 Triple Stacked Volume Phase Grating

The ultimate goal of the instrument is to have a spectral resolving power between 5000 and 10,000, which can be readily accessible with transmissive volume phase gratings (used in the first diffraction order with the present design). Despite this, even if VPHGs can be made with very high diffraction efficiency, the disadvantage of a classical, single first-order grating is that the light will be smeared out in a single spectrum, thus wasting usable portions of the detector. Moreover, for securing the large bandwidth at the target resolution, it is required to use a very wide sensor, which is very expensive and not readily available. A possible solution is to multiplex the VPHG in layers as reported in Ref. 41. In this way, each grating can diffract a different part of the wavelength range toward the same direction so the average efficiency is improved by a wide margin, by having more than one efficiency maximum. To separate the spectra on the detector plane, the gratings are rotated with respect to each other, with a designed angle set to have clearly separated spectra and output signals which are as horizontally dispersed as possible (see Fig. 6).

4.1 *Design*

Considering the working wavelength range for this application of 1000 to 1600 nm, the geometrical conditions have been chosen with the aim to obtain three first-order diffraction efficiency curves with maxima at around 1100, 1300, and 1500 nm, ensuring a high efficiency at each wavelength. The incidence angle defined in the spectrograph design is 21.5 deg. This angle is shared by the three dispersing layers and the grating line density has been chosen to match the Bragg condition at the central wavelength for each of the three gratings.
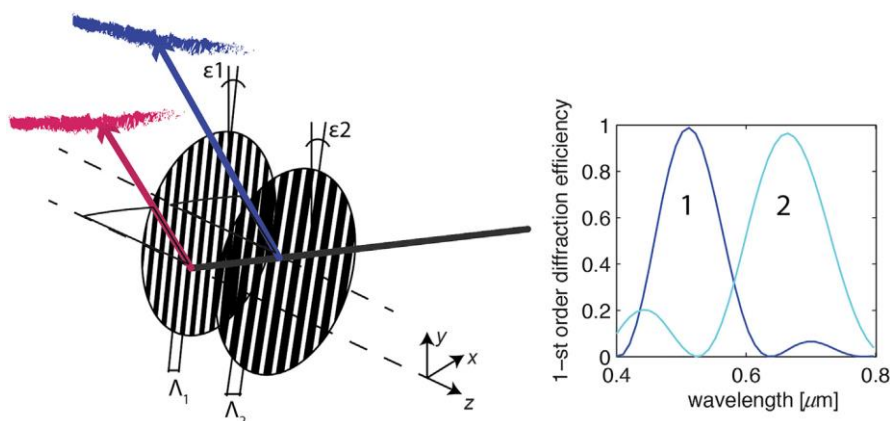
Fig. 6 Scheme of the spectral-multiplexing concept. For simplicity, a two-stacked VPHG is presented, each creating a separate spectrum which are shown in different colors. The inset shows the simulated diffraction efficiencies of the two layers for an example design.
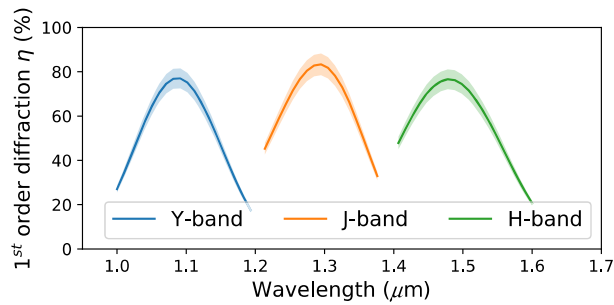
Fig. 7 Simulation of the combined diffraction efficiency of the multiplexed VPHG for an incidence angle of 21.5° for unpolarized light. The shaded area presents the minimum and maximum diffraction efficiency prediction for the manufacturing process. Material absorption and reflection losses have been estimated and taken into account.

Table 1 Main features selected for the three designed diffraction gratings.

Layer #	Central wavelength (nm)	Index modulation Δn	Layer thickness (μm)	Grating pitch (lines/mm)	ϵ rotational angle (°)
1	1100	0.022	28	668	−3
2	1300	0.020	34	565	0
3	1500	0.010	50	490	3

The efficiency and bandwidth of each single layer (and thus the refractive index modulation strength, Δn, of the grating and thickness of VPHGs, respectively) have been calculated and optimized by means of a rigorous coupled wave analysis-based script. The ad-hoc code takes into account the interaction between the diffractive layers and computes the final throughput of the multiplexed element, see Fig. 7. The losses due to reflection as well as those due to materials absorption and scattering have been considered in the simulations to have a reliable prediction of the efficiency curves. In Table 1, the final design parameters of the stacked optical element are reported.

4.2 *Manufacturing*

The choice of the materials with different thickness has been based on the Δn requirements along with the width of each first-order diffraction and the line density required for each grating. The three gratings have been produced using the Bayfol® HX material. This photopolymeric film has been chosen due to its ability to address precisely the required Δn values, simply selecting the proper writing conditions (e.g., laser power density).[71] Moreover, the solid layers can be used in a configuration that requires only one glass substrate in between the layers, resulting in a thinner diffractive element. Each VPHG layer composing the final device has been produced individually by means of the holographic setup based on a 532-nm diode-pumped solid-state laser. Every photopolymeric grating is supported by a BK7 round window (1 in.), the front and the back ones possess AR coating on the outer face (optimized from 1 to 1.6 μm at 21.5 deg).

After the characterization of each layer, they were coupled with index matching fluid (cedar oil) and aligned according to the tilt angles specified in the design phase. To hold and block firmly the three layers, an ad-hoc 3D-printed plastic (PLA) shell was used.
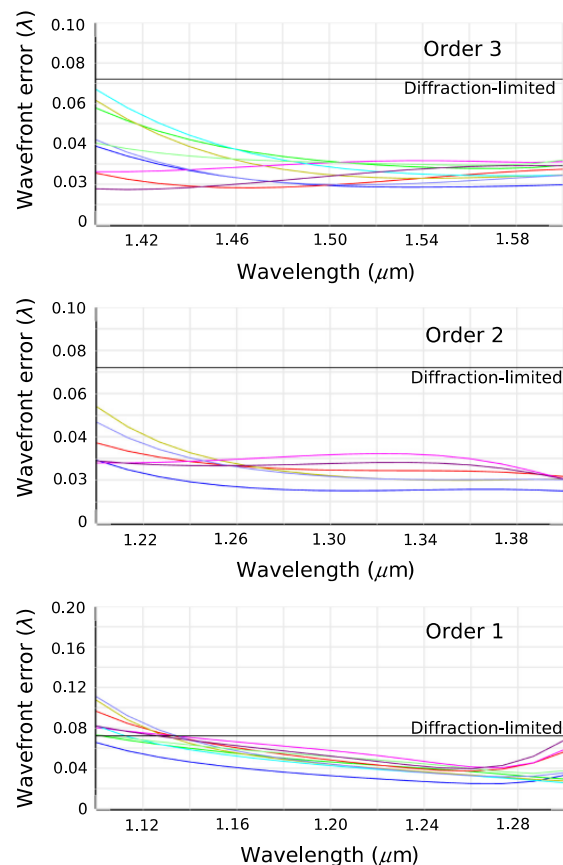
5 Spectrograph

5.1 *Optical Design*

The spectrograph was designed with off-the-shelf lenses. The output of the reformatter was estimated to have a focal ratio of 5, which was subsequently used as the input source for the

spectrograph design. The spectrograph design is a standard first-order design, with a collimator lens that creates the beam that will be dispersed by the grating, and a camera lens that focuses the spectra onto a camera. For the camera lens, we used an achromatic tube lens from Thorlabs, which has diffraction-limited performance over a large field of view and spectral bandwidth while also delivering a flat image plane. These properties make the tube lenses from Thorlabs ideal as camera lenses for integral-field spectrographs. From the available tube lenses, we found that the TTL200-S8 fitted within the requirements of the MCIFU.

The focal ratio of the waveguides ($\#F = 5$) together with the effective slit length of 2 mm required us to create a custom collimator. We used combinations of spherical singlets to create a "semicustom" collimator. The design procedure started with two off-the-shelf doublets. The internal interface of each of the doublets was set to flat (a radius of curvature of infinite). All four outer surfaces of these two doublets were optimized by minimized the angular root-mean square (rms). Then, the surfaces were iteratively replaced with the closest matching off-the-shelf singlet that was available from either Thorlabs or Edmund Optics and then the angular rms was minimized by reoptimizing the remaining surfaces. We repeated this procedure until we found a combination of singlets that had diffraction-limited performance over the full wavelength range and pseudoslit length of the reformatter. Even though the optical quality of this semicustom collimator was satisfying, not all optics were available with NIR optimized coatings. This resulted in a collimator with several uncoated optics that reduced the throughput. Figure 8 shows the total theoretical wavefront quality of the spectrograph design. Almost the full wavelength range is diffraction-limited, except for the small range of 1.0 to 1.03 μm which is nearly

Fig. 8 The wavefront quality of the spectrograph as function of wavelength for the three different orders that are made by the VPHG. The various colors represent a position along the pseudoslit and are the same pseudoslit position for each order. Here, we can see that the spectrograph design is diffraction-limited over almost the full spectral bandwidth. Only the blue part of the Y-band is slightly nondiffraction-limited, which will lower the effective resolving power.
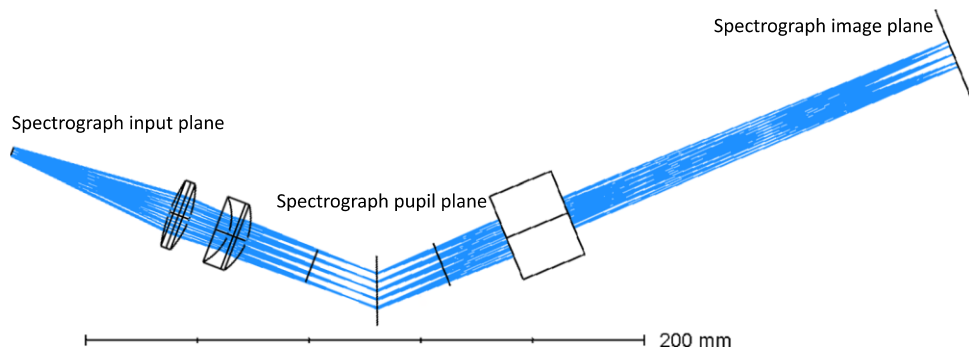
Fig. 9 The layout of the spectrograph with the different components of the spectrograph. The scale bar shows the small footprint of the optical path of the spectrograph, which is roughly 40 cm × 20 cm.

diffraction-limited. The final layout of the MCIFU spectrograph is shown in Fig. 9. The spectrograph could be kept small with a footprint of ~200 × 400 mm due to the SM input.

The collimator creates an 11-mm pupil diameter, with <0.5 mm of pupil wander as a function of position along the pseudoslit. The diffraction-limited resolving power of the spectrograph is $R = W\rho$, where W is the projected size of the pupil onto the grating and ρ is the line density of the grating. The theoretical maximum resolving power would then be ~8000, 6700, and 5800 for Y-band, J-band, and H-band, respectively. For best performance, the spectrograph has been designed to work with an output plane of 2048×2048 pixels. A C-RED II with 640×480 pixels was available for the MCIFU tests. The complete spectral range was covered by translating the camera. The full spectrograph output is covered by 12 camera positions.

5.2 Mechanical Design

The mechanical design of the spectrograph (see Fig. 10) is simple due to its small size and the optical beam features (slow beams). Moreover, the simplicity was also a requirement due to budget and time constraints from the design to the commissioning. The working angle of the VPHG in respect to the collimator and the angle with the camera are set using two 3D printed
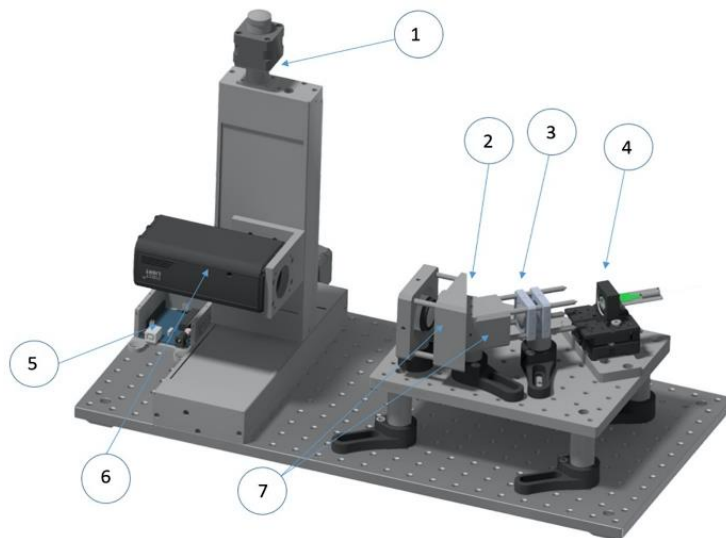
Fig. 10 Mechanical design of the spectrograph from the reformatter to the camera: (1) motorized stages, (2) dispersing element, (3) collimating optical elements, (4) reformatter holder, (5) Arduino control components, (6) C-RED 2 camera, and (7) 3D printed elements.

pieces, allowing for a simple integration and alignment procedure. The additive manufacturing approach was chosen also for the reformatter holder that allows for fitting the reformatted fiber inside a standard mounting. The degrees of freedom of this component are the tip-tilt, the decenter, and the focus. The motorized stages that carry the camera are the same that used in 3D printed setups and allows for covering the full field-of-view by a set of discrete positions.

5.3 Performance

After integration of the spectrograph, we characterized the throughput and resolving power of the spectrograph. To have a good estimation of the spectral throughput of the instrument, we used a tunable light source (TLS) (Oriel TLS-300X). The poor coupling between the faint TLS source and the fiber prevented a good signal/noise for the throughput measurement. To send some light through the instrument, we had to measure the subsystems independently and without the fiber. Moreover, as the $f/\#$ of the source did not match the instrument, we decided to first measure the Multiplexed VPHG, and then the in-line optical train without the VPHG.

The throughput of the spectrograph lenses was also measured with a 1064-nm diode laser, knowing that the spectral response is mainly due to the interface reflections it is consistent with the previous estimations. The throughput of the lenses in the spectrograph is ~0.8 which is consistent with the fact that the first two lenses are not AR coated. The total throughput of the system is then calculated adding the VPHGs contribution. In Fig. 11, we report the spectrographs total throughput and the measured efficiency curves of the Multiplexed VPHG.

With all individual components measured, we can determine the total end-to-end throughput. The wavelength-dependent throughput is shown in Fig. 12. The throughput of CANARY with the WHT (T. Morris, private communication) is also included in the throughput budget. The impact of the AO performance on the coupling efficiency is based on the expected Strehl ratio of CANARY and simulations that determine the relationship between the Strehl ratio and fiber coupling efficiency.[61] From this, we determine that the expected end-to-end throughput is on the order of 0.4%. The main limitations are the fiber link throughput and the AO performance.
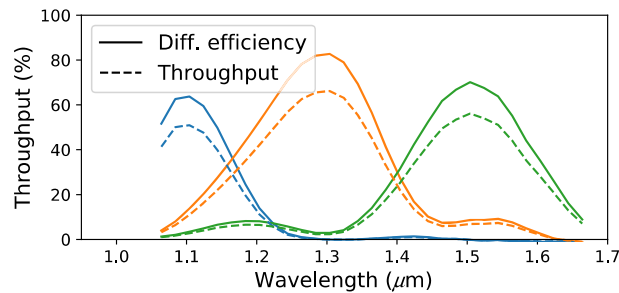
Fig. 11 The measured diffraction efficiency and throughput of the spectrograph without the fiber link as measured by the tunable laser source. The solid lines show the diffraction efficiency of the stacked VPHG system. The dashed lines include the throughput of the spectrograph optics.
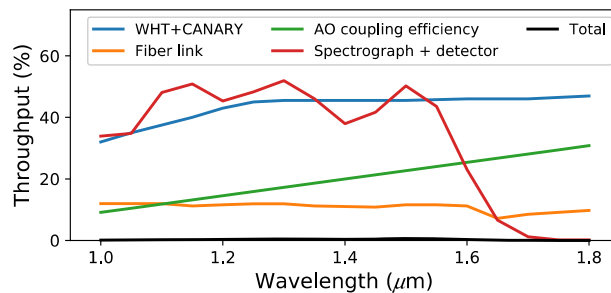

Fig. 12 Throughput of the individual components together with the total throughput (black). The largest limiting factor is the fiber link. The total throughput is 0.4% on average.
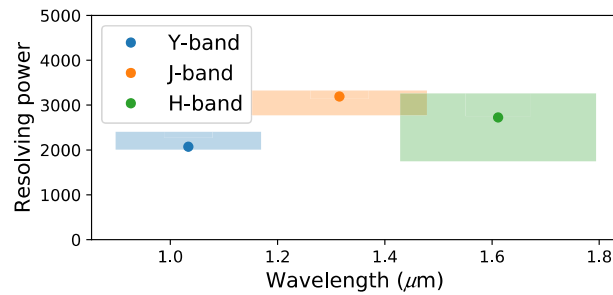
Fig. 13 The measured resolving power of the MCIFU for the three different spectral orders. The shaded area shows the 1-σ resolving power estimates from several emission lines within each order. The points in each area show the median resolving power of that order. The H-band resolving power has a large spread due to line blending of many of the measured lines. The estimated resolving power is a factors 2 to 3 lower than the theoretical limit.

The resolving power of the spectrograph was determined with a Krypton line lamp (Oriel 6031 Kr Spectral Calibration Lamp). To obtain a wavelength solution for all individual cores, we injected the light through the fiber bundle. Even though the line lamp was a large incoherent light source, we were still able to couple enough light into each individual core for the calibration purposes. The wavelength solution was fitted with a first-order polynomial. From the wavelength solution, we derived a linear dispersion of 0.070, 0.850, and 0.095 nm^{-1}. The measured dispersion of each of the gratings was within 1% of the designed dispersion, indicating that the triple stacked grating was manufactured within specifications. From the line lamp measurements, we could also derive the effective resolving power of the spectrograph, which is defined as the center wavelength of the Kr emission lines divided by their FWHM. The resolving power for the different spectral orders is shown in Fig. 13. The effective resolving power is a factor 2 to 3 lower than expected. This is most likely due to a misalignment of the collimation optics, as the PSFs of each emission line are magnified more than expected, show an asymmetry, and have a strong Airy ring. An example of the PSFs which contain these effects can be seen in Fig. 14.
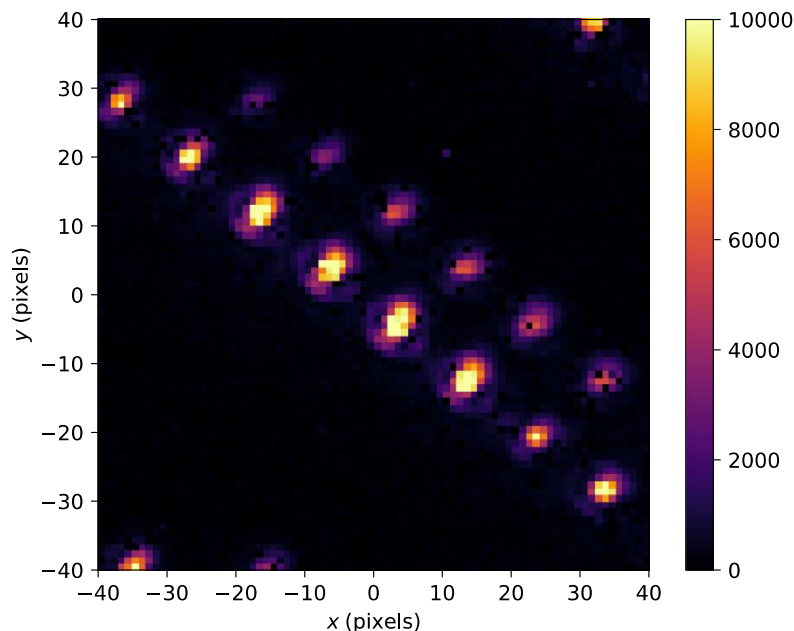
Fig. 14 The PSFs of the spectrograph as measured with the Kr spectral calibration lamp. The horizontal axis is the dispersion axis. The diagonal array of PSFs is the output of a single emission line illuminating a single row of the reformatter. The PSFs are extended and asymmetric toward the north-east and show a clear Airy ring.

These features are not expected from SM waveguides that output Gaussian-like profiles and indicate that we are vignetting the beam inside the spectrograph.

6 Testing with CANARY

The spectrograph was tested with the CANARY AO system at the WHT.[42] CANARY is an AO demonstration test bed for wide-field laserguide star tomography and open-loop AO control. The main purpose of such an AO system is to deliver good wavefront correction over a large field of view. CANARY was used in single-conjugate adaptive optics mode for the MCIFU experiment. In this mode, the wavefront errors are measured by a 7×7 Shack–Hartmann wavefront sensor, which are then fedback to a 52-element deformable mirror (DM) and dedicated tip-tilt mirror. In this configuration, CANARY delivers a Strehl of 30% in nominal atmospheric conditions in H-band. The data were taken between 18 and 21 July, 2019, under the OPTICON open access time. This time was shared with two other groups performing experiments, dividing the nights into sections.

Once assembled, the MCIFU was tested using the internal CANARY sources. We used a modified simulated annealing routine[72] to remove path abberation between the wavefront sensor and the fiber. The algorithm optimized the shape of the DM, maximizing the fiber coupling. This increased the fiber coupling by ~10%.

Several exposures with increasing exposure time were taken to create a high-dynamic range image for the postfiber contrast determination. The postfiber contrast map is shown in Fig. 15. The contrast in the first ring is on the order of 10^{-2}, which is similar to the contrast of the first Airy ring. The map also shows that there is some asymmetry in the PSF. The asymmetry in the contrast map hints on residual astigmatism or coma, which is on the order of 0.5 rad rms by comparing the simulated contrast maps with the data, which is shown in Fig. 15.

6.1 On-Sky Performance

Once on-sky, we targeted bright stars to estimate the performance. Our prime target was Vega, because we could use it as a calibrator star. In Fig. 16, the full spectrograph output is shown by a stitched image of 12 camera positions. Due to the AO tip-tilt variation and because the exposures of the individual camera positions were taken sequentially, there is some variability in the flux between the positions. Not all cores of the MCF could be used during the on-sky demonstration as there was not enough separation between the three orders to fit all the 73 cores, which resulted in overlapped spectra. The top and bottom of the reformatter was blocked with a mask to remove the overlapping spectra.
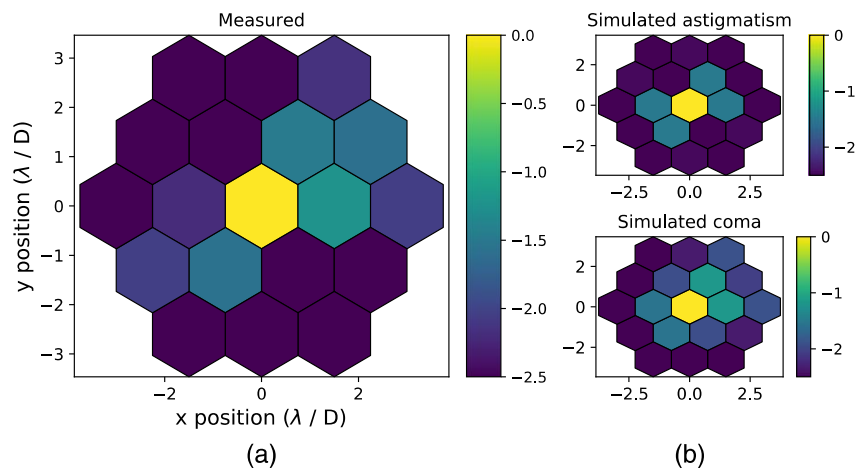
Fig. 15 (a) The monochromatic post-fiber contrast map on a logarithmic scale as measured with a 1550-nm laser. (b) A comparison of the asymmetry in the illumination with simulations hints on the presence of 0.5-rad rms residual astigmatism and/or coma.
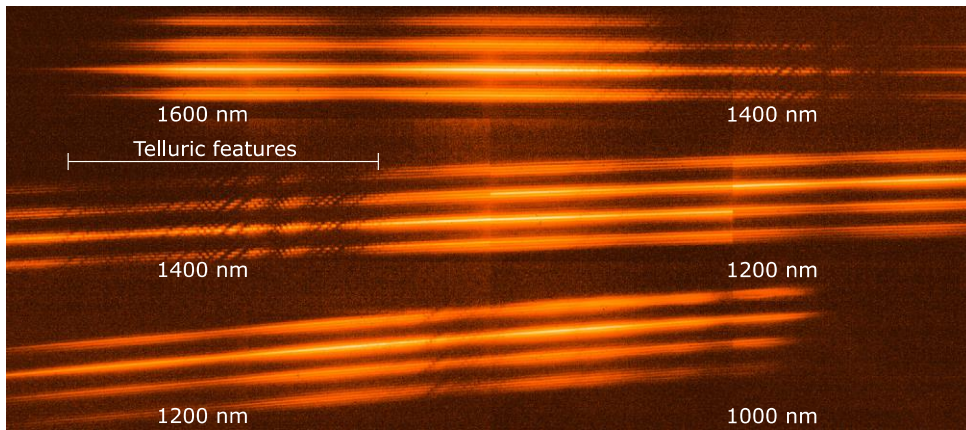
Fig. 16 The full spectrograph output of Vega after stitching 12 detector positions together. The color of the image is logarithmically stretched to highlight the spectra from the fainter fiber cores. Each fiber captures a different part of the PSF at the input, therefore the brightness of the spectral trace corresponds with the brightness of the captured part of the PSF. The main features that are visible are the telluric lines imprinted into the spectrum of Vega. Abrupt changes in the continuum of the individual cores are visible because the full image was reconstructed from 12 observations that were taken one after another, with varying conditions. The beginning and end of each spectrum has been marked with the corresponding wavelength.

Vega is an A0 star which means that it is almost featureless, the main spectral features that are visible come from the Earth's telluric absorption lines. Figure 17 shows the extracted spectrum from 1310 to 1390 nm averaged over all fibers. We chose this part of the spectrum as it illustrates the effect of the telluric features. The telluric features allowed us to do an independent measurement of the on-sky resolving power and wavelength solution. We used the ESO SkyCalc[73,74] to generate a transmission spectrum using the standard Paranal atmospheric parameters. Vega was modeled with a high-resolution PHOENIX stellar model[75] with an effective stellar temperature of $T_{\mathrm{eff}} = 9600$, metallicity of $Z = -0.5$, and surface gravity log $g = 4.0$. We used a fourth-order polynomial for the instrument throughput and also used a fourth-order polynomial for the wavelength solution. The high-resolution spectrum was convolved by a Gaussian with a certain width to mimic the effect of the spectrograph resolving power. The retrieved resolving power from this procedure was $R = 2970$, which matches very well with the estimated resolving power from the Kr line lamp. We did not match all features in the observed spectrum because the parameters of both the telluric model and the stellar model were fixed. The good match between the measured and modeled spectra shows that we can extract high fidelity spectra that are not contaminated by etalon and fringing effects. Previous SMFs spectrographs were plagued by strong etalon amplitude variations, which could be up to 10% across the spectra.[24,63]

Because of the optical layout of CANARY and the MCIFU, it was not possible to image the PSF and the spectrograph output. Therefore, we were not able to get a direct estimate for the on-sky fiber coupling efficiency.
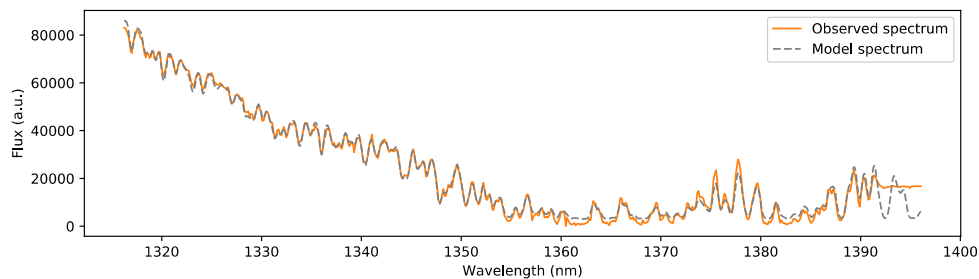
Fig. 17 The spatially averaged spectrum of Vega from 1300 to 1400 nm. The structure of this part of the spectrum of Vega is predominantly caused by the telluric absorption lines.
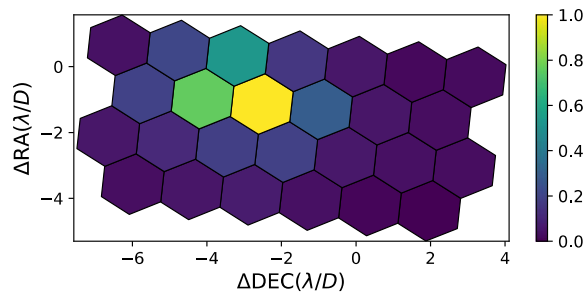
Fig. 18 The on-sky reconstructed H-band image, using the MCIFU, of the bright star Alpha Herculis. The observations were taken at 10 Hz. The image shown here is the mean of 1000 successive images from the data stream. Each microlens samples roughly $1.3\lambda/D$. The asymmetry in the PSF comes from a slow drift in tip/tilt alignment during the observations.

A second target that was observed was Alpha Herculis, one of the brightest infrared targets in the sky with magnitudes of $J = -2.3$ and $H = -3.2$.[76] The brightness of the target allowed us to do high-speed integral-field spectroscopy at 10 Hz, at a single camera position. In Fig. 18, we show the reconstructed H-band PSF of one of the exposures.

During the OPTICON July 2019 run at the WHT, another experiment was performed to characterize AO performance with a more sophisticated controller, the linear quadratic Gaussian (LQG) regulator instead of the standard integrator. The LQG regulator relies on a model that describes the temporal dynamics of the disturbance and whose relevance is a key for a performance improvement. It includes both the autoregressive order 2 model on the first 495 Zernike modes built from turbulence priors as described in Ref. 77, and a data-driven model for the nine first modes estimated from recent AO telemetry data. This LQG controller provides a more accurate modeling of the temporal dynamics for the most energetic modes: not only vibrations on the tip and tilt but most of other sources of disturbance on the nine first modes is captured whether it comes from dome turbulence, windshake, or atmospheric turbulence. Implementing this, LQG controller required very little tuning and proved to deliver increased performance and to be much more stable than the integrator.[78] During the night from 21st to 22nd July, 2019, we observed Alpha Herculis both with the integrator and the LQG and measured the impact on the tip-tilt residuals. To estimate the performance, we made a white light image of the IFU PSF and calculated the centroid of the white-light PSF as function of time. The centroid was measured using the center-of-mass of each PSF. We estimated that the LQG successfully decreased the standard deviation of the centroid by a factor of $\sim$1.4.

7 Discussion

The on-sky tests of the MCIFU have shown that the components are able to work together on-sky to deliver an SMF-fed NIR integral field spectrograph (IFS). It was not possible to optimize the performance of all components due to the short time (6 months), between inception of the instrument and the on-sky demonstration. Because the MCIFU is modular, it is possible to redesign and optimize individual components and switch them for better performance. There are several parts that we have identified that can be improved with a clear path.

7.1 *Fiber Link Improvements*

Our complete fiber link system showed throughput of between a few and 27% for individual cores. As this fiber link was a new system developed in only a few months, we are happy with its initial performance. For future experiments, we will develop a new fiber, with the aim of increasing both throughput and uniformity. Our target is to bring the fiber link throughput much closer to 50%. To achieve the increase in the performance for our new reformatter, we will need to improve our ability to accurately control the inscription to create a better mode matching between the cores and to optimize their alignment. A shorter pulse laser can allow us to optimize

the laser–matter interaction in the substrate and enhance the inscription accuracy. By this way, we expect to increase the throughput for the straight waveguide and enable a more precise alignment of the MCF with the ULI wavguides to avoid the variations in throughput seen in Fig. 4.

Further improvements in practical coupling efficiencies by the microlenses should also be possible as we keep developing the manufacturing process. Past work/experiences have shown that the coupling efficiency that can be achieved in the lab is close to the theoretical modeling. Yet, the current microlenses were higher and printed over a much larger surface than normal, likely effecting performance of the outer lenses. The most probable cause is shrinkage of the structure during the curing step. Shrinkage has a stronger effect on the outer cores than the inner cores. Thus, further optimization and refinement/iterations need to be made to improve efficient coupling. And finally, an AR coating can be added to the microlenses to get the highest possible throughput.

7.2 Spectrograph Improvements

The triple stacked VPHG shows a performance close to the theoretical design limit. This indicates that we are operating at the current manufacturing limit of the VPHG technology. The main limiting factor in the spectrograph is the collimation optics. The alignment of the separate singlets is quite sensitive, and there is quite a large loss of throughput due to the uncoated optics. Both the throughput and the resolving power can be improved by a redesign of the collimation optics.

7.3 New Detector

Currently, a C-RED 2 is used as a detector for the MCIFU. The C-RED 2 is designed for a small field of view high-speed NIR imaging and not long-integration spectroscopy. Due to the high read noise and dark current of the C-RED 2, the single spectral channel limiting magnitude in 1 h is about 12th magnitude at the WHT if we exclude the contributions from the background. Combining all spectral channels could improve this to about 15th magnitude. Because of the low number of detector pixels, we need to scan the spectrograph focal plane in several steps, which as shown in this work makes postprocessing more difficult due to tip-tilt stability. Ideally, we would use a detector with 2 k × 2 k pixels and low read and dark noise. Currently, the best available solution for us would be a HAWAII-2RG,[79] though we also note the increasing pixel numbers on SAPHIRA detectors and a 2 k × 2 k version would make a very attractive solution. Switching to a HAWAII-2RG would increase the limiting magnitude by five magnitudes.

7.4 On Sky

CANARY is an AO demonstration test bed for wide-field laser guide star tomography and open-loop AO control. For high-contrast imaging of exoplanets, we need to use ExAO systems that focus only on a very small field of view around the star. For SMF optics, this reduces the coupling into the fiber which is proportional to the Strehl.[61] For our observations, the estimated on-axis Strehl from CANARY was between 5% and 15% in the H, which will be lower in the J band. The Strehl was lower than expected due to poor atmospheric conditions. This shows an advantage of integral-field spectroscopy as opposed to single-object spectroscopy where the full PSF is injected into a single SMF.[26] Due to the microlenses and multiple fiber, the MCIFU is much less sensitive to pointing errors and residual tip/tilt errors. But adding the MCIFU behind an ExAO system that delivers high Strehl in the NIR such as the Magellan Adaptive Optics Extreme (MagAO-X) system[80] would allow for much higher coupling into the fiber. Due to the high Strehl, it would also be possible to use high-performance coronagraphs to reduce the amount of starlight that pollutes the planet signal. The past few years have shown that with SMFs it is possible to make higher performance coronagraphs.[51–54,62]

We reckon that after implementing all proposed upgrades, the throughout can be significantly increased. An overview of the current and target throughput for each subsystem is shown in Table 2. For the current system, three components are significantly limiting the throughput, the AO performance, the microlens coupling, and the reformatter. The throughput can be increased

Table 2 Wavelength averaged instrument throughput.

Subsystem	Current	Optimal	What to improve
WHT + CANARY	0.43	0.43	
Microlenses absorption	0.90	0.96	Thinner microlenses
Microlens alignment	0.3	0.9	More development time
AO coupling	0.2	0.66	Switch to ExAO system with Strehl above 90%
Reformatter	0.4	0.7	Refinement of the manufacturing
Spectrograph	0.8	0.9	New AR coatings
VPH	0.5	0.6	Refinement of the manufacturing
Detector	0.8	0.9	Switch to HAWAII-2RG
Total	0.003 (0.005)	0.07 (0.11)	Peak throughput in brackets

by a factor close to 20 if only these three components are addressed, which shows the importance of further refinement of the fiber link and future tests on ExAO systems.

8 Conclusions

Here, we present the MCIFU an innovative prototype SMF-fed IFS designed to characterize exoplanets that can easily be added to existing and future high contrast imaging instruments. The PSF from an AO or ExAO system is focused on a 3D printed MLA which feeds an MCF. At the entrance to the spectrograph, the output slit is formed using an ULI reformatter. The spectrograph itself is formed from off-the-shelf components, 3D printed components, a custom set of triple stacked VPHGs, and a C-RED 2 detector. The prototype instrument itself went from design to telescope in ~6 months. Due to its modular nature, the instrument can be easily upgraded and adapted for observations with other AO systems.

The SMF link has been demonstrated to work on-sky, even in low Strehl conditions which are challenging for instruments where the full PSF is injected into a single SMF. We derived a resolving power consistent with our lab measurements from the telluric lines in the observed spectrum of Vega. And furthermore, we demonstrated that it is possible to get high-speed integral-field spectra with the current MCIFU. With our observations, we could confirm the improved performance of a new AO real-time control algorithm.

Both the fiber link and spectrograph performance are slightly less than half the theoretical maximum, with the fiber link throughput being around 20% and the resolving power being around 3000. This is due to the short manufacture and assembly time, and currently work is being done to improve and we plan to test the first modifications with MagAO-X. We will compare our results with those from CANARY and then begin a modular improvement program, bringing the system from prototype to full instrument.

Acknowledgments

82

Data, Materials, and Code Availability

All data that were used to support this work can be found at doi: 10.25422/azu.data.12857885.

References

1. I. A. G. Snellen et al., "The orbital motion, absolute mass and high-altitude winds of exoplanet HD209458b," *Nature* **465**, 1049–1051 (2010).
2. D. K. Sing et al., "A continuum from clear to cloudy hot-Jupiter exoplanets without primordial water depletion," *Nature* **529**, 59–62 (2016).
3. L. Kreidberg et al., "Absence of a thick atmosphere on the terrestrial exoplanet LHS 3844b," *Nature* **573**, 87–90 (2019).
4. D. Charbonneau et al., "Detection of thermal emission from an extrasolar planet," *Astrophys. J.* **626**, 523–529 (2005).
5. M. Brogi et al., "The signature of orbital motion from the dayside of the planet τ Boötis b," *Nature* **486**, 502–504 (2012).
6. H. J. Hoeijmakers et al., "Atomic iron and titanium in the atmosphere of the exoplanet KELT-9b," *Nature* **560**, 453–455 (2018).
7. J. L. Beuzit et al., "SPHERE: the exoplanet imager for the very large telescope," *Astron. Astrophys.* **631**, A155 (2019).
8. B. Macintosh et al., "First light of the Gemini planet imager," *Proc. Natl. Acad. Sci. U. S. A.* **111**, 12661–12666 (2014).
9. N. Jovanovic et al., "The Subaru coronagraphic extreme adaptive optics system: enabling high-contrast imaging on solar-system scales," *Publ. Astron. Soc. Pac.* **127**, 890 (2015).
10. A. M. Lagrange et al., "A probable giant planet imaged in the β Pictoris disk. VLT/NaCo deep L'-band imaging," *Astron. Astrophys.* **493**, L21–L25 (2009).
11. M. Bonnefoy et al., "The near-infrared spectral energy distribution of β Pictoris b," *Astron. Astrophys.* **555**, A107 (2013).
12. M. Keppler et al., "Discovery of a planetary-mass companion within the gap of the transition disk around pds 70," *Astron. Astrophys.* **617**, A44 (2018).
13. A. Müller et al., "Orbital and atmospheric characterization of the planet within the gap of the PDS 70 transition disk," *Astron. Astrophys.* **617**, L2 (2018).
14. B. P. Bowler et al., "Planets around low-mass stars (PALMS). IV. The outer architecture of M Dwarf planetary systems," *Astrophys. J. Suppl. Ser.* **216**, 7 (2015).
15. K. Wagner, D. Apai, and K. M. Kratter, "On the mass function, multiplicity, and origins of wide-orbit giant planets," *Astrophys. J.* **877**, 46 (2019).
16. A. Vigan et al., "The SPHERE infrared survey for exoplanets (SHINE). III. The demographics of young giant exoplanets below 300 au with SPHERE," arXiv:2007.06573 (2020).
17. C. Marois et al., "Angular differential imaging: a powerful high-contrast imaging technique," *Astrophys. J.* **641**, 556–564 (2006).

18. J. Antichi et al., "BIGRE: a low cross-talk integral field unit tailored for extrasolar planets imaging spectroscopy," *Astrophys. J.* **695**, 1042–1057 (2009).
19. W. B. Sparks and H. C. Ford, "Imaging spectroscopy for extrasolar planet detection," *Astrophys. J.* **578**, 543–564 (2002).
20. P. Riaud and J. Schneider, "Improving Earth-like planets' detection with an ELT: the differential radial velocity experiment," *Astron. Astrophys.* **469**, 355–361 (2007).
21. H. Kawahara et al., "Spectroscopic coronagraphy for planetary radial velocimetry of exoplanets," *Astrophys. J. Suppl. Ser.* **212**, 27 (2014).
22. I. Snellen et al., "Combining high-dispersion spectroscopy with high contrast imaging: probing rocky planets around our nearest neighbors," *Astron. Astrophys.* **576**, A59 (2015).
23. J. Wang et al., "Observing exoplanets with high dispersion coronagraphy. I. The scientific potential of current and next-generation large ground and space telescopes," *Astron. J.* **153**, 183 (2017).
24. A. D. Rains et al., "Development of the single-mode fiber integral field unit for the RHEA spectrograph," *Proc. SPIE* **10702**, 107025J (2018).
25. S. Y. Haffert et al., "On-sky results of the Leiden EXoplanet Instrument (LEXI)," *Proc. SPIE* **10703**, 1070323 (2018).
26. D. Mawet et al., "Keck planet imager and characterizer: status update," *Proc. SPIE* **10703**, 1070306 (2018).
27. I. A. G. Snellen et al., "Fast spin of the young extrasolar planet β Pictoris b," *Nature* **509**, 63–65 (2014).
28. H. J. Hoeijmakers et al., "Medium-resolution integral-field spectroscopy for high-contrast exoplanet imaging. Molecule maps of the β Pictoris system with SINFONI," *Astron. Astrophys.* **617**, A144 (2018).
29. Q. M. Konopacky et al., "Detection of carbon monoxide and water absorption lines in an exoplanet atmosphere," *Science* **339**, 1398–1401 (2013).
30. T. S. Barman et al., "Simultaneous detection of water, methane, and carbon monoxide in the atmosphere of Exoplanet HR8799b," *Astrophys. J.* **804**, 61 (2015).
31. D. J. M. P. dit de la Roche, H. J. Hoeijmakers, and I. A. G. Snellen, "Molecule mapping of HR8799b using OSIRIS on Keck. Strong detection of water and carbon monoxide, but no methane," *Astron. Astrophys.* **616**, A146 (2018).
32. J.-B. Ruffio et al., "Radial velocity measurements of HR 8799 b and c with medium resolution spectroscopy," *Astron. J* **158**, 200 (2019).
33. K. Wagner et al., "Magellan adaptive optics imaging of PDS 70: measuring the mass accretion rate of a young giant planet within a gapped disk," *Astrophys. J.* **863**, L8 (2018).
34. S. Y. Haffert et al., "Two accreting protoplanets around the young star PDS 70," *Nat. Astron* **3**, 749–754 (2019).
35. S. G. Leon-Saval, C. H. Betters, and J. Bland-Hawthorn, "The photonic tiger: a multicore fiber-fed spectrograph," *Proc. SPIE* **8450**, 84501K (2012).
36. R. J. Harris et al., "Photonic spatial reformatting of stellar light for diffraction-limited spectroscopy," *Mon. Not. R. Astron. Soc.* **450**(1), 428–434 (2015).
37. P.-I. Dietrich et al., "Printed freeform lens arrays on multi-core fibers for highly efficient coupling in astrophotonic systems," *Opt. Express* **25**, 18288 (2017).
38. P. I. Dietrich et al., "*In situ* 3D nanoprinting of free-form coupling elements for hybrid photonic integration," *Nat. Photonics* **12**, 241–247 (2018).
39. R. R. Thomson et al., "Ultrafast laser inscription of a 121-waveguide fan-out for astrophotonics," *Opt. Lett.* **37**, 2331–2333 (2012).
40. A. Boccaletti et al., "SPHERE+: imaging young Jupiters down to the snowline," arXiv:2003.05714 (2020).
41. A. Zanutta et al., "Spectral multiplexing using stacked volume-phase holographic gratings–I," *Mon. Not. R. Astron. Soc.* **469**(2), 2412–2422 (2017).
42. E. Gendron et al., "Final two-stage MOAO on-sky demonstration with canary," *Proc. SPIE* **9909**, 99090C (2016).
43. R. Bacon et al., "3D spectrography at high spatial resolution. I. Concept and realization of the integral field spectrograph TIGER," *Astron. Astrophys. Suppl. Ser.* **113**, 347 (1995).

84

44. N. Thatte et al., "Very high contrast integral field spectroscopy of AB Doradus C: 9-mag contrast at 0.2 arcsec without a coronagraph using spectral deconvolution," *Mon. Not. R. Astron. Soc.* **378**, 1229–1236 (2007).

45. T. D. Groff et al., "The CHARIS IFS for high contrast imaging at Subaru," *Proc. SPIE* **9605**, 96051C (2015).

46. A. J. Skemer et al., "First light with ALES: a 2-5 micron adaptive optics integral field spectrograph for the LBT," *Proc. SPIE* **9605**, 96051D (2015).

47. A. Vigan et al., "High-contrast imaging of Sirius A with VLT/SPHERE: looking for giant planets down to one astronomical unit," *Mon. Not. R. Astron. Soc.* **454**, 129–143 (2015).

48. J. R. Males and O. Guyon, "Ground-based adaptive optics coronagraphic performance under closed-loop predictive control," *J. Astron. Telesc. Instrum. Syst.* **4**, 019001 (2018).

49. C. Vanderriest, "A fiber-optics dissector for spectroscopy of nebulosities around quasars and similar objects," *Publ. Astron. Soc. Pac.* **92**, 858–862 (1980).

50. J. R. Allington-Smith et al., "Integral field spectroscopy with the gemini multiobject spectrographs," *Proc. SPIE* **2871**, 1295–1305 (1997).

51. D. Mawet et al., "Observing exoplanets with high-dispersion coronagraphy. II. Demonstration of an active single-mode fiber injection unit," *Astrophys. J.* **838**, 92 (2017).

52. E. H. Por and S. Y. Haffert, "The single-mode complex amplitude refinement (SCAR) coronagraph. I. Concept, theory, and design," *Astron. Astrophys.* **635**, A55 (2020).

53. G. Ruane et al., "Efficient spectroscopy of exoplanets at small angular separations with vortex fiber nulling," *Astrophys. J.* **867**, 143 (2018).

54. C. T. Coker et al., "Simulations of a high-contrast single-mode fiber coronagraphic multiobject spectrograph for future space telescopes," *J. Astron. Telesc. Instrum. Syst.* **5**, 045003 (2019).

55. R. G. Petrov et al., "AMBER, the near-infrared spectro-interferometric three-telescope VLTI instrument," *Astron. Astrophys.* **464**, 1–12 (2007).

56. Gravity Collaboration et al., "First light for GRAVITY: phase referencing optical interferometry for the very large telescope interferometer," *Astron. Astrophys.* **602**, A94 (2017).

57. J. R. Crepp et al., "iLocater: a diffraction-limited Doppler spectrometer for the large binocular telescope," *Proc. SPIE* **9908**, 990819 (2016).

58. J. Baudrand and G. A. H. Walker, "Modal noise in high-resolution, fiber-fed spectra: a study and simple cure," *Publ. Astron. Soc. Pac.* **113**, 851–858 (2001).

59. L. S. Fohrmann et al., "Single mode thermal emission," *Opt. Express* **23**, 27672–27682 (2015).

60. J. C. Corbett, "Sampling of the telescope image plane using single- and few-mode fibre arrays," *Opt. Express* **17**, 1885–1901 (2009).

61. N. Jovanovic et al., "Efficient injection from large telescopes into single-mode fibres: enabling the era of ultra-precision astronomy," *Astron. Astrophys.* **604**, A122 (2017).

62. S. Y. Haffert et al., "The single-mode complex amplitude refinement (SCAR) coronagraph. II. Lab verification, and toward the characterization of Proxima b," *Astron. Astrophys.* **635**, A56 (2020).

63. A. D. Rains et al., "Precision single mode fibre integral field spectroscopy with the RHEA spectrograph," *Proc. SPIE* **9908**, 990876 (2016).

64. C. H. Betters et al., "PIMMS Échelle: the next generation of compact diffraction limited spectrographs for arbitrary input beams," *Proc. SPIE* **9147**, 91471I (2014).

65. I. Spaleniak et al., "Integrated photonic building blocks for next-generation astronomical instrumentation II: the multimode to single mode transition," *Opt. Express* **21**, 27197–27208 (2013).

66. D. G. MacLachlan et al., "Efficient photonic reformatting of celestial light for diffraction-limited spectroscopy," *Mon. Not. R. Astron. Soc.* **464**(4), 4950–4957 (2016).

67. C. A. Ross et al., "Optimisation of ultrafast laser assisted etching in fused silica," *Opt. Express* **26**(19), 24343–24356 (2018).

68. N. Jovanovic et al., "Starlight demonstration of the dragonfly instrument: an integrated photonic pupil-remapping interferometer for high-contrast imaging," *Mon. Not. R. Astron. Soc.* **427**(1), 806–815 (2012).

85

69. T. Gissibl et al., "Refractive index measurements of photo-resists for three-dimensional direct laser writing," *Opt. Mater. Express* **7**, 2293–2298 (2017).

70. Nanoscribe, "Ip photoresins," 2020, https://www.nanoscribe.com/en/solutions/materials #tab-880.

71. A. Zanutta et al., "Photopolymeric films with highly tunable refractive index modulation for high precision diffractive optics," *Opt. Mater. Express* **6**(1), 252–263 (2016).

72. S. Kirkpatrick, C. D. Gelatt, and M. P. Vecchi, "Optimization by simulated annealing," *Science* **220**(4598), 671–680 (1983).

73. S. Noll et al., "An atmospheric radiation model for Cerro Paranal. I. The optical spectral range," *Astron. Astrophys.* **543**, A92 (2012).

74. A. Jones et al., "An advanced scattered moonlight model for Cerro Paranal," *Astron. Astrophys.* **560**, A91 (2013).

75. T. O. Husser et al., "A new extensive library of PHOENIX stellar atmospheres and synthetic spectra," *Astron. Astrophys.* **553**, A6 (2013).

76. R. M. Cutri et al., "VizieR online data catalog: 2MASS all-sky catalog of point sources (Cutri+ 2003)," VizieR Online Data Catalog, II/246 (2003).

77. G. Sivo et al., "First on-sky SCAO validation of full LQG control with vibration mitigation on the CANARY pathfinder," *Opt. Express* **22**(19), 23565–23591 (2014).

78. B. Sinquin et al., "On-sky results for adaptive optics control with data-driven models on low-order modes," *Mon. Not. R. Astron. Soc.* **498**, 3228–3240 (2020).

79. M. Kissler-Patig et al., "HAWK-I: the high-acuity wide-field K-band imager for the ESO very large telescope," *Astron. Astrophys.* **491**, 941–950 (2008).

80. J. R. Males et al., "MagAO-X: project status and first laboratory results," *Proc. SPIE* **10703**, 1070309 (2018).

Sebastiaan Y. Haffert is a NASA Hubble postdoctoral fellow at the University of Arizona's Steward Observatory. He received his PhD in astronomy cum laude from Leiden University in 2019. His research focuses on high-spatial and high-spectral resolution instrumentation for exoplanet characterization.

Robert J. Harris received his PhD from Durham University in 2014, modeling astrophotonic devices and spectrographs and developing photonic reformatters for high-resolution spectroscopy. Following his PhD and a STEP postdoc (again at Durham), he took up a Carl-Zeiss fellowship at the Landessternwarte, Heidelberg, where he was also awarded the Gliese fellowship. He is currently working at the MPIA in Heidelberg.

Biographies of the other authors are not available.

J. Astron. Telesc. Instrum. Syst.   045007-24   Oct–Dec 2020 • Vol. 6(4)

86

Chapter 4- Ultrafast laser inscription of asymmetric integrated waveguide 3 dB couplers for astronomical K-band interferometry at the CHARA array

4.1   Introduction

4.1.1   How does stellar interferometry work?

The angular resolution of any single aperture imaging system is limited to $\sim \frac{\lambda}{D}$, where λ is the wavelength of the light, and D is the diameter of the collecting aperture. Interferometry provides a route to overcome this limitation by coherently combining the light captured by multiple widely spaced telescopes. In this case, the resolution of the imaging is limited by the separation distance between the telescopes, which can be hundreds of metres, not the individual aperture size of the telescopes which are currently 8-10 m at visible/infrared wavelengths (with the construction of the ELTs now underway).

To understand how interferometry works, Figure 30 presents a schematic diagram of Young's double slits when illuminated by monochromatic light originating from either a single point source at infinity, or two point sources at infinity. In the first case, the light will generate fringes on a screen with an angular fringe separation of $\frac{\lambda}{b}$ rad, and a fringe spatial frequency of $\frac{b}{\lambda}$ rad^{-1}. The visibility of these fringes $\left(V = \frac{I_{Max} - I_{Min}}{I_{Max} + I_{Min}} \right)$ will also be 1. In the second case, where two incoherent point sources produce separate fringe patterns, the visibility of the overall fringe pattern observed will gradually reduce as the source separation increases, completely disappearing when the point sources are angularly separated by half the fringe spacing $\left(\frac{\lambda}{2b} \right)$.

Although the example in Figure 30 is for the situation of Young's double slits (a simple screen behind two apertures), the situation can be extended to the case of telescopes viewing a celestial object(s). In this case, the slits are replaced by telescopes, and the screen is replaced by a beam combining instrument (examples of which will be discussed later) which is located at some position between the telescopes.
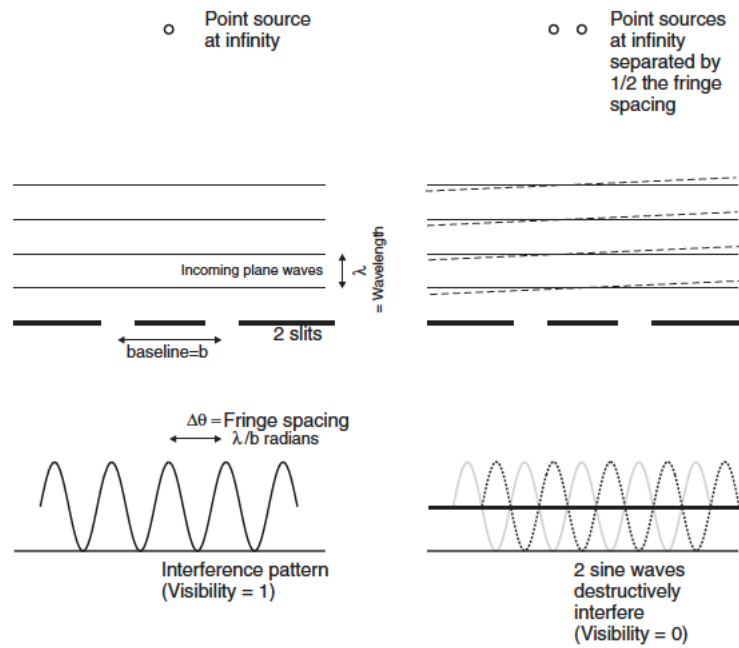
Figure 30: Schematic diagrams of (Left) Young's slits illuminated by a monochromatic point source at infinity. (Right) Young's slits illuminated by two monochromatic incoherent point sources at infinity, separated by half of the fringe spacing shown on the right. Taken and adapted from [90].

Obviously, the situations shown in Figure 30 are idealised. To be of use for imaging applications we need to understand how the interferometer fringes relate *in general* to the object intensity distribution. The answer to this can be obtained somewhat logically by considering what happens to the fringes we observe as we move away from the situation of an idealised monochromatic point source. As shown in Figure 31(b), in comparison to the high visibility (V = 1) infinite series of fringes we would observe from a monochromatic point source, Figure 31(a), a polychromatic point source will result in a fringe packet (black) which is the result of the overlapping monochromatic fringes from each wavelength within the signal. The situation for a spatially extended monochromatic source is shown in Figure 31(c), where it can be seen that the resultant fringes (black) are the result of the overlapping, but offset, high visibility (V = 1) infinite series of fringes from each monochromatic point source across the object, resulting in an infinite series of reduced visibility (V < 1) fringes. The situation for an extended polychromatic source is shown in Figure 31(d), where it can be seen that the result is a fringe packet of reduced visibility.
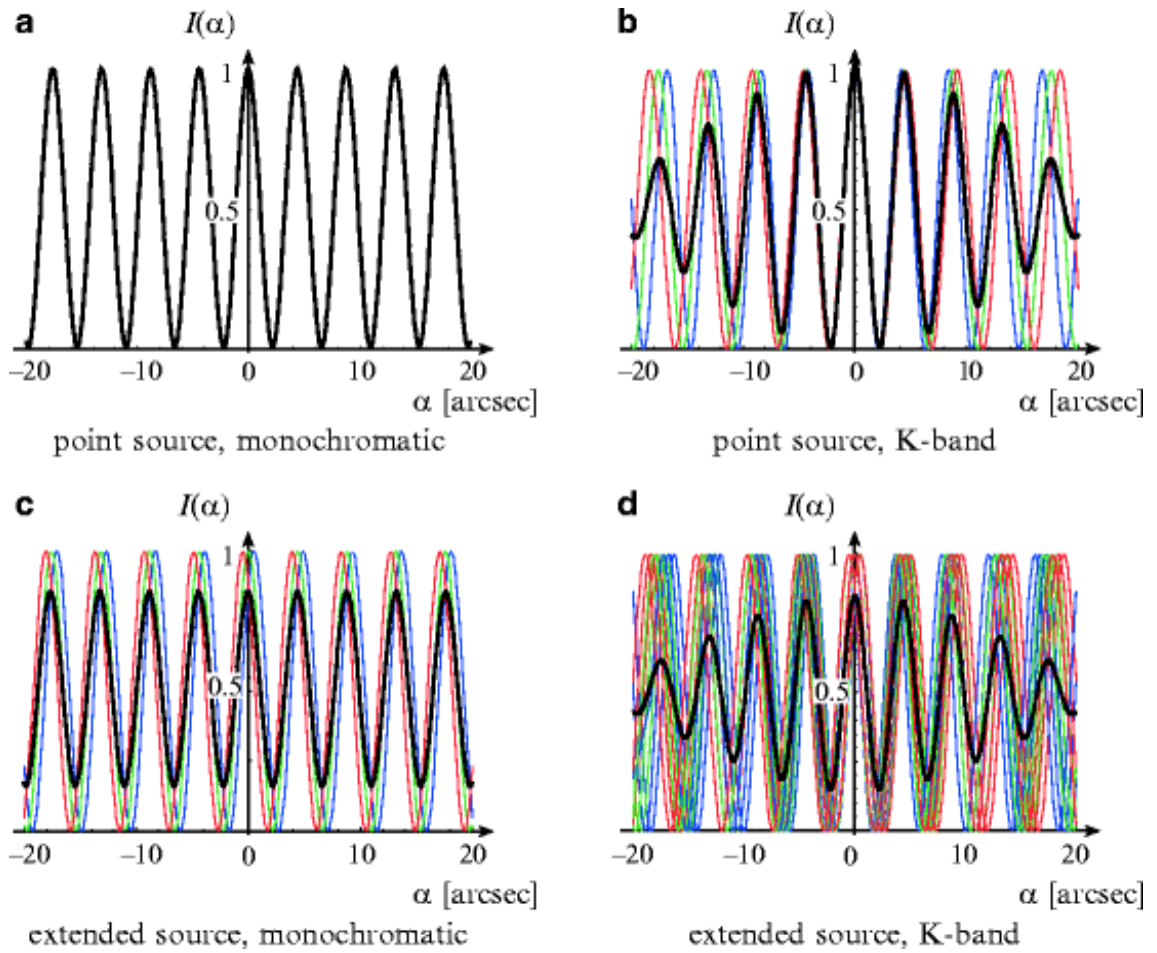
Figure 31: Fringe patterns (black) that would be expected from a two-telescope beam combiner when viewing (a) a monochromatic point source, (b) a polychromatic point source, (c) a monochromatic extended source and, (d) a polychromatic extended source. Reprinted/adapted by permission from Springer Nature: Propagation of Light by A. Glindemann © (2011)[91].

From the above, it is clear that it is the *visibility* of the fringes measured by an interferometer which holds information about the spatial properties of the source. The nature of this specific relationship is strongly hinted at by Figure 30, where it can be seen that the visibility of the fringes measured for two point sources goes to 0 when they are angularly separated by half the spacing of the fringes generated by one point source $\left(\frac{\lambda}{2b}\right)$, and then back up to 1 when they become angularly separated by $\frac{\lambda}{b}$. It is also notable and interesting to note that the $\frac{b}{\lambda}$ component of the Fourier transorm of such an object will also have a magnitude of 0 when the objects are separated by $\left(\frac{\lambda}{2b}\right)$, and 1 for the $\frac{b}{\lambda}$ component when the objects are separated by $\frac{\lambda}{b}$. Given these relations, it not unreasonable to consider that the visibility of the interferogram measured by an interferometer with a baseline, *b*, is directly related to the amplitude of the $\frac{b}{\lambda}$ component

of the image Fourier transform, and indeed this is the case. Although it is beyond the scope of this thesis, the Van Cittert-Zernike theorem does indeed link the visibility of the interferometer fringes to a unique Fourier component of the object distribution, $\frac{D}{\lambda}$, where D is the interferometer baseline projected onto the sky.

Clearly, measuring the amplitude of one Fourier component of the object's intensity distribution is not sufficient to reconstruct an accurate image. To do so, requires the acquisition of many such amplitudes and their relative phases, a feat which is achieved in a number of ways. First, it should be noted that even a two-telescope interferometer can provide information about more than one Fourier component since the object can be viewed from multiple different angles as the Earth rotates, and also at multiple different wavelengths. Secondly, the number of baselines can be increased by using more than just two telescopes, and an N telescope array provides $\frac{N^2-N}{2}$ independent baselines. Figure 32 shows an example of how the Fourier plane can be "filled in" using a two-dimensional array of telescopes and multiple measurements over the period of a few hours to allow the Earth to rotate. Once the amplitudes and relative phases of these Fourier amplitudes are known, the object intensity distribution can then be reconstructed using numerical algorithms such as CLEAN [92].
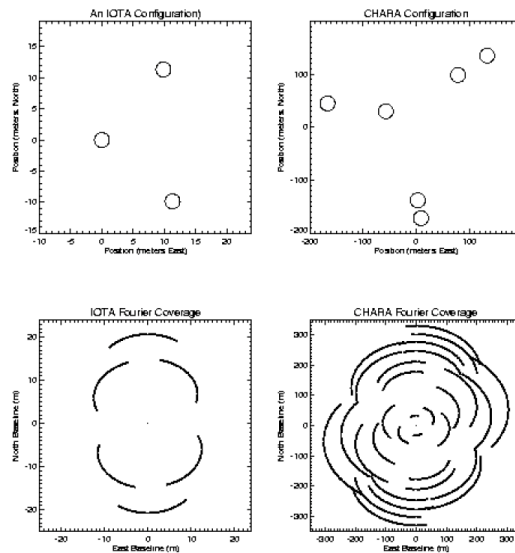

Figure 32: (Top row) Diagrams showing the positions of the telescopes in the IOTA and CHARA arrays. (Bottom row) Diagrams presenting the Fourier coverage enabled by the the IOTA and CHARA arrays. Taken and adapted from [90].

4.1.2 Beam combination

The properties of the telescope array are clearly crucial to the operation of the interferometer, but the interferometer cannot operate unless the beams are interferometrically combined. This is the task of the beam combiner, and many different approaches can be taken. As shown in Figure 33, for the case of a two telescope interferometer, the beams from the telescopes can either be combined in the image plane, where the images generated by telescope are overlapped onto a camera, or in the pupil plane, where light from each telescope is projected first onto a 50/50 mirror, and then onto single pixel detectors. In the first case, the result is an image of the object which is modulated by fringes, in the second the result is an interferogram which is generated by using a delay line in one of the optical paths is to scan the relative delay between both paths through 0. It is the pupil plane combination which has become the most standard approach in modern interferometry for a variety of reasons, not least the fact that single pixel detectors offer superior noise advantages compared to detector arrays.
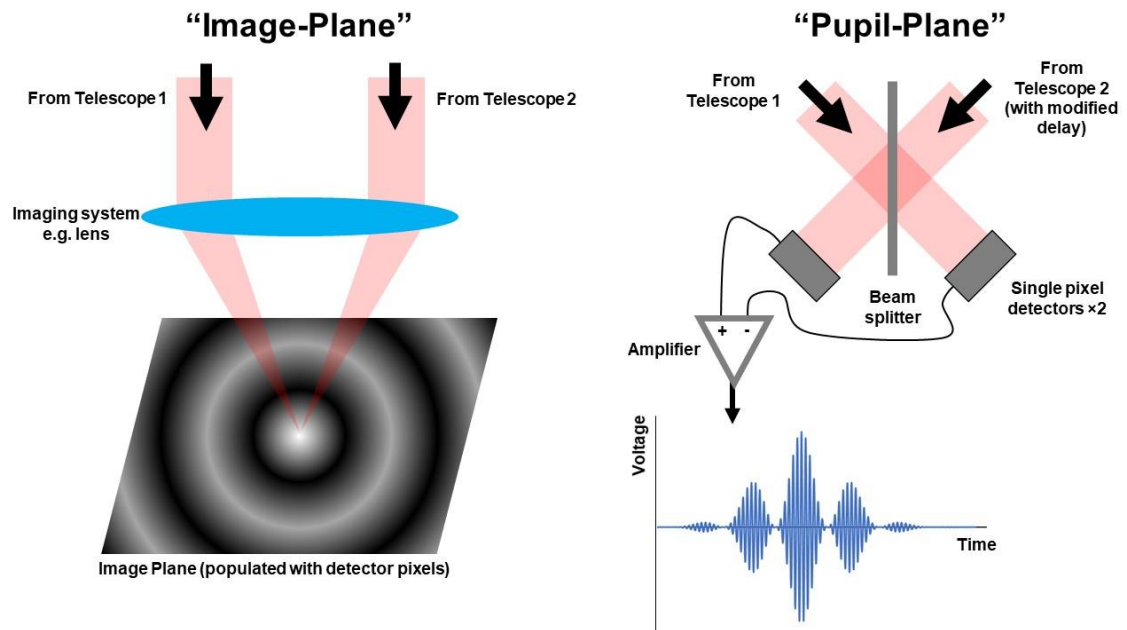

Figure 33: Schematic diagram of (Left) image-plane and (Right) pupil plane beam combination. Adapted from [90].

Pupil plane beam combiners also come in many different forms. Instruments such as AMBER, Figure 4, developed for the VLTI, use a complex optical table filled with bulk optic mirrors and beam splitters to acquire interferograms from each pair of three

telescopes in the VLTI array. Others, such as FLUOR (Figure 34) or MIRC (Michigan Infra-Red Combiner) at CHARA, use single mode optical fibres for the beam combination. In the case of MIRC, for example, six mid-infrared optical fibres are used to collect light from the six telescopes in the array. These fibres were then placed in a non-redundant linear arrangement to interferometrically combine light onto a camera. By using a non-redundant linear array, light from each pair of fibres generates fringes with a specific period on the camera, allowing the fringe visibility for each pair of telescopes to be evaluated.
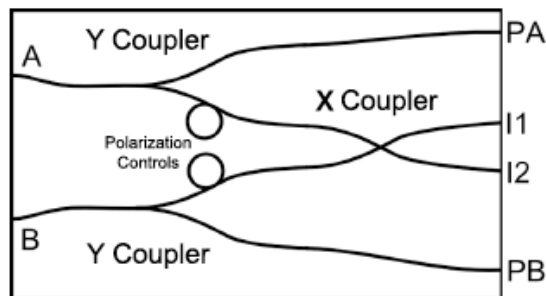
Figure 34: Schematic diagram of the MONA fibre beam combiner used in the FLUOR instrument at CHARA. Taken and adapted from [93].

A powerful alternative to fully-fibre beam combiners that has gained increasing popularity is the use of integrated optics, as first proposal by Kern et al in 1997 [12] and now used in instruments such as PIONIER [91] and GRAVITY [9] at the VLTI. In this case, all the necessary components, including beam splitters, passive phase shifters and couplers can be integrated onto a single integrated optic chip, as shown in Figure 35 for the 4-telescope integrated optic beam combiner used in GRAVITY [9]. In the paper that accompanies this chapter, I present the development of 3 dB asymmetric integrated waveguide couplers for astronomical K-band interferometry at the CHARA array.
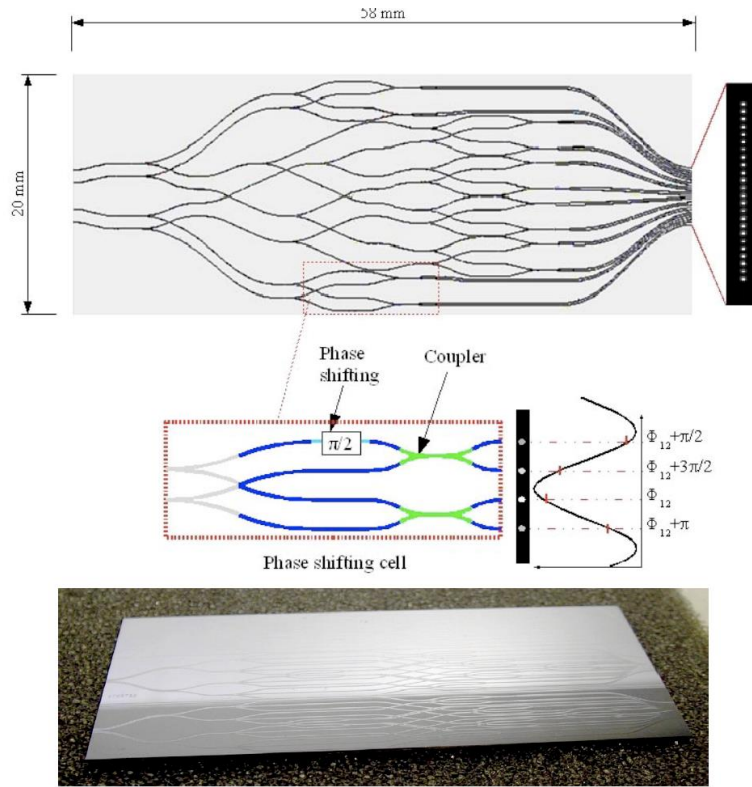
Figure 35: (Top) Schematic diagram of the waveguide layout for the 4-telescope GRAVITY beam combiner. (Middle) Phase shifting section required to generate the ABCD sampling of the interferogram. (Bottom) Photograph of the integrated optic chip. Taken and adapted from [9].

4.2 Aim of the study

The aim of this study was to develop an integrated optic replacement for the MONA fibre beam combiner used in the JouFLU beam combination instrument at CHARA, Figure 34. Over time, fibres in MONA have started to experience a degradation in performance, making high-resolution astronomy in the K-band difficult. The aim of this work was therefore to develop an integrated optic beam combiner to revive the JouFLU setup and enable K-band interferometry. The aim, therefore, was to fabricate an integrated version of the fibre beam combiner schematically presented in Figure 34.

To develop the integrated optic beam combiner, K-band waveguides that were single mode between 2.0 μm and 2.4 μm were first developed using Infrasil silica glass substrates, a low OH form of silica glass which has low-loss transmission of light over short lengths (~ few cm) out to ~ 3.0 μm. After this, K-band evanescent couplers using identical waveguides were then developed which exhibited > 50% power transfer, but

highly chromatic coupling behaviour. A new approach was then used to "detune" one waveguide relative to the other by adiabatically varying the width of one of the waveguides that forms the coupler. The result of this detuning is to achromaticise and reduce the coupling of the coupler. In this manner, we were able to develop K-band achromatic 3 dB couplers which will form the building block for a replacement integrated optic beam combiner.

4.3   My contributions

This section explains what contributions were made by myself and my co-authors towards the work in the following paper. I used ULI to fabricate and optimise straight waveguides for K-band operation in Infrasil glass with guidance from A. Benoît (AB). I adapted a code provided by D. G. MacLachlan to efficiently control the complex movement of the glass in the laser focus during the fabrication. I used ULI to fabricate and optimise the evanescent field couplers for K-band operation. I conducted all characterisation measurements. I analysed the data with AB.

The polarisation study and interferometry measurements were performed by T. K. Sharma. The interface of the beam combiner and fibre v-groove was planned by A. N. Dinkelaker. The paper was written by AB with input from myself and all other authors.

Ultrafast laser inscription of asymmetric integrated waveguide 3 dB couplers for astronomical K-band interferometry at the CHARA array

Aurélien Benoît,[1,*,†] **Fraser A. Pike,**[1,†] **Tarun K. Sharma,**[2,†] **David G. MacLachlan,**[1] **Aline N. Dinkelaker,**[3] **Abani S. Nayak,**[3] **Kalaga Madhav,**[3] **Martin M. Roth,**[3] **Lucas Labadie,**[2] **Ettore Pedretti,**[4] **Theo A. ten Brummelaar,**[5] **Nic Scott,**[6] **Vincent Coudé du Foresto,**[7] **and Robert R. Thomson**[1]

[1]*SUPA, Institute of Photonics and Quantum Sciences, Heriot-Watt University, Edinburgh, EH14 4AS, UK*
[2]*I. Physikalisches Institut der Universität zu Köln, Zülpicher Strasse 77, 50937 Cologne, Germany*
[3]*Leibniz-Institut für Astrophysik Potsdam, An der Sternwarte 16, 14482 Potsdam, Germany*
[4]*UKRI STFC Rutherford Appleton Laboratory, Chilton, UK*
[5]*Center for High Angular Resolution Astronomy, Georgia State University, P.O. Box 3969, Atlanta, Georgia 30302-3969, USA*
[6]*NASA Ames Research Center, Moffett Field, California 94035, USA*
[7]*LESIA of Paris Observatory/CNRS/UPMC/Univ. Paris Diderot, Paris, France*
*Corresponding author: a.benoit@hw.ac.uk

We present the fabrication and characterization of 3 dB asymmetric directional couplers for the astronomical K-band at wavelengths between 2.0 and 2.4 µm. The couplers were fabricated in commercial Infrasil silica glass using an ultrafast laser operating at 1030 nm. After optimizing the fabrication parameters, the insertion losses of straight single-mode waveguides were measured to be ∼1.2 ± 0.5 dB across the full K-band. We investigate the development of asymmetric 3 dB directional couplers by varying the coupler interaction lengths and by varying the width of one of the waveguide cores to detune the propagation constants of the coupled modes. In this manner, we demonstrate that ultrafast laser inscription is capable of fabricating asymmetric 3 dB directional couplers for future applications in K-band stellar interferometry. Finally, we demonstrate that our couplers exhibit an interferometric fringe contrast of >90%. This technology paves the path for the development of a two-telescope K-band integrated optic beam combiner for interferometry to replace the existing beam combiner (MONA) in Jouvence of the Fiber Linked Unit for Recombination (JouFLU) at the Center for High Angular Resolution Astronomy (CHARA) telescope array.

1. INTRODUCTION

The burgeoning field of astrophotonics has emerged over the past couple of decades and seeks to exploit photonic technologies and principles to enable the development of superior astronomical instruments [1–4]. Astrophotonics has already resulted in multiple successes, examples of which include the use of optical fibers for flexibly routing light from the telescope focal plane to spectrographs for analysis [5] and spectral imaging [6,7], and broadband laser frequency combs that provide unprecedented spectrograph calibration capabilities [8]. A raft of new and potentially transformative astrophotonic technologies is also currently under development. These

include integrated echelle gratings [9], integrated fiber-fed spectrographs [10,11], waveguide Bragg gratings to filter out atmospheric OH lines [12–14], and ring-resonator-based frequency combs [15].

One of the most impressive successes in the astrophotonics field is the development of compact integrated optic (IO) beam combiners for coherently combining the light collected by multiple telescopes [16]. Beam combining instruments that utilize IO beam combiners, such as GRAVITY [17] or Precision Integrated-Optics Near-infrared Imaging ExpeRiment (PIONIER) [18] at the Very Large Telescope Interferometer (VLTI) telescope array [19], have demonstrated excellent capabilities. Despite these instruments, current IO

beam combiners require improvements to facilitate future scalability and additional applications. First, the number of telescopes might increase to enable more interferometric baselines. Secondly, to optimize IO beam combiners for specific applications, the design might have to be iteratively changed and improved, requiring flexibility in the manufacturing process. Once the design is fixed, however, production of identical devices is required, e.g., for space applications [20,21], where a large number of devices are needed for testing, qualification, and redundancy. Additionally, the IO devices used in GRAVITY and PIONIER are fabricated using conventional planar silica-on-silicon platforms that operate efficiently in the H-band (1.5–1.8 μm) but less so at longer wavelengths [22–24]. Applications in the K-band (2.0–2.4 μm), for example, are faced with unwanted propagation losses in silica-on-silicon platforms due to the OH contaminations in the glass [25]. Using existing IO beam combiner technology to go further into the mid-infrared (IR) therefore presents a challenge. Alternative methods, such as fluorine or chalcogenide fibers, are required to access this wavelength range, which enables us to access the fingerprint region with an abundance of fundamental absorption bands of chemical species from 3 to 20 μm and can improve imaging of extrasolar planets by reducing the contrast between starlight and planet compared to the visible range [26,27]. In this context, ultrafast laser inscription (ULI), with its capacity to inscribe an inexpensive 3D low-loss waveguide in a suitable glass, is an excellent candidate for expanding the working wavelength range of IO beam combiners. This fabrication technique has recently demonstrated a variety of different 3D complex-light reformatting components for operation in the H-, L-, and M-bands with experimental laboratory results as well as some "on-sky" measurements at near-IR wavelengths [28–31] and the Guided-Light Interferometric Nulling Technology (GLINT) instrument is a permanent module on the Subaru Coronagraphic Extreme Adaptive Optics (SCExAO) system at the Subaru telescope [32].

The Center for High Angular Resolution Astronomy (CHARA) [33] of Georgia State University uses a fiber-based beam combiner technology for two-telescope interferometry in the K-band: the Fiber Linked Unit for Recombination (FLUOR) utilizes fluoride fibers. In 2014, as part of the program known as Jouvence of FLUOR (JouFLU), major upgrades were applied including the fiber-fed interferometric beam combiner

in a closed box system called MONA, achieving accurate interferometric visibility amplitude measurements with 0.1%–0.3% precision [34]. In the years since the upgrade, JouFLU has provided detailed measurements of the survey of debris-disc stars, and visibility estimation for the Exozodi survey [35,36]. Over time, however, it has started to experience technical challenges, including performance degradation, which makes high-resolution astronomy in the K-band difficult. An IO beam combiner could revive the JouFLU setup and K-band interferometry. With this in mind, we have started work to develop a two-input IO beam combiner that can become a replacement for the existing combiner, utilizing the infrastructure and optical setup of JouFLU at the CHARA array. A key enabler of this component is achromatic 3 dB couplers, the development of which we report here.

2. OVERVIEW OF A FUTURE IO BEAM COMBINER FOR JouFLU

Figure 1 presents a schematic illustration of the fiber-fed chip-based interferometric beam combiner we are developing for JouFLU, with an interface designed for the replacement of the existing MONA fiber beam combiner. Shown are the two input fibers that couple light into the ULI written waveguides on the glass substrate via a V-groove array. From the input waveguides, light is distributed to two photometric tap couplers (Tap) and two interferometric arms in the 3 dB directional coupler (3 dB) [37,38]. After the coupling region, the four outputs are connected to fibers arranged in a square array for coupling into the Near Infrared Camera and Multi-Object Spectrometer (NICMOS) camera.

Here, we investigate the potential of ULI fabrication to produce a 3 dB asymmetric IO beam combiner in Infrasil glass (IG) with the same MONA interferometric contrast around 90% for stellar interferometry over the full K-band. The paper is structured as follows. We present in Section 3 the manufacturing method and optimum parameters to obtain a low-loss 3 dB asymmetric coupler. In Section 4, we perform initial tests of the polarization behavior of the couplers and demonstrate the capacity of the integrated couplers to provide high contrast interferometry results. We present the conclusions of the paper in Section 5.
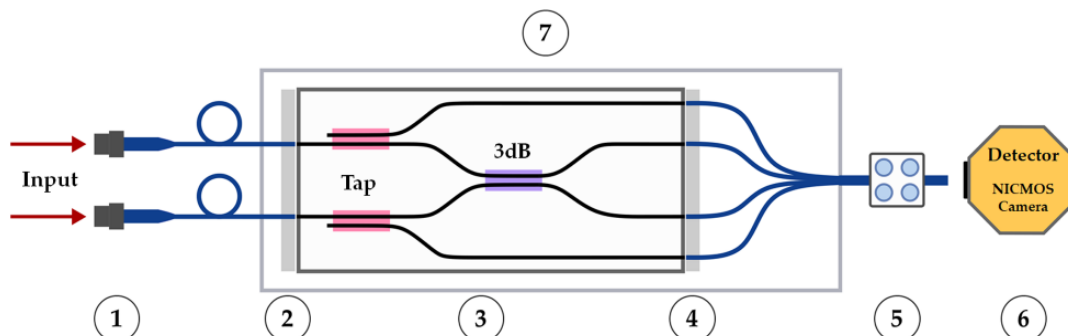
Fig. 1.   Schematic representation of the IO beam combiner being developed for JouFLU with the fiber-coupled inputs from two telescopes connected to the chip via V-grooves, ULI written waveguides for the photometric tap as well as the 3 dB direct coupler, and output fiber bundle going to the NICMOS camera and detection system. (1) Light input from the telescope via FC/PC connectors, (2) input two-fiber V-groove array, (3) 3 dB asymmetric coupler and photometric tap couplers, (4) output four-fiber V-groove array, (5) fiber square bundle to (6) NICMOS detector, and (7) full packaged beam combiner system.

3. DEVELOPING K-BAND WAVEGUIDES

A. ULI Fabrication Details

To obtain low-loss guidance in the K-band, it is necessary to use a substrate material that exhibits low absorption in the 2.0–2.4 µm spectral range. To this end, we have chosen to focus our attention on using IG as a substrate for the ULI process. To perform the ULI process, we used a LightConversion Pharos laser at 1030 nm that delivers 185 fs pulses at a pulse repetition rate of 500 kHz, with the light polarization adjusted to circular. All structures were written using a transverse writing geometry and the multiscan technique to control the waveguide cross section [39]. Accordingly, the train of ultrafast laser pulses was focused ∼250 µm below the surface of the IG substrate using a 6.24 mm focal length lens with a numerical aperture (NA) of 0.4 (Thorlabs C110 TME-B), and waveguides were formed by translating the substrate through the laser focus in the plane perpendicular to the laser beam propagation axis.

B. Characterizing ULI Fabricated Waveguides

The insertion losses of the ULI waveguides were characterized using the system shown schematically in Fig. 2. The system consists of a supercontinuum (SC) source (NKT Extreme-K) followed by a bandpass filter (BPF) for 2250 ± 250 nm (Thorlabs FB2250-500) to select the K-band wavelength span. Figure 2 presents the two steps to characterize the insertion losses of the ULI waveguides. Light from the SC source is coupled into a 2 m long commercial fiber (NuFern SM1950).

To measure the insertion loss of the waveguide, a reference spectrum is first acquired using an IR fiber-coupled optical spectrum analyzer (Thorlabs OSA205). A few percent of the input light is used to monitor the stability of the input power during the measurements. In the second step, the NuFern fiber is cleaved close to its mid-point, and the cleaved ends are coupled to the ULI waveguide under test by butt-coupling with index matching fluid to reduce Fresnel reflections. Two three-axis translation stages were used to optimize the coupling

of light between the ULI waveguide and the fibers. The spectra of the light coupled through the waveguide are acquired and compared to the reference spectrum to obtain the insertion loss across the K-band. After investigating a wide range of pulse energies for fabrication (from 33 to 255 nJ) and multiscan parameters (25 to 75 scans in steps of five and then 21 to 33 scans in steps of two), we found that optimal waveguides were fabricated using a pulse energy of 250 nJ (measured before the lens used to focus the light into the substrate), 31 scans of the substrate through the laser focus, with a scan separation of 200 nm, and a substrate translation velocity of $4 \text{ mm} \cdot \text{s}^{-1}$, corresponding to an estimated physical waveguide width of 6.2 µm. Figure 3(a) presents the insertion loss spectrum (black squares) where each point corresponds to a raw data average over a wavelength span of 8 nm, for a 17 mm long waveguide fabricated using the above-mentioned parameters. The throughput of these ULI waveguides is $\sim 1.2 \pm 0.5$ dB. We estimate that a minimum of approximately 0.02 dB/facet of this is due to coupling losses between the fiber and waveguide due to mode mismatch since the waveguide exhibits a mode field diameter (MFD) of ~ 9.8 µm, and the fiber exhibits a MFD of ~ 8.7 µm without any transverse offset. This leads us to conclude that the waveguides exhibit a maximum propagation loss of $\sim 0.68 \text{ dB} \cdot \text{cm}^{-1}$. This throughput value is of the same order of magnitude as previous single-mode ULI waveguide fabrications with $0.8 \text{ dB} \cdot \text{cm}^{-1}$ at 3.39 µm [40] or $0.85 \text{ dB} \cdot \text{cm}^{-1}$ at 1.3 µm [31].

The inset of Fig. 3(a) presents a micrograph of a ULI waveguide fabricated using the optimal ULI parameters where the incident writing laser beam comes from the top, and the writing process is from the left to right in Fig. 3(a). The insets of Fig. 3(b) show the recorded near-field intensity distributions recorded using a DataRay WinCamD microbolometer array for the fiber (F) and for the waveguide (W) with a magnification of around 67. From these near-field intensity distributions, the ULI waveguide MFD is measured around 10.3 µm on x axis and 9.3 µm on y axis at $1/e^2$ in comparison with the fiber MFD
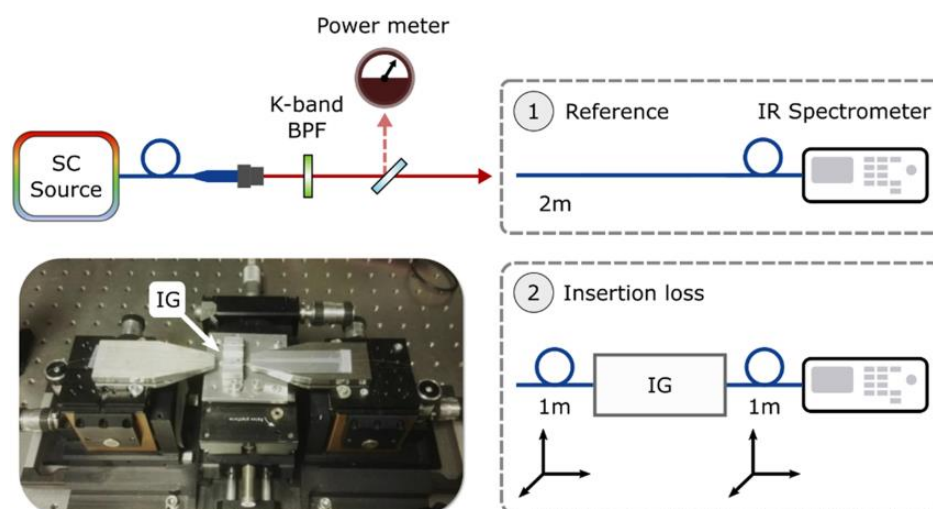
Fig. 2. Schematic representation of the experimental setup used for the waveguide and coupler characterization, based on a SC source followed by a K-band bandpass filter (BPF). Illustration of the two main steps of insertion loss measurements, with spectra measured directly for a 2 m fiber, followed by spectra for the cleaved fiber to measure insertion loss of the waveguide in IG. Inset: photograph of the double three-axis translation stage with the fibers and the IG.
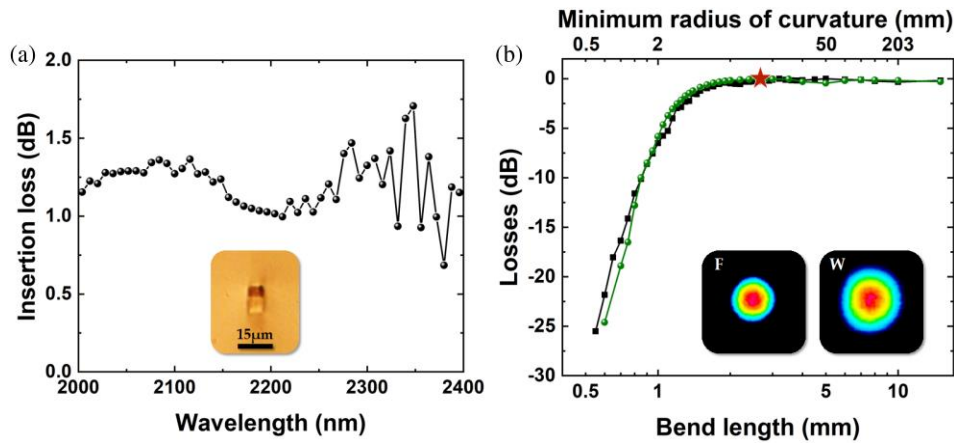
Fig. 3. (a) Insertion loss (black points) of a straight waveguide written with the best set of laser parameters where each point corresponds to a raw data average over a wavelength span of 8 nm. Inset: micrograph of the ULI waveguide. (b) Evolution of the experimental losses (black squares) in relation to the straight waveguide as a function of the bend length for a deviation of 100 μm and the simulated losses with a refractive index difference of $8 \cdot 10^{-3}$ (green points). The red star represents the radius of curvature of couplers. Inset: output near-field intensity distribution of the fiber (F) and waveguide (W).
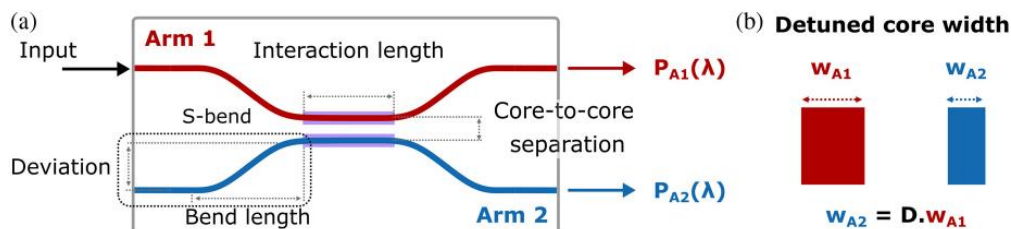
Fig. 4. (a) Schematic representation of the 3 dB asymmetric directional coupler with a description of the important geometric parameters for fabrication and characterization. (b) Illustration of waveguide width difference defined by D for the detuned core study.

measured around 8.7 μm on x axis and 8.8 μm on y axis. Using the optimal ULI parameters, we also investigated the bending-induced losses in these waveguides. To do this, we fabricated an array of 50 waveguides where each waveguide undergoes a symmetric double "S-bend" describing a "raised sinus" profile with a lateral shift deviation of 100 μm in the plane of the substrate, as presented in the dot black square labeled "S-bend" in Fig. 4(a). Figure 3(b) presents the results of experiments to characterize the bend induced losses as a function of bend length and radius of curvature. These results indicate that for a 100 μm lateral shift deviation, a bend length of 2 mm results in minimal excess loss. Calculated using CodeSeeder's BeamLab toolboxes for MATLAB and fitting the experimental bend losses [green points in Fig. 3(b)] [41], the refractive index difference of ULI waveguides is estimated at $8 \cdot 10^{-3}$.

C. Developing Asymmetric 3 dB Couplers

For all our studies, we used a substrate chip length of 17 mm, which will be sufficient in the future to fabricate the beam combiner in Fig. 1. With this in mind, we have chosen to fabricate ULI waveguides with a transverse deviation of 58.5 μm over a bend length of 2 mm providing negligible bending loss and corresponding to a minimum radius of curvature of around 14 mm [red star in Fig. 3(b)]. The multiscan fabrication process of each arm is from left to right in Fig. 3(a) where the writing

laser beam is coming from the top. For the couplers, arm 1 is written first and then arm 2, from top to bottom in Fig. 4(a).

To characterize each directional coupler, the experimental setup shown in Fig. 2 was used to measure the spectrum of the light leaving each arm—$P_{A1}(\lambda)$ and $P_{A2}(\lambda)$ for arm 1 and arm 2, respectively. When coupling light into arm 1 of the coupler, the fraction of light coupled into arm 1 at each wavelength is given as $R_1(\lambda) = P_{A1}(\lambda)/(P_{A1}(\lambda) + P_{A2}(\lambda))$ and into arm 2 $R_2(\lambda) = P_{A2}(\lambda)/(P_{A1}(\lambda) + P_{A2}(\lambda))$ [42]. For all the following coupler characterization experiments, the input light is always coupled into arm 1 of the coupler, and we describe the evolution of coupling ratios $R_1(\lambda)$ and $R_2(\lambda)$. The coupling ratio of a coupler at each wavelength is dependent on two parameters: the interaction length and the core-to-core separation defined as the distance between the two core centers, in Fig. 4(a). A detailed study was performed to understand how these two parameters impact the coupling ratio by varying the interaction length from 0.05 to 1.6 mm in steps of 0.05 mm and the core-to-core separation from 9 to 15 μm in steps of 1 μm. Figure 5 presents 2D maps representing the experimental measurements of the coupling ratios $R_1(\lambda)$ (a) and $R_2(\lambda)$ (b) for couplers fabricated with a core-to-core separation of 10 μm. The color pattern gives two pieces of information: (i) a horizontal color line indicates achromatic behavior; and (ii) a white line indicates 3 dB splitting. Thus, a white horizontal line represents achromatic 3 dB behavior over the full K-band ($R(\lambda) = 0.5$). The experimental results clearly highlight the
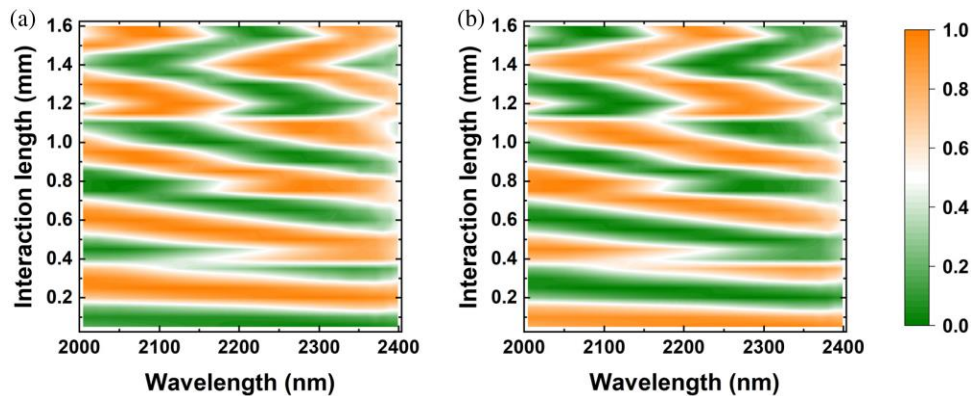
Fig. 5. 2D representation maps representing the experimental measurements providing the (a) $R_1(\lambda)$ and (b) $R_2(\lambda)$ values as a function of interaction length and propagated wavelength for a core-to-core separation of 10 μm.

impact of the interaction length on the coupling behavior in a directional coupler, with shorter interaction lengths leading to more achromatic performance. Also, one can observe the same global coupling trend with the other core-to-core separation measurements where the interaction needs to be longer to obtain the same coupling behavior for a higher core-to-core separation. Interestingly, there appears to be something of a discontinuity in the operation of the couplers once the interaction length is beyond ∼1.1 mm. This phenomenon is currently under investigation. We have performed the same experiment by coupling input light in arm 2 and a similar behavior was observed. Even though the "white line" appears to be flat and achromatic around an interaction length of 0.2 mm, a 3 dB asymmetric directional coupler is not achievable with these parameters over the full K-band.

To achieve the desired achromatic behavior, we focused our investigation on detuning the propagation constant of the guided mode in one of the waveguides in the coupler relative to the propagating mode in the other waveguide [42–45]. For the following detuned study, the investigation was carried out for all couplers with a core-to-core separation of 10 μm and the shortest interaction lengths. For our propose, the "mode-detuning" was induced by controlling the ULI process such that one of the waveguides adiabatically transitions to a smaller waveguide width as it approaches the interaction region, and then adiabatically transitions back to its original waveguide width as it leaves the coupling region. The taper length is then equal to the 2 mm bend length and is produced by adjusting the scan separation. This way, one can ensure negligeable losses along the taper transition and preserve high throughput propagation. Figure 4(b) illustrates how asymmetric directional couplers were fabricated that consisted of two waveguides—arm 1 and arm 2. Arm 1 has a width w_{A1}, and arm 2 has a width w_{A2}, which is a factor D smaller than w_{A1}. In our study, D was varied between 0.75 and 1.00 in steps of 0.05. Figures 6(a)–6(d) show the experimentally measured coupler coupling ratios (a), (c) $R_1(\lambda)$ and (b), (d) $R_2(\lambda)$ as a function of the interaction length and wavelength, with (a), (b) $D = 0.75$ and (c), (d) $D = 0.8$.

The dashed gray rectangular areas highlight the relevant interaction length that results in a close-to-3 dB achromatic behavior over the K-band for both cases. These maps show two options to obtain a 3 dB asymmetric directional coupler, one

for an interaction length of 400 μm with $D = 0.75$ and one for an interaction length of 600 μm with $D = 0.8$. Over the full K-band span, Figs. 6(e) and 6(f) present the evolutions of coupling ratios $R_1(\lambda)$ (red points) and $R_2(\lambda)$ (blue diamond) of these two possible couplers for: (e) an interaction length of 400 μm with $D = 0.75$ and (f) an interaction length of 600 μm with $D = 0.8$. These results show the capability of the ULI method to provide 3 dB asymmetric directional couplers in IG for K-band applications.

4. 3 dB ASYMMETRIC ULI COUPLERS CHARACTERIZATION

As detailed previously, the 3 dB asymmetric couplers will eventually form the heart of an IO beam combining instrument to replace the existing MONA beam combiner of the JouFLU instrument at the CHARA array. To further assess their suitability for this, we used the experimental setup shown in Fig. 7 to characterize their polarization preserving and interferometric properties. A systematic characterization of all 3 dB asymmetric directional couplers written on the chip was conducted to isolate the optimal device based on the metric of the highest broadband interferometric contrast. We present the experimental results of the identified asymmetric coupler fabricated with an interaction length of 600 μm with D = 0.8.

A. Polarization Study

During the fabrication process, ultrafast laser exposure generates form and stress birefringence in the glass substrate, which may have a substantial impact on the polarization behavior of the ULI waveguides [46,47]. As differential birefringence effects between the left and right arms of the device may result in visibility losses, we investigated this aspect and developed an experimental setup to observe the polarization behavior of the coupler for a varying input linear polarization. The experimental setup is presented in the gray dotted rectangle in Fig. 7(a). K-band filtered (SBP-2314-0001112) SC light (Leukos STM 250 MIR) is passed through a wire grid polarizer (WP25M-UB) and coupled to one input of the ULI coupler. The wire grid polarizer allows us to ensure a linearly controlled polarization state at the ULI waveguide input with an extinction ratio around
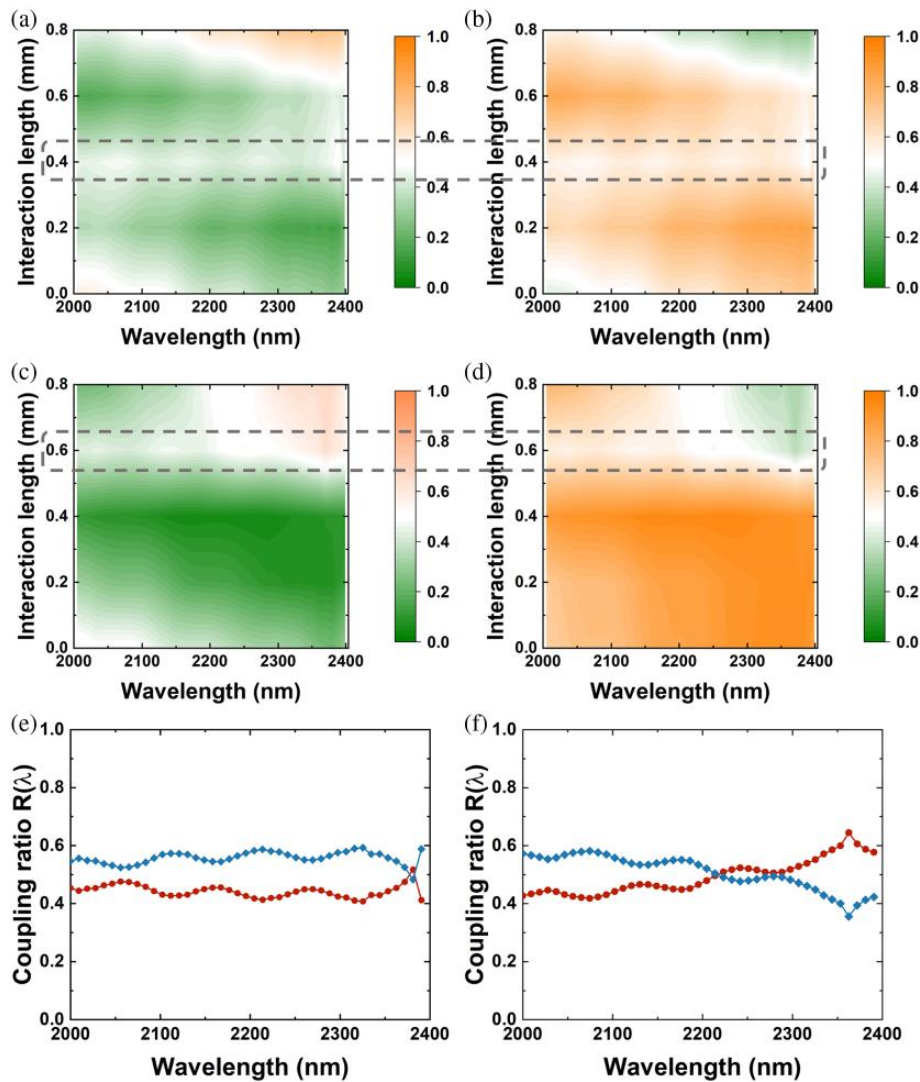
Fig. 6. 2D map representation of the full investigation of the coupling ratios (a), (c) $R_1(\lambda)$ and (b), (d) $R_2(\lambda)$ versus interaction length and propagated wavelength with (a), (b) $D = 0.75$ and (c), (d) $D = 0.8$. The dashed gray rectangle highlights the interaction length with a white horizontal power ratio line for the two arms, which represents a 3 dB asymmetric directional coupler ($R(\lambda) \sim 0.5$). Coupling ratio evolutions of $R_1(\lambda)$ in red points and $R_2(\lambda)$ in blue diamonds for (e) interaction length of 400 µm with $D = 0.75$ and (f) interaction length of 600 µm with $D = 0.8$.

30 dB over the whole K-band, even using an unpolarized SC source. The output analyzer informs us on the polarization state of the emergent light measured by the IR camera. By varying the input polarization of the coupled light with the polarizer (from 0° to 240° in steps of 20°), we investigated the polarization maintaining properties of the ULI fabricated coupler. The 0° position corresponds to the vertical direction with respect to the horizontal optics table. The polarization contrast is defined as $C_p = (I_{\text{Max}} - I_{\text{Min}})/(I_{\text{Max}} + I_{\text{Min}})$, where I_{Max} and I_{Min} are, respectively, the maximum and minimum flux measured on the IR camera (Infratech 5360S) when rotating the analyzer. Therefore, a polarization contrast $C_p = 1$ corresponds to a linear polarization, and a contrast $C_p = 0$ corresponds to a circular polarization of the output signal transmitted by the combiner. Then, intermediate values correspond to an elliptical polarization. Figures 8(a) and 8(b) present the variations in the measured polarization contrast C_p for the light collected from arm 1 and arm 2 of the asymmetric directional coupler

as a function of the input linear polarization angle. With this measurement, we identify the angular positions (with respect to the horizontal plane of the optical bench) of the fast and slow axes of the birefringent coupler, which correspond to angular directions for which the linear input polarization is maintained.

We find that, within the precision of our measurement, the positions of the fast and slow axes are at about ∼80° and ∼170° for arm 1 and arm 2, respectively, and ∼90° apart as expected. In principle, this information can be used in the future to align the axis of the input polarization-maintaining fibers and the IO combiner. This measurement also informs us on the maximum phase retardation introduced by the coupler since $C_{p,\text{min}} = \cos(\psi)$, where ψ is the phase retardation in radians. This remains true in the case of polychromatic light when we consider the relatively narrow bandwidth of the K-band filter. We find experimentally the highest retardation to be ∼80°, and as expected at about 45° from the slow/fast axis directions. Finally, we can qualitatively assess with these graphs the level of
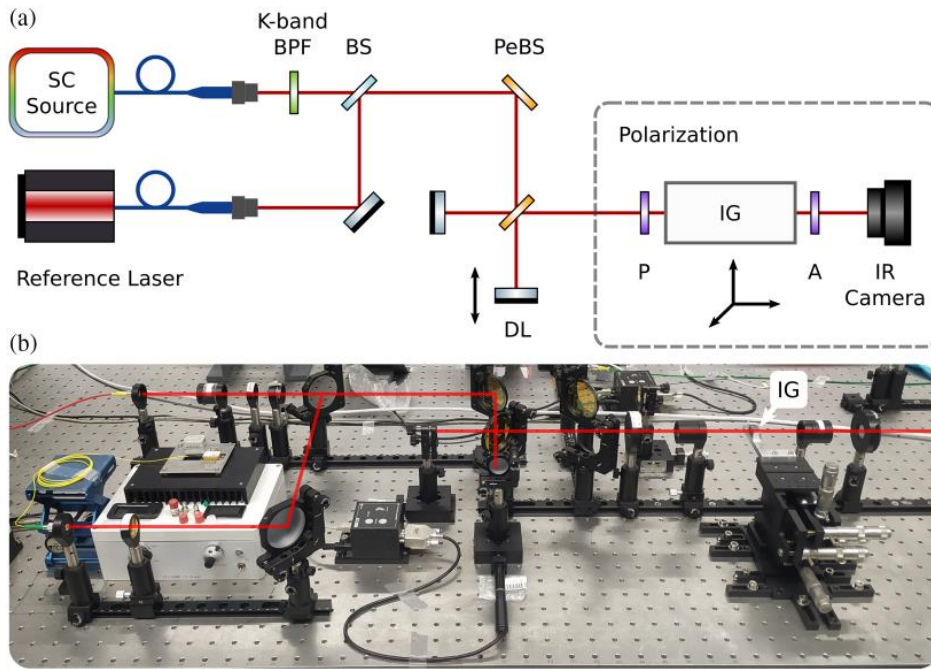
Fig. 7. (a) Schematic of the interferometry experimental setup with the two sources (SC source and reference laser at 2 µm), beam splitter (BS) to overlap the beams, followed by the interferometer based on several pellicle beam splitters (PeBS) and a delay line mirror (DL) as well as a fixed mirror. Light is then passed through a polarizer (P) before being coupled in the asymmetric directional couplers on the glass substrate, finally passing through an analyzer (A), after which an IR camera acquires the output light. (b) Photograph of the interferometry setup.
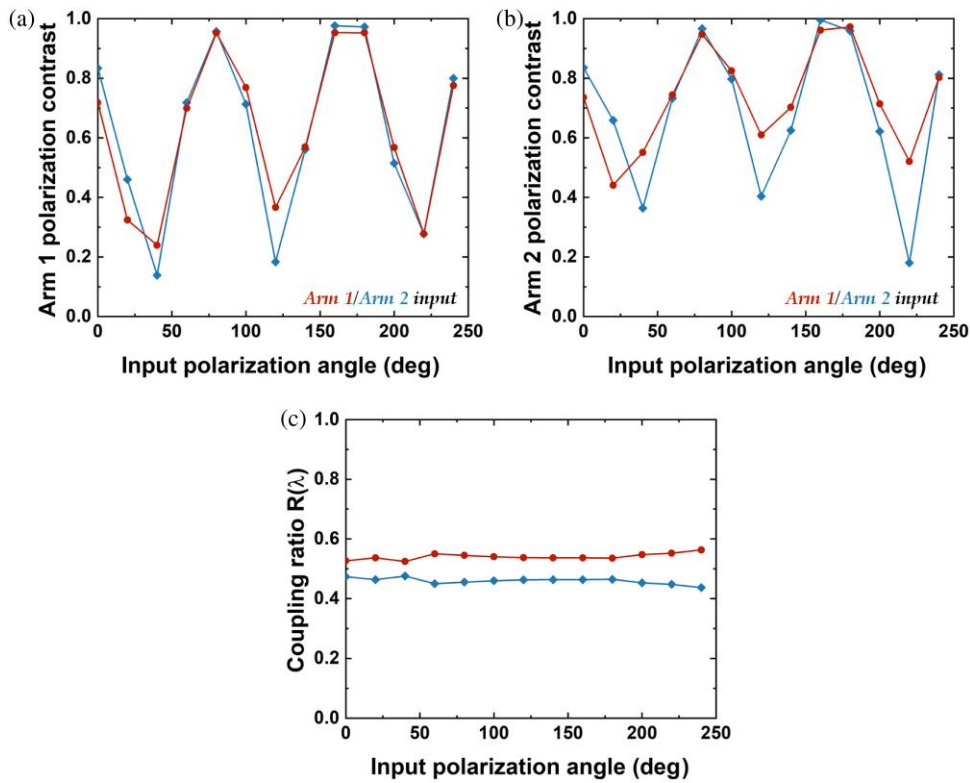
Fig. 8. (a) Evolution of the output polarization contrast in arm 1 and (b) arm 2 as a function of the input polarization angle when light is coupled to arm 1 (red point curve) or arm 2 (diamond blue curve). (c) Evolution of coupling ratios $R_1(\lambda)$ in red points and $R_2(\lambda)$ in blue diamonds as a function of the input polarization angle.

differential birefringence between the two arms of the coupler [48]. This can inform us on the possibility of visibility losses due to polarization effects. For a given output arm [Fig. 8(a) or Fig. 8(b)], the two red and blue curves should ideally be the same if no differential birefringence is present. While comparable in shape, we qualitatively observe that both outputs of the combiner are affected by some level of differential birefringence, with arm 2 (right) slightly worse than arm 1 (left). However, this level of differential birefringence will not result in a significant visibility loss as we will see in the next section, at least for classical V^2 interferometry. Finally, Fig. 8(c) shows the dependence of beam combiner coupling ratio $R(\lambda)$ with the input linear polarization direction, which is controlled by the input polarizer. No analyzer is used at the waveguide outputs in this case. We observe only a mild variation of $\sim$5% in the coupling ratio as a function of the input linear polarization angle, with the two curves $R(\lambda)$ showing a relatively flat profile. Again, we have performed this experiment by coupling input light in arm 2, and a similar behavior was observed. While such an effect can generally be mitigated by instrumental strategies (e.g., splitting the input horizontal and vertical polarizations), it is reassuring to observe that the intensity unbalance of the coupler is only slightly dependent on the input polarization. This may become relevant when both polarizations of the incoming beams are coupled into the chip. We believe that the polarization effects we have observed are due to stress induced birefringence in the coupler interaction region. In particular, the birefringence properties of the waveguide inscribed first, arm 1 in our case, become altered by the stress field generated by the inscription of the second waveguide arm 2 [49,50]. The impact of this stress field is observed in the discrepancy of polarization contrast at the output of the two arms, as presented in Figs. 8(a) and 8(b).

B. Interferometry Measurements

The interferometric bench setup (Fig. 7) is based on a SC source followed by a K-band BPF and a reference continuous wave laser diode emitting at 2 µm, which can be aligned with the broadband source by tilting a beam splitter (BS). The bench is based on a classical two-channel interferometric setup, described in more detail in [51]. A polarizer can be placed in the input beam to change the linear polarization angle before coupling light

in the coupler. The delay line scans the fringes over 100 µm [±50 µm around the zero optical path difference (OPD)] at a speed of 0.5 µm per second, and the data are recorded at 250 Hz. Figure 9(a) presents the interferogram patterns recorded for the two arms of the 3 dB asymmetric directional coupler. The total length of the fringe packet is about 200 µm, double the scan range, because of mirror reflection. Figure 9(b) shows a close-up view of the central OPD region, where the π-phase shift between the two outputs of the coupler is clearly visible. The interferogram shows some noise contribution at the position of successive maxima. Before deriving the instrumental contrast, we reduced the impact of the high-frequency noise by applying the Savitzky–Golay (SG) smoothing and differentiation filtering method [52]. Following this step, the broadband instrumental contrast was measured to be 92%, which is represented by the dark curves and the dashed gray lines in Fig. 9(b). Following the analysis presented Section 4.A, we investigated the dependence of the interferometric contrast with the angular direction of the input linear polarization.

For this purpose, three measurements were acquired with input linear polarization angles of 0°, 45°, and 90°, and we find that in all three cases, the contrast is $\geq$92%. In absence of a measurement of the bare contrast of the test bench, the contrast of 92% should be understood as a current upper limit of the performance of the beam combiner. Further and more detailed characterization of the intrinsic performance of the bench [51] could help to disentangle more precisely the contributions to be attributed to the beam combiner and refine the ultimate achievable performances of the device. Our analysis shows that the ULI platform can deliver high-quality K-band IO beam combiners with high instrumental contrast, which are relatively polarization insensitive.

5. CONCLUSION

We reported the development of 3 dB asymmetric directional couplers that operate across the full K-band between 2.0 and 2.4 µm for future stellar interferometry applications. The couplers were fabricated in a commercial IG using ULI with optimized parameters, with straight waveguides exhibiting an insertion loss of $\sim$1.2 ± 0.5 dB over the K-band with single-mode behavior. A number of asymmetric directional couplers
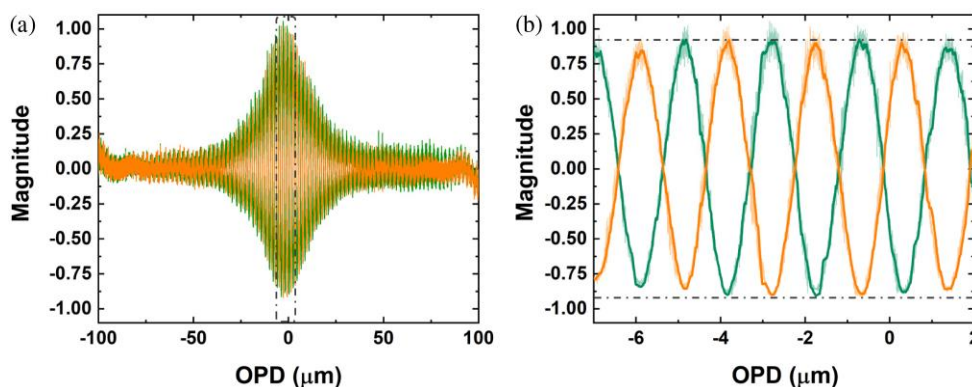
Fig. 9.   (a) Full interferometer pattern recorded for the two arms of the 3 dB asymmetric directional coupler and a close-up in the dashed rectangular region (b) using a FFT filtering correction. (b) Close-up of (a) showing the noisy FFT correction in the background as transparent curves and the SG results as dark curves, corresponding to a contrast magnitude of 92%.

with different interaction lengths and geometric properties were studied to achieve the best device, which exhibits 3 dB achromatic splitting behavior over the K-band. We presented the results of characterization experiments, which demonstrate that the birefringence axes of the coupler waveguides are not aligned with each other and are not aligned with the substrate axis. Finally, two successive filtering corrections (FFT and SG) provide a high contrast magnitude of 92%. The results demonstrate that ULI can fabricate high-quality asymmetric directional couplers for applications in K-band astronomical interferometry. We aim to use these devices to develop a complete two-telescope K-band IO beam combiner system to replace the existing beam combiner MONA in JouFLU at the CHARA array. The ULI fabrication method can be easily adapted to fabricate a 3D multi-telescope interferometer in K-band.

Disclosures. The authors declare no conflicts of interest.

Data Availability. Data underlying the results presented in this paper are not publicly available at this time but may be obtained from the authors upon reasonable request.

†These authors contributed equally to this paper.

REFERENCES

1. J. Bland-Hawthorn and P. Kern, "Astrophotonics: a new area for astronomical instruments," Opt. Express **17**, 1880–1884 (2009).
2. V. Coudé du-Foresto and S. T. Ridgway, "FLUOR–a Stellar interferometer using single-mode fibers," in *European Southern Observatory Astrophysics Symposia*, J. M. Beckers and F. Merkle, eds. (1992), Vol. **39**, p. 731.
3. V. Coudé du Foresto, G. Perrin, J.-M. Mariotti, M. Lacasse, and W. Traub, "The FLUOR/IOTA fiber stellar interferometer," in *Integrated Optics for Astronomical Interferometry*, P. Kern and F. Malbet, eds. (1997), pp. 115–125.
4. K. Rousselet-Perraut, P. Haguenauer, P. Petmezakis, J.-P. Berger, D. Mourard, S. D. Ragland, G. Huss, F. Reynaud, E. LeCoarer, P. Y. Kern, and F. Malbet, "Qualification of IONIC (integrated optics nearinfrared interferometric camera)," Proc. SPIE **4006**, 1042–1051 (2000).
5. I. J. Lewis, R. D. Cannon, K. Taylor, K. Glazebrook, J. A. Bailey, I. K. Baldry, J. R. Barton, T. J. Bridges, G. B. Dalton, T. J. Farrell, P. M. Gray, A. Lankshear, C. McCowage, I. R. Parry, R. M. Sharples, K. Shortridge, G. A. Smith, J. Stevenson, J. O. Straede, L. G. Waller, J. D. Whittard, J. K. Wilcox, and K. C. Willis, "The Anglo-Australian observatory 2dF facility," Mon. Not. R. Astron. Soc. **333**, 279–298 (2002).
6. M. M. Roth, A. Kelz, T. Fechner, T. Hahn, S.-M. Bauer, T. Becker, P. Böhm, L. Christensen, F. Dionies, J. Paschke, E. Popow, D. Wolter, J. Schmoll, U. Laux, and W. Altmann, "PMAS: The Potsdam multi-aperture spectrophotometer. I. Design, manufacture, and performance," Publ. Astron. Soc. Pac. **117**, 620 (2005).
7. A. Kelz, M. A. W. Verheijen, M. M. Roth, S. M. Bauer, T. Becker, J. Paschke, E. Popow, S. F. Sánchez, and U. Laux, "PMAS: the

8. Potsdam multi-aperture spectrophotometer. II. The wide integral field unit PPak," Publ. Astron. Soc. Pac. **118**, 129 (2006).
9. M. T. Murphy, T. Udem, R. Holzwarth, A. Sizmann, L. Pasquini, C. Araujo-Hauck, H. Dekker, S. D'Odorico, M. Fischer, T. W. Hänsch, and A. Manescau, "High-precision wavelength calibration of astronomical spectrographs with laser frequency combs," Mon. Not. R. Astron. Soc. **380**, 839–847 (2007).
9. A. Stoll, Y. Wang, and K. Madhav, "Integrated Echelle gratings for astrophotonics," Proc. SPIE **11203**, 112030Z (2020).
10. M. Mayor, F. Pepe, D. Queloz, F. Bouchy, G. Rupprecht, G. Curto, G. A. Avila, W. Benz, J. Bertaux, X. Bonfils, T. Dall, H. Dekker, B. Delabre, W. Eckert, M. Fleury, A. Gilliotte, D. Gojak, J. Guzman, D. Kohler, J. Lizon, A. Longinotti, C. Lovis, D. Mégevand, L. Pasquini, and J. Reyes, "Setting new standards with HARPS," Messenger **114**, 20–24 (2003).
11. N. Cvetojevic, N. Jovanovic, J. Lawrence, M. Withford, and J. Bland-Hawthorn, "Developing arrayed waveguide grating spectrographs for multi-object astronomical spectroscopy," Opt. Express **20**, 2062–2072 (2012).
12. C. Q. Trinh, S. C. Ellis, J. Bland-Hawthorn, J. S. Lawrence, A. J. Horton, S. G. Leon-Saval, K. Shortridge, J. Bryant, S. Case, M. Colless, W. Couch, K. Freeman, H.-G. Loehmannsroeben, L. Gers, K. Glazebrook, R. Haynes, S. Lee, J. O'Byrne, and S. Miziar, "GNOSIS: The first instrument to use fiber Bragg gratings for OH suppression," Astron. J. **145**, 51 (2013).
13. N. Jovanovic, N. Cvetojevic, B. Norris, C. Betters, C. Schwab, J. Lozi, O. Guyon, S. Gross, F. Martinache, P. Tuthill, D. Doughty, Y. Minowa, N. Takato, and J. Lawrence, "Demonstration of an efficient, photonic-based astronomical spectrograph on an 8-m telescope," Opt. Express **25**, 17753–17766 (2017).
14. J. Bland-Hawthorn, M. Englund, and G. Edvell, "New approach to atmospheric OH suppression using an aperiodic fibre Bragg grating," Opt. Express **12**, 5902–5909 (2004).
15. M.-G. Suh, X. Yi, Y. H. Lai, S. Leifer, I. S. Grudinin, G. Vasisht, E. C. Martin, M. P. Fitzgerald, G. Doppmann, J. Wang, D. Mawet, S. B. Papp, S. A. Diddams, C. Beichman, and K. Vahala, "Searching for exoplanets using a microresonator astrocomb," Nat. Photonics **13**, 25–30 (2019).
16. H. A. McAlister, W. G. Bagnuolo, Jr., W. I. Hartkopf, and A. K. Garrison, "Multiple-telescope optical interferometric array," Proc. SPIE **1237**, 22–30 (1990).
17. F. Eisenhauer, G. Perrin, W. Brandner, C. Straubmeier, K. Perraut, A. Amorim, M. Schöller, S. Gillessen, P. Kervella, M. Benisty, C. Araujo-Hauck, L. Jocou, J. Lima, G. Jakob, M. Haug, Y. Clénet, T. Henning, A. Eckart, J. Berger, P. Garcia, R. Abuter, S. Kellner, T. Paumard, S. Hippler, S. Fischer, T. Moulin, J. Villate, G. Ávila, A. Gräter, S. Lacour, A. Huber, M. Wiest, A. Nolot, P. Carvas, R. Dorn, O. Pfuhl, E. Gendron, S. Kendrew, S. Yazici, S. Antón, Y. Jung, M. Thiel, E. Choquet, R. Klein, P. Teixeira, P. Gitton, D. Moch, F. Vincent, N. Kudryavtseva, S. Ströbele, S. Sturm, P. Fédou, R. Lenzen, P. Jolley, C. Kister, V. Lapeyrère, V. Naranjo, C. Lucuix, R. Hofmann, F. Chapron, U. Neumann, L. Mehrgan, O. Hans, G. Rousset, J. Ramos, M. Suárez, R. Lederer, J. Reess, R. Rohloff, P. Haguenauer, H. Bartko, A. Sevin, K. Wagner, J. Lizon, S. Rabien, C. Collin, G. Finger, R. Davies, D. Rouan, M. Wittkowski, K. Dodds-Eden, D. Ziegler, F. Cassaing, H. Bonnet, M. Casali, R. Genzel, and P. Léna, "GRAVITY: observing the universe in motion," Messenger **143**, 16 (2011).
18. M. Benisty, J.-P. Berger, L. Jocou, P. Labeye, F. Malbet, K. Perraut, and P. Kern, "An integrated optics beam combiner for the second generation VLTI instruments," Astron. Astrophys. **498**, 601–613 (2009).
19. M. Schöller, "The Very Large Telescope Interferometer: current facility and prospects," New Astron. Rev. **51**, 628–638 (2007).
20. J. D. Monnier, A. Aarnio, O. Absil, N. Anugu, E. Baines, A. Bayo, J.-P. Berger, L. I. Cleeves, D. Dale, W. Danchi, W. J. de Wit, D. Defrère, S. Domagal-Goldman, M. Elvis, D. Froebrich, M. Gai, P. Gandhi, P. Garcia, T. Gardner, D. Gies, J.-F. Gonzalez, B. Gunter, S. Hoenig, M. Ireland, A. M. Jorgensen, M. Kishimoto, L. Klarmann, B. Kloppenborg, J. Kluska, J. S. Knight, Q. Kral, S. Kraus, L. Labadie, P. Lawson, J.-B. Le Bouquin, D. Leisawitz, E. G. Lightsey, H. Linz, S. Lipscy, M. MacGregor, H. Matsuo, B. Mennesson, M. Meyer, E. A. Michael, F. Millour, D. Mozurkewich, R. Norris, M. Ollivier, C.

Packham, R. Petrov, L. Pueyo, B. Pope, S. Quanz, S. Ragland, G. Rau, Z. Regaly, A. Riva, R. Roettenbacher, G. Savini, B. Setterholm, M. Sewilo, M. Smith, L. Spencer, T. ten Brummelaar, N. Turner, G. van Belle, G. Weigelt, and M. Wittkowski, "A realistic roadmap to formation flying space interferometry," Astro2020 APC White Paper, arXiv: 1907.09583 (2019).

21. S. Piacentini, T. Vogl, G. Corrielli, P. K. Lam, and R. Osellame, "Space qualification of ultrafast laser-written integrated waveguide optics," Laser Photon. Rev. **15**, 2000167 (2020).

22. K. Perraut, L. Jocou, J. P. Berger, A. Chabli, V. Cardin, G. Chamiot-Maitral, A. Delboulbé, F. Eisenhauer, Y. Gambérini, S. Gillessen, S. Guieu, J. Guerrero, M. Haug, F. Hausmann, F. Joulain, P. Kervella, P. Labeye, S. Lacour, C. Lanthermann, V. Lapras, J. B. Le Bouquin, M. Lippa, Y. Magnard, T. Moulin, P. Noël, A. Nolot, F. Patru, G. Perrin, O. Pfuhl, S. Pocas, S. Poulain, C. Scibetta, E. Stadler, R. Templier, N. Ventura, C. Vizioz, A. Amorim, W. Brandner, and C. Straubmeier, "Single-mode waveguides for GRAVITY–I. The cryogenic 4-telescope integrated optics beam combiner," Astron. Astrophys. **614**, A70 (2018).

23. GRAVITY Collaboration, "First light for GRAVITY: phase referencing optical interferometry for the Very Large Telescope Interferometer," Astron. Astrophys. **602**, A94 (2017).

24. L. Jocou, K. Perraut, A. Nolot, T. Moulin, Y. Magnard, P. Labeye, V. Lapras, F. Eisenhauer, G. Perrin, A. Amorim, W. Brandner, and C. Straubmeier, "The integrated optics beam combiner assembly of the GRAVITY/VLTI instrument," Proc. SPIE **8445**, 84452X (2012).

25. O. Humbach, H. Fabian, and U. Grzesik, "Analysis of OH absorption bands in synthetic silica," J. Non-Crys. Sol. **203**, 19–26 (1996).

26. L. Labadie and O. Wallner, "Mid-infrared guided optics: a perspective for astronomical instruments," Opt. Express **17**, 1947–1962 (2009).

27. W. A. Traub and K. W. Jucks, "A possible aeronomy of extrasolar terrestrial planets," arXiv: 0205369 (2002).

28. N. Jovanovic, P. G. Tuthill, and B. Norris, "Starlight demonstration of the Dragonfly instrument: an integrated photonic pupil-remapping interferometer for high-contrast imaging," Mon. Not. R. Astron. Soc. **427**, 806–815 (2012).

29. J. Tepper, L. Labadie, S. Gross, A. Arriola, S. Minardi, R. Diener, and M. J. Withford, "Ultrafast laser inscription in ZBLAN integrated optics chips for mid-IR beam combination in astronomical interferometry," Opt. Express **25**, 20642–20653 (2017).

30. F. A. Pike, A. Benoît, D. G. MacLachlan, R. J. Harris, I. Gris-Sánchez, D. Lee, T. A. Birks, and R. R. Thomson, "Modal noise mitigation for high-precision spectroscopy using a photonic reformatter," Mon. Not. R. Astron. Soc. **497**, 3713–3725 (2020).

31. S. Haffert, R. J. Harris, A. Zanutta, F. A. Pike, A. Bianco, E. M. A. Redaelli, A. Benoît, D. G. MacLachlan, C. A. Ross, I. Gris-Sánchez, M. D. Trappen, Y. Xu, M. Blaicher, G. Riva, B. Sinquin, C. Kulcsár, N. A. Bharmal, É. Gendron, L. Staykov, T. J. Morris, S. Barboza, N. Münch, L. F. Bardou, L. Prengère, H.-F. G. Raynaud, P. Hottinger, T. Anagnos, J. Osborn, C. Koos, R. R. Thomson, T. A. Birks, I. A. G. Snellen, and C. U. Keller, "Diffraction-limited integral-field spectroscopy for extreme adaptive optics systems with the multicore fiber-fed integral-field unit," J. Astron. Telesc. Instrum. Syst. **6**, 045007 (2020).

32. B. R. M. Norris, N. Cvetojevic, T. Lagadec, N. Jovanovic, S. Gross, A. Arriola, T. Gretzinger, M.-A. Martinod, O. Guyon, J. Lozi, M. J. Withford, J. S. Lawrence, and P. Tuthill, "First on-sky demonstration of an integrated-photonic nulling interferometer: the GLINT instrument," Mon. Not. R. Astron. Soc. **491**, 4180–4193 (2020).

33. T. A. ten Brummelaar, H. A. McAlister, S. T. Ridgway, W. G. Bagnuolo, Jr., N. H. Turner, L. Sturmann, J. Sturmann, D. H. Berger, C. E. Ogden, R. Cadman, W. I. Hartkopf, C. H. Hopper, and M. A. Shure, "First results from the CHARA array. II. Description of the instrument," Astron. J. **628**, 453–465 (2005).

34. N. J. Scott, R. Millan-Gabet, E. Lhomé, T. A. Ten Brummelaar, V. Coudé Du Foresto, J. Sturmann, and L. Sturmann, "Jouvence of

FLUOR: upgrades of a fiber bean combiner at the CHARA array," J. Astron. Instrum. **2**, 1340005 (2013).

35. P. D. Nuñez, N. J. Scott, B. Mennesson, O. Absil, J.-C. Augereau, G. Bryden, T. ten Brummelaar, S. Ertel, V. Coudé du Foresto, S. T. Ridgway, J. Sturmann, L. Sturmann, N. J. Turner, and N. H. Turner, "A near-infrared interferometric survey of debris-disc stars," Astron. Astrophys. **608**, A113 (2017).

36. P. D. Nuñez, T. ten Brummelaar, B. Mennesson, and N. J. Scott, "Visibility estimation for the CHARA/JouFLU Exozodi survey," Publ. Astron. Soc. Pac. **129**, 024002 (2017).

37. J. B. LeBouquin, K. Rousselet-Perraut, P. Kern, F. Malbet, P. Haguenauer, P. Kervella, I. Schanen, J. P. Berger, A. Delboulbé, B. Arezki, and M. Schöller, "First observations with an H-band integrated optics beam combiner at the VLTI," Astron. Astrophys. **424**, 719–726 (2004).

38. M. Olivero, M. Svalgaard, L. Jocou, and J.-P. Berger, "Direct UV-written integrated optical beam combiner for stellar interferometry," J. Lightwave Technol. **25**, 367–371 (2007).

39. G. Brown, R. R. Thomson, A. K. Kar, N. D. Psaila, and H. T. Bookey, "Ultrafast laser inscription of Bragg-grating waveguides using the multiscan technique," Opt. Lett. **37**, 491–493 (2012).

40. A. Arriola, S. Mukherjee, D. Choudhury, L. Labadie, and R. R. Thomson, "Ultrafast laser inscription of mid-IR directional couplers for stellar interferometry," Opt. Lett. **39**, 4820–4822 (2014).

41. https://www.codeseeder.com/.

42. W. J. Chen, S. M. Eaton, H. Zhang, and P. R. Herman, "Broadband directional couplers fabricated in bulk glass with high repetition rate femtosecond laser pulses," Opt. Express **16**, 11470–11480 (2008).

43. A. Takagi, K. Jinguji, and M. Kawachi, "Design and fabrication of broad-band silica-based optical waveguide couplers with asymmetric structure," IEEE J. Quantum Electron. **28**, 848–855 (1992).

44. T. Gretzinger, S. Gross, A. Arriola, T. T. Fernandez, D. Strixner, J. Tepper, L. Labadie, and M. J. Withford, "Broadband mid-infrared directional and multimode interference couplers in GLS glass fabricated using femtosecond laser direct-writing," in *Conference on Lasers and Electro-Optics (CLEO)* (2019), paper cm_4_1.

45. M. Olivero and M. Svalgaard, "Direct UV-written broadband directional planar waveguide couplers," Opt. Express **13**, 8390–8399 (2005).

46. L. A. Fernandes, J. R. Grenier, P. R. Herman, J. S. Aitchison, and P. V. S. Marques, "Femtosecond laser writing of waveguide retarders in fused silica for polarization control in optical circuits," Opt. Express **19**, 18294–18301 (2011).

47. L. A. Fernandes, J. R. Grenier, P. R. Herman, J. S. Aitchison, and P. V. S. Marques, "Stress induced birefringence tuning in femtosecond laser fabricated waveguides in fused silica," Opt. Express **20**, 24103–24114 (2012).

48. R. Diener, S. Nolte, T. Pertsch, and S. Minardi, "Effects of stress on neighboring laser written waveguides in gallium lanthanum sulfide," Appl. Phys. Lett. **112**, 111908 (2018).

49. J. Tepper, L. Labadie, R. Diener, S. Minardi, J.-U. Pott, R. Thomson, and S. Nolte, "Integrated optics prototype beam combiner for long baseline interferometry in the L and M bands," Astron. Astrophys. **602**, A66 (2017).

50. G. Corrielli, S. Atzeni, S. Piacentini, I. Pitsios, A. Crespi, and R. Osellame, "Symmetric polarization-insensitive directional couplers fabricated by femtosecond laser writing," Opt. Express **26**, 15101–15109 (2018).

51. J. Tepper, R. Diener, L. Labadie, S. Minardi, S. Gross, A. Arriola, M. Withford, and S. Nolte, "Photonics-based mid-infrared interferometry: the challenges of polychromatic operation and comparative performances," Proc. SPIE **10701**, 107011B (2018).

52. A. Savitzky and M. J. E. Golay, "Soothing and differentiation of data by simplified least squares procedures," Anal. Chem. **36**, 1627–1639 (1964).

Chapter 5- Conclusions and outlook

5.1   Conclusions

This thesis introduced the area of exoplanet research within astronomy, and set out the instrumentation standards, challenges, and developments towards solutions which are currently relevant to the field. The importance of spectrographs and beam combiners in this matter was developed and in particular, astrophotonics was proposed as a method of improving instrumentation for exoplanet research. Current examples of astrophotonic devices such as photonic lanterns, laser frequency combs and integrated beam combiners were introduced, and it was shown how these are already improving astronomical capabilities. The technique of ULI was introduced, in particular the potential of ULI waveguide-based devices in astronomical instruments such as spectrographs and beam combiners. Three chapters demonstrating successful applications of ULI in astrophotonic devices followed this introduction.

High-resolution spectrographs such as those used in radial velocity observations, often suffer from modal noise, especially in the near-IR. Modal noise causes variations in the output speckle pattern and therefore acquired spectrum due to movements in the fibre and input. Typically, this is mitigated by agitation of the fibre so the noise can be time-averaged. The PIMMS design was proposed as a way to mitigate modal noise in an innovative astrophotonic way, but the pseudo-slit is very long and requires a large detector. The hybrid reformatter developed by MacLachlan et al made use of a ULI slit to overcome this challenge, and demonstrated strong on-sky throughput.

A prototype spectrograph was constructed in order to measure the level of modal noise mitigation the hybrid reformatter could provide over a comparable basic multimode fibre using conventional fibre agitation techniques. One method of comparison using a broadband source and performing a statistical analysis indicated a factor of 6 reduction in modal noise. A second method of comparison monitoring the variation in positions of multiple spectrally narrow peaks indicated the hybrid reformatter mitigated modal noise to the same level as a single mode fibre i.e. the modal noise was below detectable limits. Further analysis to account for temperature variations in the lab maintained this conclusion. The single spectroscopic line radial velocity precision of 80 m.s^{-1} demonstrates strong capabilities for hybrid reformatter-based spectrographs.

A further area of interest in exoplanet observations is direct imaging, and in particular the combining of this with spectroscopy so as to characterise the atmosphere. IFUs are a suitable method for this, and require a high density of single mode cores. A multicore fibre based IFU has been identified as a way to meet this need. The main challenge with this was avoiding overlap of the huge number of spectra on the detector which was spread out by a ULI reformatter.

The full MCIFU instrument consisted of an MCF with microlenses to enable efficient coupling, a ULI waveguide reformatter, a mask to block stray light made by ULI assisted chemical etching, and a VPHG-based spectrograph. Lab results indicated the reformatter cores had throughputs in J-band of up to 67% with good alignment, and the mask blocked stray light by many orders of magnitude. An on-sky run at the WHT in July 2019 demonstrated a successful proof of concept by resolving the Earth's telluric lines from a spectrum of Vega.

Stellar interferometry is a popular observation technique requiring a beam combiner instrument. Integrated beam combiners are currently offering good performance in state-of-the-art instruments. The MONA fibre beam combiner at the CHARA array has suffered a degradation in performance, and the use of ULI in the development of asymmetric integrated waveguide 3 dB couplers for astronomical K-band interferometry at the CHARA array was undertaken.

The 1.2 ± 0.5 dB insertion losses in the resulting K-band single mode waveguides indicated strong potential for on-sky performance. 3 dB achromatic coupling was achieved by varying the interaction length of two coupler arms and detuning the propagation constants via narrowing of one waveguide core. The coupler exhibited an interferometric fringe contrast of 92%. The potential of this ULI beam combiner is strong and is due to be tested on-sky.

These three ULI devices each demonstrate a successful application of the technique to astrophotonic instruments. The ability to create specific waveguide components has addressed many of the challenges similar instruments need to overcome, in a cost-effective and scalable manner. Going forward, the work contained in this thesis may be

further developed to give instrumentation engineers confidence in the effectiveness of a ULI-based instrument, and improve observation capabilities overall.

5.2   Future work

This section describes recent developments in the continuation of the work in this thesis and suggests some ideas for improvements. The suggestions are not exhaustive, but I hope the reader may find them useful.

The spectrograph used to investigate modal noise had a basic design. With the initial study showing promising results, a next step could be the integration of the hybrid reformatter with a spectrograph engineered for a higher resolving power and greater environmental stability, and with a cross-dispersed design encompassing a larger spectral region. Improvements in the stability of the ULI process could allow for a straighter slit to be produced in future. The stray light may also be blocked in a much more effective way by using a mask manufactured in a similar manner to the one used on the MCIFU reformatter.

A number of possible improvements to the MCIFU were identified, including those relating to the gratings, detector, and microlenses. Specifically regarding the reformatter, with more development time it would be possible to perfect the alignment process so that all cores had the same throughput as shown in the central ones, and the mask could also be refined for a more precise fit and alignment. Testing of the instrument at MagAO-X in Chile was planned but delayed by the pandemic. The improved coupling from an extreme AO system may have demonstrated the multi-object observing capabilities of this type of spectrograph.

The production of a final beam combiner for CHARA was delayed due to the pandemic, but it is still the intention of our collaboration to test our device on-sky. Good progress has been made improving the ULI process, in particular the iteration of the beam NA via an SLM phase mask to optimise this very important parameter in a time-effective and repeatable manner.

References

[1]   S. C. Ellis and J. Bland-Hawthorn, The case for OH suppression at near-infrared wavelengths, Monthly Notices of the Royal Astronomical Society **386**, 47-64 (2008).

[2]   M. Mayor, F. Pepe, D. Queloz, F. Bouchy, G. Rupprecht, *et al.*, Setting New Standards with HARPS, The Messenger **114**, 20-24 (2003).

[3]   C. Quercellini, L. Amendola, A. Balbi, P. Cabella, and M. Quartin, Real-time Cosmology, Physics Reports **521**, 95-134 (2012).

[4]   R. Sharples, R. Bender, A. A. Berbel, N. Bezawada, R. Castillo, *et al.*, First Light for the KMOS Multi-Object Integral-Field-Spectrometer, The Messenger **151**, 21-23 (2013).

[5]   I. J. Lewis, R. D. Cannon, K. Taylor, K. Glazebrook, J. A. Bailey, *et al.*, The Anglo-Australian Observatory 2dF facility, Monthly Notices of the Royal Astronomical Society **333**, 279-298 (2002).

[6]   J. J. Bryant, M. S. Owers, A. S. G. Robotham, S. M. Croom, S. P. Driver, *et al.*, The SAMI Galaxy Survey: instrument specification and target selection, Monthly Notices of the Royal Astronomical Society **447**, 2857-2879 (2015).

[7]   T. A. ten Brummelaar and H. A. McAlister, "Optical and Infrared Interferometers," in Planets, Stars and Stellar Systems: Volume 1, T. D. Oswalt and I. S. McLean, eds. (Springer, 2013).

[8]   J. Bland-Hawthorn, S. C. Ellis, S. G. Leon-Saval, R. Haynes, M. M. Roth, *et al.*, A complex multi-notch astronomical filter to suppress the bright infrared sky, Nature Communications **2**, 581 (2011).

[9]   S. Gillessen, F. Eisenhauer, G. Perrin, W. Brandner, C. Straubmeier, *et al.*, GRAVITY: a four-telescope beam combiner instrument for the VLTI, Proc. SPIE 7734, Optical and Infrared Interferometry II, 77340Y (2010).

[10]   R. A. McCracken, É. Depagne, R. B. Kuhn, N. Erasmus, L. A. Crause, and D. T. Reid, Wavelength calibration of a high resolution spectrograph with a partially stabilized 15-GHz astrocomb from 550 to 890 nm, Optics Express **25**, 6450-6460 (2017); https://doi.org/10.1364/OE.25.006450.

[11]   R. G. Petrov, F. Malbet, G. Weigelt, P. Antonelli, U. Beckmann, *et al.*, AMBER, the near-infrared spectro-interferometric three-telescope VLTI instrument, A&A **464**, 1-12 (2007).

[12]   P. Kern, F. Malbet, I. Schanen-Duport, and P. Benech, "Integrated Optics Single-mode Interferometric Beam Combiner for Near Infrared Astronomy," in Integrated Optics for Astronomical Interferometry, p. 115 (1997).

[13]   G. Zins, B. Lazareff, J.-P. Berger, J.-P. Le Bouquin, L. Jocou, *et al.*, PIONIER: A Four-telescope Instrument for the VLTI, The Messenger **146**, 12-17 (2011).

[14]   GRAVITY Collaboration *et al.*, First direct detection of an exoplanet by optical interferometry, A&A **623**, L11 (2019).

[15]   GRAVITY Collaboration *et al.*, Detection of the Schwarzschild precession in the orbit of the star S2 near the Galactic centre massive black hole, A&A **636**, L5 (2020).

[16] J.-B. Le Bouquin, J.-P. Berger, B. Lazareff, G. Zins, P. Haugenauer, *et al.*, PIONIER: a 4-telescope visitor instrument at VLTI, A&A **535**, A67 (2011).

[17] C. Q. Trinh, S. C. Ellis, J. Bland-Hawthorn, A. J. Horton, J. S. Lawrence, and S. G. Leon-Saval, The nature of the near-infrared interline sky background using fibre Bragg grating OH suppression, Monthly Notices of the Royal Astronomical Society **432**, 3262-3277 (2013).

[18] H. Kosaka, T. Kawashima, A. Tomita, M. Notomi, T. Tamamura, T. Sato, and S. Kawakami, Superprism Phenomena in Photonic Crystals: Toward Microscale Lightwave Circuits, Journal of Lightwave Technology **17**, 2032 (1999).

[19] E. le Coarer, S. Blaize, P. Benech, I. Stefanon, A. Morand, *et al.*, Wavelength-scale stationary-wave integrated Fourier-transform spectrometry, Nature Photonics **1**, 473-478 (2007).

[20] P. Gatkine, S. Veilleux, Y. Hu, J. Bland-Hawthorn, and M. Dagenais, Arrayed waveguide grating spectrometers for astronomical applications: new results, Optics Express **25**, 17918-17935 (2017).

[21] N. Cvetojevic, N. Jovanovic, C. Betters, J. S. Lawrence, S. C. Ellis, G. Robertson, and J. Bland-Hawthorn, First starlight spectrum captured using an integrated photonic micro-spectrograph, A&A **544**, L1 (2012).

[22] R. J. Harris and J. R. Allington-Smith, Applications of Integrated Photonic Spectrographs in astronomy, Monthly Notices of the Royal Astronomical Society **428**, 3139-3150 (2013).

[23] N. Jovanovic, C. Schwab, O. Guyon, J. Lozi, N. Cvetojevic *et al.*, Efficient injection from large telescopes into single-mode fibres: Enabling the era of ultra-precision astronomy, A&A **604**, A122 (2017).

[24] S. G. Leon-Saval, T. A. Birks, J. Bland-Hawthorn, and M. Englund, "Multimode fiber devices with single-mode performance," Optics Letters **30**, 2545-2547 (2005).

[25] T. A. Birks, I. Gris-Sánchez, S. Yerolatsitis, S. G. Leon-Saval, and R. R. Thomson, The photonic lantern, Advances in Optics and Photonics **7**, 107-167 (2015).

[26] D. Noordegraaf, P. M. W. Skovgaard, M. D. Maack, J. Bland-Hawthorn, R. Haynes, and J. Lægsgaard, Multi-mode to single-mode conversion in a 61 port Photonic Lantern, Optics Express **18**, 4673-4678 (2010).

[27] T. A. Birks, B. J. Mangan, A. Díez, J. L. Cruz, and D. F. Murphy, "Photonic lantern" spectral filters in multi-core fibre, Optics Express **20**, 13996-14008 (2012).

[28] R. R. Thomson, T. A. Birks, S. G. Leon-Saval, A. K. Kar, and J. Bland-Hawthorn, Ultrafast laser inscription of an integrated photonic lantern, Optics Express **19**, 5698-5705 (2011).

[29] R. J. Harris, D. G. MacLachlan, D. Choudhury, T. J. Morris, E. Gendron, A. G. Basden, G. Brown, J. R. Allington-Smith, and R. R. Thomson, Photonic spatial reformatting of stellar light for diffraction-limited spectroscopy, Monthly Notices of the Royal Astronomical Society **450**, 428-434 (2015).

[30] J. Oaks, J. A. Buisson, and M. M. Largay, A summary of the GPS constellation clock performance, Proceedings of the 39th Annual Precise Time and Time Interval Meeting, p. 119 (2007).

[31]   R. A. Probst, G. Lo Curto, G. Ávila, A. Brucalassi, B. L. Canto Martins, *et al.*, Relative stability of two laser frequency combs for routine operation on HARPS and FOCES, Proc. SPIE 9908, Ground-based and Airborne Instrumentation for Astronomy VI, 990864 (2016).

[32]   N. Jovanovic, P. G. Tuthill, B. Norris, S. Gross, P. Stewart, *et al.*, Starlight demonstration of the Dragonfly instrument: an integrated photonic pupil-remapping interferometer for high-contrast imaging , Monthly Notices of the Royal Astronomical Society **427**, 806-815 (2012).

[33]   I. Gris-Sánchez, D. M. Haynes, K. Ehrlich, R. Haynes, and T. A. Birks, Multicore fibre photonic lanterns for precision radial velocity Science, Monthly Notices of the Royal Astronomical Society **475**, 3065-3075 (2018).

[34]   P.-I. Dietrich, R. J. Harris, M. Blaicher, M. K. Corrigan, T. J. Morris, W. Freude, A. Quirrenbach, and C. Koos, Printed freeform lens arrays on multi-core fibers for highly efficient coupling in astrophotonic systems, Optics Express **25**, 18288-18295 (2017).

[35]   B. R. M. Norris, J. Wei, C. H. Betters, A. Wong, and S. G. Leon-Saval, An all-photonic focal-plane wavefront sensor, Nature Communications **11**, 5335 (2020).

[36]   M. Ams, G. D. Marshall, P. Dekker, M. Dubov, V. K. Mezentsev, I. Bennion, and M. J. Withford, Investigation of Ultrafast Laser--Photonic Material Interactions: Challenges for Directly Written Glass Photonics, IEEE Journal of Selected Topics in Quantum Electronics **14**, 1370-1381 (2008).

[37]   R. R. Gattass and E. Mazur, Femtosecond laser micromachining in transparent materials, Nature Photonics **2**, 219-225 (2008).

[38]   C. Hnatovsky, R. S. Taylor, P. P. Rajeev, E. Simova, V. R. Bhardwaj, D. M. Rayner, and P. B. Corkum, Pulse duration dependence of femtosecond-laser-fabricated nanogratings in fused silica, Applied Physics Letters **87**, 014104 (2005).

[39]   S. M. Eaton, H. Zhang, P. R. Herman, F. Yoshino, L. Shah, J. Bovatsek, and A. Y. Arai, Heat accumulation effects in femtosecond laser-written waveguides with variable repetition rate, Optics Express **13**, 4708-4716 (2005).

[40]   R. Osellame, S. Taccheo, M. Marangoni, R. Ramponi, P. Laporta, D. Polli, S. De Silvestri, and G. Cerullo, Femtosecond writing of active optical waveguides with astigmatically shaped beams, Journal of the Optical Society of America B **20**, 1559-1567 (2003).

[41]   R. R. Thomson, A. S. Bockelt, E. Ramsay, S. Beecher, A. H. Greenaway, A. K. Kar, and D. T. Reid, Shaping ultrafast laser inscribed optical waveguides using a deformable mirror, Optics Express **16**, 12786-12793 (2008).

[42]   Y. Nasu, M. Kohtoku, and Y. Hibino, Low-loss waveguides written with a femtosecond laser for flexible interconnection in a planar light-wave circuit, Optics Letters **30**, 723-725 (2005).

[43]   A. H. Nejadmalayeri and P. R. Herman, Ultrafast laser waveguide writing: lithium niobate and the role of circular polarization and picosecond pulse width, Optics Letters **31**, 2987-2989 (2006).

[44]   M. Ams, G. D. Marshall, and M. J. Withford, Study of the influence of femtosecond laser polarisation on direct writing of waveguides, Optics Express **14**, 13158-13163 (2006).

[45] C. Hnatovsky, R. S. Taylor, E. Simova, P. P. Rajeev, D. M. Rayner, V. R. Bhardwaj, and P. B. Corkum, Fabrication of microchannels in glass using focused femtosecond laser radiation and selective chemical etching, Applied Physics A **84**, 47-61 (2006).

[46] D. G. MacLachlan, R. R. Thomson, C. R. Cunningham, and D. Lee, Mid-Infrared Volume Phase Gratings Manufactured using Ultrafast Laser Inscription, Optical Materials Express **3**, 1616-1624 (2013).

[47] B. Olivier and Y. Bellouard, On the use of a digital twin to enhance femtosecond laser inscription of arbitrary phase patterns, JPhys Photonics **3**, 005003 (2021).

[48] S. Nolte, M. Will, J. Burghoff, and A. Tuennermann, Femtosecond waveguide writing: a new avenue to three-dimensional integrated optics, Applied Physics A **77**, 109-111 (2003).

[49] R. G. H. van Uden, R. A. Correa, E. Antonio Lopez, F. M. Huijskens, C. Xia, *et al.*, Ultra-high-density spatial division multiplexing with a few-mode multicore fibre, Nature Photonics **8**, 865-870 (2014).

[50] I. Spaleniak, N. Jovanovic, S. Gross, M. J. Ireland, J. S. Lawrence, and M. J. Withford, Integrated photonic building blocks for next-generation astronomical instrumentation II: the multimode to single mode transition, Optics Express **21**, 27197-27208 (2013).

[51] I. Spaleniak, S. Gross, N. Jovanovic, R. J. Williams, J. S. Lawrence, M. J. Ireland, and M. J. Withford, Multiband processing of multimode light: combining 3D photonic lanterns with waveguide Bragg gratings, Laser & Photonics Reviews **8**, L1-L5 (2014).

[52] R. R. Thomson, N. D. Psaila, S. J. Beecher, and A. K. Kar, Ultrafast laser inscription of a high-gain Er-doped bismuthate glass waveguide amplifier, Optics Express **18**, 13212-13219 (2010).

[53] C. Khurmi, S. Thoday, T. M. Monro, G. Chen, and D. G. Lancaster, Visible laser emission from a praseodymium-doped fluorozirconate guided-wave chip, Optics Letters **42**, 3339-3342 (2017).

[54] J. Siebenmorgen, T. Calmano, K. Petermann, and G. Huber, Highly efficient Yb:YAG channel waveguide laser written with a femtosecond-laser, Optics Express **18**, 16035-16041 (2010).

[55] S. Taccheo, G. Della Valle, R. Osellame, G. Cerullo, N. Chiodo, *et al.*, Er:Yb-doped waveguide laser fabricated by femtosecond laser pulses, Optics Letters **29**, 2626-2628 (2004).

[56] F. Fusari, R. R. Thomson, G. Jose, F. M. Bain, A. A. Lagatsky, *et al.*, Lasing action at around 1.9 µm from an ultrafast laser inscribed Tm-doped glass waveguide, Optics Letters **36**, 1566-1568 (2011).

[57] J. R. Macdonald, S. J. Beecher, P. A. Berry, G. Brown, K. L. Schepler, and A. K. Kar, Efficient mid-infrared Cr:ZnSe channel waveguide laser operating at 2486 nm, Optics Letters **38**, 2194-2196 (2013).

[58] R. Osellame, M. Lobino, N. Chiodo, M. Marangoni, G. Cerullo, and R. Ramponi *et al.*, Femtosecond laser writing of waveguides in periodically poled lithium niobate preserving the nonlinear coefficient, Applied Physics Letters **90**, 241107 (2007).

[59] J. Burghoff, C. Grebing, S. Nolte, and A. Tünnermann, Efficient frequency doubling in femtosecond laser-written waveguides in lithium niobate, Applied Physics Letters **89**, 081108 (2006).

[60] S. Kroesen, K. Tekce, J. Imbrock, and C. Denz, Monolithic fabrication of quasi phase-matched waveguides by femtosecond laser structuring the χ(2) nonlinearity, Applied Physics Letters **107**, 101109 (2015).

[61] Y. Cheng, K. Sugioka, K. Midorikawa, M. Masuda, K. Toyoda, M. Kawachi, and K. Shihoyama, Three-dimensional micro-optical components embedded in photosensitive glass by a femtosecond laser, Optics Letters **28**, 1144-1146 (2003).

[62] Z. Wang, K. Sugioka, and K. Midorikawa, Three-dimensional integration of microoptical components buried inside photosensitive glass by femtosecond laser direct writing, Applied Physics A **89**, 951-955 (2007).

[63] F. He, J. Lin, and Y. Cheng, Fabrication of hollow optical waveguides in fused silica by three-dimensional femtosecond laser micromachining, Applied Physics B **105**, 379-384 (2011).

[64] D. Choudhury, W. T. Ramsay, R. Kiss, N. A. Willoughby, L. Paterson, and A. K. Kar, A 3D mammalian cell separator biochip, Lab on a Chip **12**, 948-953 (2012).

[65] G. Nava, T. Yang, V. Vitali, P. Minzioni, I. Cristiani, *et al.*, Newtonian to non-newtonian fluid transition of a model transient network, Soft Matter **14**, 3288-3295 (2018).

[66] P. Paiè, F. Bragheri, A. Bassi, and R. Osellame, Selective plane illumination microscopy on a chip, Lab on a Chip **16**, 1556-1560 (2016).

[67] N. Bellini, K. C. Vishnubhatla, F. Bragheri, L. Ferrara, P. Minzioni, R. Ramponi, I. Cristiani, and R. Osellame, Femtosecond laser fabricated monolithic chip for optical trapping and stretching of single cells, Optics Express **18**, 4679-4688 (2010).

[68] A. Crespi, R. Osellame, R. Ramponi, D. J. Brod, E. F. Galvão, *et al.*, Integrated multimode interferometers with arbitrary designs for photonic boson sampling, Nature Photonics **7**, 545-549 (2013).

[69] M. C. Rechtsman, J. M. Zeuner, Y. Plotnik, Y. Lumer, D. Podolsky, F. Dreisow, S. Nolte, M. Segev, and A. Szameit, Photonic Floquet topological insulators, Nature **496**, 196-200 (2013).

[70] S. Mukherjee, A. Spracklen, D. Choudhury, N. Goldman, P. Öhberg, E. Andersson, and R. R. Thomson, Observation of a Localized Flat-Band State in a Photonic Lieb Lattice, Physical Review Letters **114**, 245504 (2015).

[71] J. R. Grenier, L. A. Fernandes, P. V. S. Marques, J. S. Aitchison, and P. R. Herman, Optical Circuits in Fiber Cladding: Femtosecond laser-written Bragg Grating Waveguides, in *CLEO:2011 - Laser Applications to Photonic Applications* (Optical Society of America, Baltimore, Maryland, 2011), p. CMZ1.

[72] J. He, B. Xu, X. Xu, C. Liao, and Y. Wang, Review of Femtosecond-Laser-Inscribed Fiber Bragg Gratings: Fabrication Technologies and Sensing Applications, Photonic Sensors **11**, 203-226 (2021).

[73] J. C. W. Corbett and J. Allington-Smith, Fibre modal noise issues in astronomical spectrophotometry, Proc. SPIE 6269, Ground-based and Airborne Instrumentation for Astronomy, 62693N (2006).

[74] E. Oliva, M. Rainer, A. Tozzi, N. Sanna, M. Iuzzolino, and A. Brucalassi, Experimental characterization of modal noise in multimode fibers for astronomical spectrometers, A&A **632**, A21 (2019).

[75] N. Jovanovic, C. Schwab, N. Cvetojevic, O. Guyon, and F. Martinache, Enhancing Stellar Spectroscopy with Extreme Adaptive Optics and Photonics, Publications of the Astronomical Society of the Pacific **128**, 121001 (2016).

[76] J. R. Crepp, J. Crass, D. King, A. Bechter, E. Bechter, *et al.*, iLocater: a diffraction-limited Doppler spectrometer for the Large Binocular Telescope, Proc. SPIE 9908, Ground-based and Airborne Instrumentation for Astronomy VI, 990819 (2016).

[77] G. Raskin, J. Pember, D. Rogozin, C. Schwab, and D. Coutts, Fiber modal noise mitigation by a rotating double scrambler, Proc. SPIE 11451, Advances in Optical and Mechanical Technologies for Telescopes and Instrumentation IV, 114516F (2020).

[78] S. Mahadevan, S. Halverson, L. Ramsey, and N. Venditti, Suppression of fiber modal noise induced radial velocity errors for bright emission-line calibration sources, The Astrophysical Journal **786**, 18 (2014).

[79] R. R. Petersburg, T. M. McCracken, D. Eggerman, C. A. Jurgenson, D. Sawyer, A. E. Szymkowiak, and D. A. Fischer, Modal Noise Mitigation through Fiber Agitation for Fiber-fed Radial Velocity Spectrographs, The Astrophysical Journal **853**, 181 (2018); https://doi.org/10.3847/1538-4357/aaa487.

[80] T. A. Birks, B. J. Mangan, A. Díez, J. L. Cruz, and D. F. Murphy, "Photonic lantern" spectral filters in multi-core fibre, Optics Express **20**, 13996-14008 (2012).

[81] C. H. Betters, S. G. Leon-Saval, J. G. Robertson, and J. Bland-Hawthorn, Beating the classical limit: A diffraction-limited spectrograph for an arbitrary input beam, Optics Express **21**, 26103-26112 (2013).

[82] S. G. Leon-Saval, C. H. Betters, and J. Bland-Hawthorn, The Photonic TIGER: a multicore fiber-fed spectrograph, Proc. SPIE 8450, Modern Technologies in Space- and Ground-based Telescopes and Instrumentation II, 84501K (2012).

[83] D. G. MacLachlan, R. J. Harris, I Gris-Sánchez, T. J. Morris, D. Choudhury, *et al.*, Efficient photonic reformatting of celestial light for diffraction-limited spectroscopy, Monthly Notices of the Royal Astronomical Society **464**, 4950-4957 (2017).

[84] A. D. Rains, M. J. Ireland, N. Jovanovic, J. Bento, T. Feger, *et al.*, Development of the single-mode fiber integral field unit for the RHEA Spectrograph, Proc. SPIE 10702, Ground-based and Airborne Instrumentation for Astronomy VII, 107025J (2018).

[85] C. A. Ross, D. G. MacLachlan, D. Choudhury, and R. R. Thomson, Optimisation of ultrafast laser assisted etching in fused silica, Optics Express **26**, 24343-24356 (2018).

[86] M. Cirasuolo, J. Afonso, M. Carollo, H. Flores, R. Maiolino, *et al.*, MOONS: the Multi-Object Optical and Near-infrared Spectrograph for the VLT, Proc. SPIE 9147, Ground-based and Airborne Instrumentation for Astronomy V, 91470N (2014).

[87] C. Ross, D. Lee, I. Guinouard, and R. R. Thomson, Microlenses for astrophotonic instruments manufactured by ultrafast-laser assisted etching, Proc. SPIE 11451, Advances in Optical and Mechanical Technologies for Telescopes and Instrumentation IV, 114510P (2020).

[88] D. Choudhury, A. Arriola, J. R. Allington-Smith, C. Cunningham, and R. R. Thomson, Towards freeform microlens arrays for near infrared astronomical instruments, Proc. SPIE 9151, Advances in Optical and Mechanical Technologies for Telescopes and Instrumentation, Proc. SPIE 9151, Advances in Optical and Mechanical Technologies for Telescopes and Instrumentation, 915146 (2014).

[89]   N. Lindenmann, S. Dottermusch, M. L. Goedecke, T. Hoose, M. R. Billah, T. P. Onanuga, A. Hofmann, W. Freude, and C. Koos, Connecting Silicon Photonic Circuits to Multicore Fibers by Photonic Wire Bonding, Journal of Lightwave Technology **33**, 755-760 (2015).

[90]   J. D. Monnier, Optical interferometry in astronomy, Reports on Progress in Physics **66**, 789 (2003).

[91]   A. Glindemann, "Principles of Stellar Interferometry," p. 59 (Springer, 2011).

[92]   J. A. Högbom, Aperture synthesis with a non-regular distribution of interferometer baselines, Astronomy and Astrophysics Supplement Series **15**, 417-426 (1974).

[93]   N. J. Scott, R. Millan-Gabet, E. Lhomé, T. A. ten Brummelaar, V. Coudé Du Foresto, J. Sturmann, and L. Sturmann, Jouvence of FLUOR: upgrades of a fiber beam combiner at the CHARA array, Journal of Astronomical Instrumentation **2**, 1340005 (2013).